Methods[1]

R.N. Harris, A. Sakaguchi, K. Petronotis, A.T. Baxter, R. Berg, A. Burkett, D. Charpentier, J. Choi, P. Diz Ferreiro, M. Hamahashi, Y. Hashimoto, K. Heydolph, L. Jovane, M. Kastner, W. Kurz, S.O. Kutterolf, Y. Li, A. Malinverno, K.M. Martin, C. Millan, D.B. Nascimento, S. Saito, M.I. Sandoval Gutierrez, E.J. Screaton, C.E. Smith-Duque, E.A. Solomon, S.M. Straub, W. Tanikawa, M.E. Torres, H. Uchimura, P. Vannucchi, Y. Yamamoto, Q. Yan, and X. Zhao[2]

Chapter contents

[1] Harris, R.N., Sakaguchi, A., Petronotis, K., Baxter, A.T., Berg, R., Burkett, A., Charpentier, D., Choi, J., Diz Ferreiro, P., Hamahashi, M., Hashimoto, Y., Heydolph, K., Jovane, L., Kastner, M., Kurz, W., Kutterolf, S.O., Li, Y., Malinverno, A., Martin, K.M., Millan, C., Nascimento, D.B., Saito, S., Sandoval Gutierrez, M.I., Screaton, E.J., Smith-Duque, C.E., Solomon, E.A., Straub, S.M., Tanikawa, W., Torres, M.E., Uchimura, H., Vannucchi, P., Yamamoto, Y., Yan, Q., and Zhao, X., 2013. Methods. *In* Harris, R.N., Sakaguchi, A., Petronotis, K., and the Expedition 344 Scientists, *Proc IODP,* 344: College Station, TX (Integrated Ocean Drilling Program). doi:10.2204/iodp.proc.344.102.2013
[2] **Expedition 344 Scientists' addresses.**

Introduction

This introductory section provides an overview of operations, depth conventions, curatorial procedures, and general core handling and analysis during Integrated Ocean Drilling Program (IODP) Expedition 344. This information will help the reader understand the basis of our shipboard observations and preliminary interpretations. It will also enable interested investigators to identify data and select samples for further analysis. The information presented here pertains to shipboard operations and analyses described in the site chapters. Methods used by various investigators for shore-based analyses of Expedition 344 samples and data associated with separate scientific studies can be found in individual publications in various professional journals.

Site locations

GPS coordinates from precruise site surveys or from preexisting IODP sites were used to position the vessel at Expedition 344 sites. A SyQwest Bathy 2010 CHIRP subbottom profiler was used to monitor seafloor depth on the approach to each site to confirm depth profiles. Once the vessel was positioned at a site, the thrusters were lowered and a positioning beacon was dropped to the seafloor at all sites except Site U1381. Dynamic positioning control of the vessel uses navigational input from the GPS system and triangulation to the seafloor beacon, weighted by the estimated positional accuracy. The final hole position was the mean position calculated from GPS data collected over a significant portion of the time the hole was occupied.

Drilling operations

The advanced piston corer (APC), extended core barrel (XCB), and rotary core barrel (RCB) systems were used during Expedition 344. The APC and XCB systems were used to recover the sedimentary section in Holes U1381C, U1412A, U1412B, U1413A, U1413B, and U1414A and the sediment/basement interface at Hole U1381C. The RCB system was used to recover sediment and basement sections in Holes U1380C, U1412C, U1412D, U1413C, and U1414A.

The APC system cuts soft-sediment cores with minimal coring disturbance relative to other IODP coring systems. After the APC core barrel is lowered through the drill pipe and lands above the bit, the drill pipe is pressured up until the two shear pins that hold the inner barrel attached to the outer barrel fail. The inner

doi:10.2204/iodp.proc.344.102.2013

barrel then advances into the formation and cuts the core. The driller can detect a successful cut, or "full stroke," from observation of the pressure gauge on the rig floor because the excess pressure accumulated prior to the stroke drops rapidly.

APC refusal is conventionally defined in two ways: (1) the piston fails to achieve a complete stroke (as determined from the pump pressure and recovery reading) because the formation is too hard or (2) excessive force (>60,000 lb; ~267 kN) is required to pull the core barrel out of the formation. When a full or partial stroke can be achieved but excessive force cannot retrieve the barrel, the core barrel can be "drilled over" (i.e., after the inner core barrel is successfully shot into the formation, the drill bit is advanced to total depth to free the APC barrel).

The XCB system was used to advance the hole when APC refusal occurred before the target depth was reached or when drilling conditions required it. The XCB is a rotary system with a small cutting shoe that extends below the large rotary APC/XCB bit. The smaller bit can cut a semi-indurated core with less torque and fluid circulation than the main bit, potentially improving recovery. The XCB cutting shoe (bit) extends ~30.5 cm ahead of the main bit in soft sediment but can be retracted into the main bit when hard formations are encountered.

The bottom-hole assembly (BHA) used for APC and XCB coring was composed of an 11 7/16 inch (~29.05 cm) drill bit, a bit sub, a seal bore drill collar, a landing saver sub, a modified top sub, a modified head sub, five 8¼ inch control length drill collars, a tapered drill collar, two stands of 5½ inch transition drill pipe, and a crossover sub to the drill pipe that extended to the surface.

The RCB BHA included a 9⅞ inch RCB drill bit, a bit sub, an outer core barrel, a modified top sub, a modified head sub, a variable number of 8¼ inch control length drill collars, a tapered drill collar, two stands of 5½ inch drill pipe, and a crossover sub to the drill pipe that extended to the surface.

Nonmagnetic core barrels were used most of the time in the APC and RCB sections, and APC cores were oriented with the FlexIT tool when coring conditions allowed. Formation temperature measurements were taken in all APC holes to determine heat flow through the sedimentary section (see **"Physical properties"**).

Most APC-cored intervals were ~9.5 m long, and XCB-cored intervals were ~9.7–9.8 m long, which is the length of both a standard core barrel and a joint of drill pipe. In some cases, the hole was drilled or "washed" ahead without recovering sediment to advance the drill bit to the target depth at which core recovery needed to resume. Depths of drilled intervals and core recovery are provided in the "Operations" section of each site chapter.

IODP depth conventions

Deep Sea Drilling Project, Ocean Drilling Program (ODP), and IODP Phase 1 reports, diagrams, and publications used three primary designations to reference depth: meters below rig floor (mbrf), meters below seafloor (mbsf), and meters composite depth (mcd). These designations evolved over many years to meet the needs of individual science parties, but over the course of ODP and early IODP scientific drilling, issues with the existing depth scale designations and the lack of a consistent framework became apparent. A new classification and nomenclature for depth scale types was defined in 2006–2007 during the hiatus in IODP drilling operations to ensure that data acquisition, scale mapping, and the construction of composite splices are unequivocal (see "IODP Depth Scales Terminology" at **www.iodp.org/program-policies/**).

The primary depth scales are measured by the length of drill string (e.g., drilling depth below rig floor [DRF] and drilling depth below seafloor [DSF]), core recovered (e.g., core depth below seafloor [CSF] and core composite depth below seafloor [CCSF]), and logging wireline (e.g., wireline log depth below rig floor [WRF] and wireline log depth below seafloor [WSF]). In cases where multiple logging passes are made, wireline log depths are mapped to one reference pass, creating the wireline log matched depth below seafloor (WMSF). All units are in meters. The relationship between scales is defined either by protocol, such as the rules for computation of CSF from DSF, or user-defined correlations, such as core-to-log correlation or stratigraphic correlation of cores between holes to create a common CCSF scale from the CSF scale used in each hole. The distinction in nomenclature should make the reader aware that the same depth value in different depth scales usually does not refer to exactly the same stratigraphic interval.

During Expedition 344, unless otherwise noted, depths below rig floor were calculated as DRF and are reported as mbrf, core depths below seafloor were calculated as CSF-A and are reported as mbsf, and downhole wireline depths were calculated as WMSF and are reported as mbsf.

Curatorial procedures and sample depth calculations

Numbering of sites, holes, cores, and samples followed standard IODP procedure. A full curatorial identifier for a sample consists of the following information:

expedition, site, hole, core number, core type, section number, section half, piece number (hard rocks only), and interval in centimeters measured from the top of the core section. For example, a sample identification of "344-U1412A-2H-5W, 80–85 cm," indicates a 5 cm sample removed from the interval between 80 and 85 cm below the top of Section 5 (working half) of Core 2 of Hole A at Site U1412 during Expedition 344 (Fig. F1). The drilling system used to obtain a core is designated by the core type: H = APC, X = XCB, and R = RCB. The "U" preceding the hole number indicates the hole was drilled by the U.S. Implementing Organization (USIO) platform, the R/V *JOIDES Resolution*.

The depths of core intervals are defined by the length of drill string, the seafloor depth, and the amount the driller advanced the core barrel. The length of the core is defined by the sum of the lengths of the core sections. The CSF depth of a sample in a section is calculated by adding (1) the core-top depth measured with the drill string, (2) the lengths of all higher sections in the core, and (3) the offset of the sample below the section top. A soft to semisoft sediment core from less than a few hundred meters below seafloor expands upon recovery (typically a few percent to as much as 15%), so the recovered interval may not match the cored interval. In addition, a coring gap typically occurs between cores. Thus, a discrepancy between DSF and CSF depths can exist with regard to a stratigraphic interval. Furthermore, when core recovery is >100% of the cored interval, a sample taken from the bottom of a core will have a CSF depth deeper than that of a sample from the top of the subsequent core (i.e., the data associated with the two core intervals overlap on the CSF-A scale).

If a core has incomplete recovery, for curation purposes all cored material is assumed to originate from the top of the drilled interval as a continuous section; the true depth interval within the cored interval is unknown. This should be considered a sampling uncertainty in age-depth analysis or correlation of core data with downhole logging data.

Core handling and analysis

Cores were extracted from the core barrel in plastic liners. The liners were carried from the rig floor to the core processing area on the catwalk outside the core laboratory, where they were split into ~1.5 m sections. Blue (uphole) and clear (downhole) liner caps were attached with acetone onto the cut liner sections.

Sediment

As soon as cores arrived on deck, core catcher samples were taken for biostratigraphic analysis. Once the cores were cut into sections, whole-round samples were taken for shipboard interstitial water analyses and postcruise microbiological studies. When a whole-round sample was removed, a yellow cap was used to denote the missing interval. Gas samples were taken using a syringe for hydrocarbon analysis as part of the shipboard safety protocol. Syringe samples were also taken for shore-based microbiology analyses. See Figure F2 for a schematic of core flow through the laboratories.

Core sections were placed in core racks in the laboratory. When the cores reached equilibrium with laboratory temperature (typically after 3 h), whole-round core sections were run through the Whole-Round Multisensor Logger (WRMSL) for *P*-wave velocity, magnetic susceptibility, and bulk density measurements. In some cases, whole-round samples were taken for anelastic strain recovery analyses following this step. Whole-round core sections were run through the Natural Gamma Radiation Logger (NGRL). Additional whole-round samples were taken for shore-based physical properties analyses. Thermal conductivity measurements were made at varying intervals (see **"Physical properties"**).

Sediment cores were split lengthwise from bottom to top into working and archive halves. Investigators should note that older material may have been transported upward on the split face of each section during splitting.

The working half of each core was first described by the structural geologists. Samples were taken first for discrete physical properties and paleomagnetic analyses, followed by samples taken for shore-based studies based on the sampling plan agreed upon by the science party and shipboard curator and for remaining shipboard analyses such as bulk X-ray diffraction and carbonate.

The archive half of each core was scanned on the Section Half Imaging Logger (SHIL) and measured for color reflectance and point magnetic susceptibility on the Section Half Multisensor Logger (SHMSL). Labeled foam pieces were used in place of missing whole-round intervals in the SHIL images. Archive halves were then described visually and by means of smear slides. Finally, the magnetization of archive halves and discrete pieces was measured with the cryogenic magnetometer and spinner magnetometer.

Hard rocks

Pieces were pushed to the bottom of 1.5 m liner sections, and the total rock length was measured. The length was entered into the database using the SampleMaster application as "created length." This number was used to calculate recovery. Liner sections were then transferred to the core splitting room.

Whole-round samples were taken for postcruise microbiological and geochemical analyses following consultation with other members of the science party. Images were taken of these samples before they were bagged and processed. In cases where a whole-round sample was removed, a yellow cap was used to denote the missing interval.

Oriented pieces of core were marked on the bottom with a red wax pencil to preserve orientation. In several cases, pieces were too small to be oriented with certainty. Adjacent but broken pieces that could be fit together along fractures were curated as single pieces. The petrologist on shift confirmed piece matches and marked the split line on the pieces, which defined how the pieces were to be cut in two equal halves. The aim was to maximize the expression of dipping structures on the cut face of the core while maintaining representative features in both archive and working halves. A plastic spacer was secured with acetone to the split core liner between individual pieces or reconstructed contiguous groups of subpieces. These spacers may represent substantial intervals of no recovery. The length of each section of core, including spacers, was entered into the database as "curated length," which commonly differs by a few to several centimeters from the length measured on the catwalk. The database recalculated the depth of each piece based on the curated length.

Core sections were placed in core racks in the laboratory. When the cores reached equilibrium with laboratory temperature (typically after 3 h), whole-round core sections were run through the WRMSL and the NGRL.

Each piece of core was split with a diamond-impregnated saw into an archive half and a working half, with the positions of plastic spacers between pieces maintained in both halves. Pieces were numbered sequentially from the top of each section, beginning with 1. Separate subpieces within a single piece were assigned the same number but were lettered consecutively (e.g., 1A, 1B, 1C, etc.). Pieces were labeled on the outer cylindrical surface of the core. For oriented pieces, an arrow pointing to the top of the section was added to the label. The piece's orientation was recorded in the database using the SampleMaster application.

The working half of each core was first described by the structural geologists. Samples were taken for shipboard analyses, and thermal conductivity measurements were made on selected samples (see **"Physical properties"**).

The archive half of each core was scanned on the SHIL and measured for color reflectance and point magnetic susceptibility on the SHMSL. Archive halves were then described visually. Because there was insufficient time to produce and describe thin sections on board, thin section description was completed on shore and the data were entered into the database postcruise. Finally, the magnetization of archive halves and discrete pieces was measured with the cryogenic magnetometer and spinner magnetometer.

Sampling for shore-based studies was delayed until the end of coring. Sampling was conducted based on the sampling plan agreed upon by the science party and shipboard curator.

When all shipboard measurement steps were completed, cores were wrapped, sealed in plastic tubes, and transferred to cold storage aboard the ship. At the end of the expedition, the cores were kept on the ship, and at the conclusion of Expedition 345 and the transit to Victoria, British Columbia (Canada), they were transferred into refrigerated trucks and transported to cold storage at the IODP Gulf Coast Repository in College Station, Texas (USA).

Core sample disturbance

Cores may be significantly disturbed and contain extraneous material as a result of the coring and core handling process. In formations with loose sand layers, sand from intervals higher in the hole may be washed down by drilling circulation, accumulate at the bottom of the hole, and be sampled with the next core. The uppermost 10–50 cm of each core must therefore be examined critically during description for potential "fall-in." Common coring-induced deformation includes the concave-downward appearance of originally horizontal bedding. Piston action may result in fluidization ("flow-in") at the bottom of APC cores. Retrieval from depth to the surface may result in elastic rebound. Gas that is in solution at depth may become free and drive apart core segments within the liner. When gas content is high, pressure must be relieved for safety reasons before the cores are cut into segments. This is accomplished by drilling holes into the liner, which forces some sediment out of the liner along with the gas. These disturbances are described in each site chapter and graphically indicated on the visual core descriptions (VCDs or "barrel sheets").

Authorship of methods and site chapters

The separate sections of the site chapters were written by the following scientists (authors are listed in alphabetical order; see **"Expedition 344 science party"** for contact information):

Background and Objectives: Harris, Sakaguchi
Operations: Midgley, Petronotis
Lithostratigraphy and Petrology: Charpentier, Heydolph, Kutterolf, Millan, Nascimento, Smith-Duque, Straub, Yan

Paleontology and Biostratigraphy: Baxter, Burkett, Diz Ferreiro, Sandoval Gutierrez, Uchimura

Structural Geology: Kurz, Sakaguchi, Vannucchi, Yamamoto

Geochemistry: Berg, Choi, Heydolph, Kastner, Solomon, Torres

Physical Properties: Hamahashi, Harris, Hashimoto, Martin, Saito, Screaton, Tanikawa

Paleomagnetism: Jovane, Li, Petronotis, Zhao

Downhole Logging: Malinverno, Saito

Lithostratigraphy and petrology

This section outlines the procedures used to document the sedimentary and igneous composition, texture, and fabric of geologic material recovered during Expedition 344. These procedures included visual core description, smear slide and petrographic thin section description, digital color imaging, color spectrophotometry, and X-ray diffraction (XRD). Because many of the geologic techniques and observations used to analyze sedimentary cores are similar to those used to analyze igneous basement cores, both methods are presented together. However, as conditions warranted, different procedures were used to characterize sedimentary and crystalline basement rocks; these distinctions are also provided.

All instrument data from Expedition 344 were uploaded into the IODP-USIO Laboratory Information Management System (LIMS), and core description observations were entered using the DESClogik application (**iodp.tamu.edu/tasapps/**). DESClogik is a visual core description program used to store a visual (macroscopic and/or microscopic) description of core structures at a core (sediment) or section (igneous basement) scale. Core description data are available through the "Descriptive Information" LIMS Report (**web.iodp.tamu.edu/DESCReport/**).

We used the archive halves of core sections to make sedimentary and petrographic observations and interpretations. Sections dominated by soft sediment were split using a thin wire held in high tension. Recovered hard rock was split with a diamond-impregnated saw. Cuts were oriented so that important compositional and structural features were preserved in both the archive and working halves. The split surface of the archive half of sedimentary rocks was then assessed for quality (e.g., smearing or surface unevenness) and, if necessary, gently scraped with a glass slide or spatula. After splitting, the archive half was imaged using the SHIL and then analyzed for color reflectance and magnetic susceptibility using the SHMSL (see **"Physical properties"**). The archive-half section was occasionally reimaged when visibility of sedimentary structures or fabrics improved following treatment of the split core surface.

Following imaging, the archive-half sections of the sediment cores were macroscopically described for lithologic and sedimentary features. Lithostratigraphic units were characterized by visual inspection, and smear slide observations were used to determine microfossil and sedimentary constituents and abundances to aid in lithologic classification. Cores from the basement were also described visually and subsequently with the aid of thin sections for primary igneous features and secondary alteration features. The majority of thin sections were described on shore following the expedition due to time constraints. Based on preliminary visual descriptions and physical properties data, thin section samples and samples for XRD were extracted from the working-half sections. All descriptions and sample locations were recorded using curated depths (CSF-A) and documented on VCD graphic reports (Fig. **F3**).

Visual core descriptions for sediment

Color and composition

Color was determined qualitatively for core intervals using Munsell Color Charts (Munsell Color Company, Inc., 2000). Visual inspections of archive-half sections were used to identify compositional and textural elements of the sediment, including sediment structures and components such as concretions, nodules, chert, rock fragments, and tephra.

To emphasize the different compositions of volcanic sandstones, rocks were classified using a scheme after Fisher and Schmincke (1984). In general, coarser grained sedimentary rocks (63 µm to 2 mm average grain size) are designated as "sand(stone)" where volcanoclastic components are <25% of the total clasts. Volcanoclastics can be (1) reworked and commonly altered heterogeneous assemblages of volcanic material like lava and tuff fragments, as well as compositionally different ash lenses/particles, or (2) fresh or less altered compositionally homogeneous loose pyroclastics resulting directly from explosive eruptions on land or effusive/explosive vents on the seafloor. Pyroclasts are made out of volcanogenic material (Greek "pyro" = fire or magma) that is fragmented (Greek "clast" = broken in pieces) during explosive eruptions.

In a given sediment/sedimentary rock, if ≥25% volcanoclasts but <25% pyroclasts are observed, it is designated as a "volcanoclastic sand(stone)." If the clast composition is 25%–75% pyroclasts, the sediment/sedimentary rock is classified as "tuffaceous sand(stone)," but if clast composition is ≥75% pyroclasts, the rock/sediment is classified as a "tuff" or

"tephra," respectively. Depending on grain size and degree of compaction, the nomenclature is adjusted accordingly, as shown in Table T1.

Textures, structures, and sedimentary fabric

When visible at low magnifications, sediment grain size was determined using the Wentworth scale (Wentworth, 1922). Grain size, particle shape, and sorting were also noted; however, these textural attributes required inspection at high magnification and were only performed on smear slides and thin sections (see below).

Sedimentary structures observed in recovered cores included bedding, soft-sediment deformation, bioturbation, and early diagenetic mineral authigenesis. Bed thickness was defined according to Boggs (2005):

Very thick bedded = >100 cm.
Thick bedded = 30–100 cm.
Medium bedded = 10–30 cm.
Thin bedded = 3–10 cm.
Very thin bedded = 1–3 cm.
Laminae = <1 cm.

Some samples were inspected with a 10× hand lens for micrograded bedding (i.e., graded bedding occurring within laminations) and indications of preferred particle orientations, including lineation and imbrication of elongated detrital and biogenic material.

Estimations in abundances of components were made semiquantitatively using the following scheme:

R = rare (<1 vol%).
C = common (1–10 vol%).
A = abundant (10–50 vol%).
D = dominant (50–80 vol%).
M = major (>80 vol%).

The abundance of bioturbation was measured using the semiquantitative ichnofabric index as described by Droser and Bottjer (1986, 1991) and with the help of visual comparative charts (Heard and Pickering, 2008). The indexes refer to the degree of biogenic disruption of primary fabric such as lamination and range from 1 for nonbioturbated sediment to 6 for total homogenization:

1 = no bioturbation recorded; all original sedimentary structures preserved.
2 = discrete, isolated trace fossils; as much as 10% of original bedding disturbed.
3 = ~10%–40% of original bedding disturbed; burrows are generally isolated but locally overlap.
4 = last vestiges of bedding discernable; ~40%–60% disturbed; burrows overlap and are not always well defined.
5 = bedding is completely disturbed, but burrows are still discrete in places and the fabric is not mixed.
6 = bedding is nearly or totally homogenized.

Additionally, the inventory of ash layers, pods, and dispersed ash layers was documented separately to describe their textural and structural occurrence within the sedimentary column. Detailed results are given in the tephra log (see "Core descriptions").

Smear slides and thin sections

Smear slides and thin sections are useful for identifying and reporting basic textural and compositional attributes, even if the results are only semiquantitative. We estimated the texture of the sediment with the help of a visual comparison chart (Rothwell, 1989). However, errors can be large, especially for fine silt and clay-sized fractions. Smear slide analysis also tends to underestimate the amount of sand-sized grains because they are difficult to incorporate evenly onto the slide. Nevertheless, in order to define unit boundaries and subunits, smear slides are the most efficient way to evaluate differences in lithology, textures, and composition on board semiquantitatively using a point counting method.

When point-counts were conducted, we used four different predefined rectangles, randomly distributed over the slide, and counted every component in this area at 100× to 200× magnification until 200 points were reached (e.g., Galehouse 1969, 1971). This is a relatively imprecise method compared to the normal net-based point counting method; however, it is quick and works well for sandstone and sandy siltstone. The theoretical 2σ error for a total of 200 counted particles is between 3% and 7%, depending on the portion of the total inventory (van der Plas and Tobi, 1965). The various components were then binned into several categories (e.g., feldspar, pyroxene, metamorphic lithics, sedimentary lithics, etc.) to facilitate the optimum reproducibility among different scientists (see smear slides in "Core descriptions").

For fine sediment (silt and silty claystone), rough estimations were made regarding the matrix using the visual comparison chart from Rothwell (1989). These estimates were supplemented with point counting of the coarser fraction. Coarse and fine fractions were subsequently combined and normalized to 100% of the total component inventory. Because most of the point counting is based on estimates, the 2σ error for the finer sediment is much higher and must be considered when interpreting the results; overall trends, especially for coarser grains, are considered more reliable.

Detailed results are summarized in the smear slides (see "Core descriptions"). The relative abundance of major components was also validated by XRD (see "X-ray diffraction"), and the absolute weight percent of carbonate was verified by chemical analysis (see "Sediment geochemistry").

The sample location of each smear slide and thin section is shown in the Shipboard samples column of the VCDs.

X-ray diffraction

We completed routine XRD analyses of bulk powder using a Bruker D-4 Endeavor diffractometer mounted with a Vantec-1 detector using nickel-filtered Cu-Kα radiation. Our principal goal was to identify the different minerals that are present in the sediments of the different lithologic units. We also estimate relative percentages of major components—total phyllosilicate minerals, quartz, plagioclase, and calcite—using peak areas.

Most samples were selected from intervals adjacent to whole-round samples, and most are part of clusters with physical properties and carbonate samples. A few additional samples were collected periodically when there were lithology changes. Samples were freeze-dried, crushed using a mortar and pestle (along with powder for X-ray fluorescence and carbonate), and mounted as random bulk powder. Standard locked coupled scan conditions were as follows:

Voltage = 40 kV.
Current = 35 mA.
Goniometer scan 2θ = 4°–70°.
Step size = 0.0174°.
Scan rate = 1 s/step.
Divergence slit = 0.6 mm.

Diffractograms of single samples were evaluated with the Bruker DiffracPlus Evaluation software package (EVA).

The upper and lower limits of each peak on the diffractogram (Fig. **F4**) were adjusted following the guidelines shown in Table **T2,** where the peak areas used for calculations of relative mineral abundances are given. As calibration was not performed, mineral proportions should only be used to assess the variation of the relative proportion of a four-component system where phyllosilicate minerals + quartz + plagioclase + calcite = 100%. The quality of these estimates relative to the absolute percentages within the mass of total solids depends on the abundance of amorphous solids (e.g., biogenic opal and volcanic glass), as well as the total of all other minerals that occur in minor or trace quantities. Thus, the primary value of bulk powder XRD data should only be to identify spatial and temporal trends in sediment composition and to assist with core-log integration.

Hard rock description

Mineralogy and unit classification

In order to preserve important features and structures, all cores were visually examined before splitting. Large pieces of hard rock core were marked on the bottom with a red wax pencil to preserve orientation when they were removed from the split core liner. Each piece was numbered sequentially from the top of the core section and labeled on the outside surface. Broken core pieces that could be fitted together along fractures were assigned the same number and lettered consecutively from the top down (e.g., 1A, 1B, 1C, etc.). Plastic spacers were placed between pieces with different numbers; however, the presence of a spacer may represent a substantial interval without recovery. Fitted core pieces and fragile pieces were wrapped together with shrink wrap prior to splitting the core into archive and working halves. To determine the most appropriate split line, the morphology of magmatic contacts, veins, lava, and porphyroclastic flows were initially identified on the whole-round cores. Additionally, all pieces that could be confidently joined were aligned.

All subsequent shipboard characterization of hard rocks was based on visual core description and thin section analysis, and hard rock core descriptions and associated shipboard analyses were archived electronically in DESClogik. First-order identification of rock type, primary igneous textures, and alteration (veins, halos, breccia, and vesicle fill) was carried out by visual observation using a hand lens (10×) and a binocular microscope. Observations including petrographic texture, grain size, groundmass mineralogy, phenocryst mineralogy, and alteration mineralogy were determined by thin section analysis. Thin section descriptions were utilized as a point of reference from which more precise hand specimen descriptions could be made. Where possible, point counting using an automated stepping stage was carried out to estimate groundmass compositions. Phenocryst crystal habit and size (minimum, maximum, and mode) were estimated for each thin section. Mineral morphologies and textural features were also recorded. Whole-section digital photomicrographs in cross-polarized light and plane-polarized light were taken, and these, along with the thin section descriptions, are available in this volume and in the IODP database.

Classification of igneous units and subunits was based on variations in occurrence and abundance of primary mineralogy (e.g., phenocryst abundance), color, grain size, textural changes, the occurrence of chilled margins, or tectonic contacts. Where possible, a geological indicator is used to define a unit boundary (e.g., volcanic cooling margins); however, limited recovery lead to the emplacement of artificial boundaries where the units above and below are deemed sufficiently different. Subunit classifications were used to define zones of significant textural change, where appropriate. For phenocryst descriptions, the

most abundant type is named last during any written description. For example the most abundant mineral in a clinopyroxene-plagioclase phyric basalt is plagioclase. Definition limits are defined as follows:

Aphyric = <1% phenocrysts.
Sparsely phyric = 1%–5% phenocrysts.
Moderately phyric = 5%–10% phenorcysts.
Highly phyric = >10% phenocrysts.

Color was described visually on a wet cut rock surface. Wetting, using tap water and sponge, was kept to a minimum to minimize uptake of water by expanding clay minerals (smectite). Vesicle descriptions are described as follows:

Nonvesicular = <1%.
Sparsely vesicular = 1%–5%.
Moderately vesicular = 5%–20%.
Highly vesicular = >20%.

Breccia was described as basalt-clastic (i.e., clasts are formed in situ with a matrix composed of secondary minerals). This form of in situ brecciation may be considered an end-member that stems from vein-net, incipient brecciation (basaltic groundmass is nearly detached and surrounded by secondary minerals), followed by full brecciation (full detachment of basaltic fragments where they have been totally surrounded by secondary minerals). Groundmass grain size characterization includes the following:

G = glassy.
cx = cryptocrystalline, where groundmass crystals cannot be individually identified using a petrographic microscope.
mx = microcrystalline (~0.1–0.2 mm), in which groundmass is readily identifiable using a petrographic microscope.
fg = fine grained (0.2–1 mm).

Groundmass textures used during Expedition 344 include

Seriate (continuous range in grain size),
Porphyritic (high abundance of phenocrysts),
Glomeroporphyritic (clusters of phenocrysts),
Holohaline (100% glass),
Hypocrystalline (100% crystals),
Intersertal (cryptocrystalline to glassy infill of interstices between formed crystals within the groundmass),
Variolitic (fine radiating fibers of plagioclase and/or pyroxene), and
Ophitic and subophitic (lath-shaped euhedral crystals of plagioclase, grouped radially or in an irregular mesh, with a surrounding or interstitial crystals of pyroxene).

Alteration

Alteration from basement recovered during Expedition 344 was defined as (1) background alteration, (2) alteration halos, (3) veins and vein nets (where veining was numerous), (4) secondary minerals filling vesicles, and (5) basaltic breccia. Alteration features were recorded into the DESClogik program as separate logs. Levels of background alteration were defined following the convention in Figure **F5.** Vein mineralogy, orientation, width, shape, and location were recorded. Where possible, the order of infill for vesicles and veins was determined; in addition, halos and vesicle size, color, shape, and secondary mineralogy was described. Overprinting or crosscutting of veins, minerals within veins, and halos were noted. Thin sections were used to determine secondary mineralogy and describe the timing and method of secondary mineral emplacement through crosscutting relationships observed in veins, vesicles, and alteration halos. Glass was recorded in terms of percent fresh and percent altered.

Visual Core Descriptions for hard rock

VCD forms were used to describe each hard rock core. A key to the symbols used on the hard rock VCDs is given in Figure **F5.** On the VCDs, the following information is displayed from left to right:

Section depth,
Piece number,
Photograph of the archive half of the core,
Piece orientation if known,
Shipboard studies,
Lithologic unit,
Igneous textures,
Primary phenocryst minerals and abundance,
Measured structures,
Dip,
Alteration intensity,
Presence of veins,
Magnetic susceptibility, and
Unit description.

The unit summary, located on the right-hand side of the VCD includes the following information

1. Unit number,
2. Lithology,
3. Volcanic description,
4. Texture,
5. Color,
6. Phenocryst description,
7. Groundmass comments,
8. Vesicle comments,
9. Upper and lower contact comments,
10. Alteration summary,
11. Summary of veins, and
12. Summary of structures.

In instances where an individual rock fragment could not have rotated about a horizontal axis during drilling, an arrow pointing to the top of the section is shown in the Orientation column. The term "vein" describes filled crosscutting fractures and includes breccia, cataclastic injections, epigenetic mineralized veins, shear veins, and vein networks. Vein geometry and mineralogy is given in detail in the additional comments. Comments also include accessory mineral occurrences.

Paleontology and biostratigraphy

Paleontologic investigations carried out during Expedition 344 focused primarily on calcareous nannofossils, radiolarians, and benthic foraminifers. Preliminary biostratigraphic determinations were based on nannofossil and radiolarian assemblages.

Calcareous nannofossils

Calcareous nannofossil assemblages were examined and described from smear slides made from core catcher samples. Standard smear slide techniques were utilized for immediate biostratigraphic examination. In order to process a sample, a small portion of sediment was placed directly on a glass coverslip. A drop of distilled water was added, and the sediment was evenly spread across the coverslip using a flat-sided toothpick. The coarser grained fraction was removed during this process. The coverslip was then dried on a hot plate. After drying, it was mounted onto a glass microscope slide with Norland optical adhesive (Number 61) and placed under a UV lightbulb until the adhesive hardened. All samples were examined using a Zeiss Axiophot light microscope with an oil immersion lens. Phase contrast, brightfield, and cross-polarized light, all under magnifications of 400×, 630×, and 1000×, were used. Photomicrographs were taken using a Spot RTS system with Image Capture and Spot software.

Relative abundances of calcareous nannofossils were determined using the criteria defined below:

D = dominant (>90% of sediment particles).
A = abundant (50%–90%) of sediment particles.
C = common (10%–50% of sediment particles).
F = few (1%–10% of sediment particles).
R = rare (<1% of sediment particles).
B = barren (no specimen).

Species abundances were determined using the criteria defined below:

D = dominant (>100 specimens per field of view at 1000× magnification).
A = abundant (10–100 specimens per field of view at 1000× magnification).
C = common (1–10 specimens per field of view at 1000× magnification).
Freq = frequent (1 specimen per 1–10 fields of view at 1000× magnification).
R = rare (<1 specimen per 10 fields of view at 1000× magnification).

The following basic criteria were used to qualitatively provide a measure of preservation of the nannofossil assemblage:

G = good (little or no evidence of dissolution and/or recrystallization; primary morphological characteristics only slightly altered; all specimens identifiable at the species level).
M = moderate (some etching and/or recrystallization; primary morphological characteristics partially altered; most specimens not identifiable at the species level).
P = poor (specimens severely etched or overgrown; primary morphological characteristics largely destroyed; fragmentation evident; most specimens not identifiable at the species and/or generic level).

The standard nannofossil zonations of Martini (1971), Bukry (1973, 1975), and Okada and Bukry (1980) were utilized during the study to evaluate nannofossil age datums. The website Nannotax (**www.nannotax.org/**) was consulted to find updated nannofossil genera and species ranges. The zonal scheme of Martini (1971) was selected for the range-distribution chart, and this zonal scheme was correlated to the Gradstein et al. (2012) geological timescale. Determinations on the degree of preservation and group and species abundances were recorded in DESClogik and uploaded to the LIMS database.

Radiolarians

Radiolarian assemblages were examined and described from core catcher samples using smear slides. Core catcher samples were first soaked in 10% HCl to dissolve the calcium carbonate component of the sample (determined through the reactivity of the mixture). The residue was sieved over a 63 µm mesh, soaked in H_2O_2 (hydrogen peroxide) to remove any organic material present, and sieved a second time. A portion of the residue was placed directly onto a glass coverslip and spread evenly across the surface using a flat-sided toothpick. The coverslip was then dried on a hot plate. After drying, the coverslip was mounted onto a glass microscope slide with Norland optical adhesive (Number 61) and placed under a UV lightbulb until hardened. Samples were examined using a Zeiss Axioscope. Phase contrast, brightfield,

and cross-polarized light, all under magnifications of 10× and 100×, coupled with a photomicrograph camera system were used.

Relative abundances of radiolarian assemblages were determined using the method below:

A = abundant (>200 specimens per slide traverse).
C = common (50–200 specimens per slide traverse).
F = few (1–49 specimens per slide traverse).
N = none (0 specimens per slide traverse).

The following criteria were used to categorize relative abundances of radiolarian species per sample:

A = abundant (>30 specimens per slide traverse).
C = common (>6–30 specimens per slide traverse).
F = few (>1–5 specimens per slide traverse).

The following basic criteria were used to qualitatively provide a measure of preservation of the radiolarian assemblage:

VG = very good (no evidence of overgrowth, dissolution, or abrasion).
G = good (little evidence of overgrowth, dissolution, or abrasion).
M = moderate (common calcite overgrowth, dissolution, or abrasion).
P = poor (substantial overgrowth or infilling, dissolution, or fragmentation).

Sanfilippo and Nigrini (1998), Nigrini and Moore (1979), Takahashi (1991), and Riedel and Sanfilippo (1970) were used for taxonomic identification. Low-latitude zonation was assigned based on Sanfilippo and Nigrini (1998) and Sanfilippo et al. (1985). These datums were correlated to the Gradstein et al. (2012) geological timescale.

Benthic foraminifers

Core catcher samples were processed following routine methods for the study of foraminifers. Core catcher samples were first sieved with tap water over 125 and 63 µm mesh sieves, and the residue was dried on filter paper in a low-temperature oven at ~60°C. If the samples were indurated, they were first soaked in water and then in H_2O_2 (3%–5%) to further disaggregate the sediment before sieving took place. To minimize contamination of foraminifers between samples, the sieves were placed in an ultrasonic bath for several minutes and thoroughly checked between each sample to prevent contamination.

Species identifications for benthic foraminifers were made on the >125 µm size fraction and examined under a binocular microscope. Where possible, at least 150 specimens were picked, identified, and counted to determine benthic foraminiferal relative abundances. Planktonic foraminifers were not identified to species level but were used in planktonic to benthic ratio (P/[P + B]) determinations for each sample to evaluate relative changes in paleobathymetry (Ingle et al., 1980). Determinations on the degree of preservation and species counts were entered into DESClogik and uploaded into the LIMS database.

Relative abundances of benthic foraminifers were determined using the criteria defined below:

D = dominant (>30% of the >125 µm size fraction).
A = abundant (20%–30% of the >125 µm size fraction).
C = common (10%–20% of the >125 µm size fraction).
F = few (5%–10% of the >125 µm size fraction).
R = rare (1%–5% of the >125 µm size fraction)
P = present (<1% of the >125 µm size fraction).

The preservation status of benthic foraminifers was estimated as follows:

G = good (little or no evidence of dissolution and/or secondary overgrowth of calcite; diagnostic characters fully preserved).
M = moderate (dissolution and/or secondary overgrowth present; partially altered primary morphological characteristics; nearly all specimens can be identified at the species level).
P = poor (severe dissolution, fragmentation, and/or secondary overgrowth with primary features largely destroyed; many specimens cannot be identified at the species level and/or generic level).

Benthic foraminiferal taxonomy and paleodepth determination

Genera were assigned following Loeblich and Tappan (1988), and the standard foraminifer literature was consulted for species identification. Ecological and paleobathymetric interpretations are based on a compilation of ecological data, including, but not limited to, the equatorial Pacific, such as Bandy and Arnal (1957), Crouch and Poag (1987), Heinz et al. (2008), and Smith (1963, 1964).

Structural geology

Our methods for documenting the structural geology of Expedition 344 cores largely followed those used by Expedition 334 structural geologists (see "Structural geology" in the Expedition 334 "Methods" chapter [Expedition 334 Scientists, 2011]). We documented deformation observed on the working half of the split cores by classifying structures, determining the depth extent, measuring orientation data, and recording the sense of displacement. The collected data were hand-logged onto a printed form at the core table and then typed into both a spreadsheet

and DESClogik. Where possible, orientation data were also corrected for rotation related to drilling on the basis of paleomagnetic declination and inclination information.

Structural data acquisition and orientation measurements

Each structure was recorded manually on a description table sheet modified from that used during Expedition 334 (Fig. F6). Core measurements followed those made during IODP Expeditions 315 and 316, which in turn were based on previous ODP procedures developed at the Nankai accretionary margin (Legs 131 and 190). We used a plastic protractor for orientation measurements (Fig. F7). Using the working half of the split core provided greater flexibility in removing—and cutting, if necessary—pieces of the core for measurements.

Orientations of planar and linear features in cored materials were determined relative to the core axis, which represents the vertical axis in the core reference frame, and the double line marked on the working half of the split core liner, which represents 0° (and 360°) in the plane perpendicular to the core axis (Fig. F8). To determine the orientation of a planar structural element, two apparent dips of the element were measured in the core reference frame and converted to a plane represented by dip angle and either a strike or dip direction (Fig. F9). One apparent dip is usually represented by the intersection of the planar feature with the split face of the core and is quantified by measuring the dip direction and angle in the core reference frame (β_1; Fig. F10). Typical apparent dip measurements have a trend of 90° or 270° and range in plunge from 0° to 90°. The second apparent dip is usually represented by the intersection of the planar feature and a cut or fractured surface at a high angle to the split face of the core (β_2; Fig. F10). In most cases, this was a surface either parallel or perpendicular to the core axis. In the former cases, the apparent dip lineation would trend 000° or 180° and plunge from 0° to 90°; in the latter cases, the trend would range from 000° to 360° and plunge 0°. Linear features observed in the cores were always associated with planar structures (e.g., striations on faults), and their orientations were determined by measuring either the rake (or pitch) on the associated plane or the trend and plunge in the core reference frame. During Expedition 344, we measured rake for striations on the fault surface (Fig. F11) and azimuth and plunge for other lineations (e.g., fold axes). All data were recorded on the log sheet with appropriate depths and descriptive information.

Paleomagnetic correction

Paleomagnetic data were used during Expedition 344 to restore the structural data with respect to the geographic reference system (Fig. F9). Especially in the XCB and RCB intervals, drilling-induced biscuiting of the cores and individual rotation of each core biscuit require paleomagnetic reorientation to correct the structural data. Because APC cores are continuous, we used the orientation data from discrete paleomagnetic samples or from the orientation tool attached to the APC to restore all structural data collected from the same core. Because each biscuit can rotate independently in the XCB and RCB cores, a discrete paleomagnetic correction for each biscuit was needed. We therefore recorded intact and undisturbed intervals without internal biscuiting for paleomagnetic correction when we identified structures. We collected paleomagnetic measurement samples from the same coherent core piece in which structures were measured. After paleomagnetic measurements were made, we oriented the structural data using the declination of the characteristic remanence of magnetization (see **"Paleomagnetism"**).

Description and classification of structures

We constructed a structural geology template for DESClogik that facilitated the description and classification of observed structures. For clarity, we defined the terminology used to describe fault-related rocks, as well as the basis for differentiating natural structures from drilling-induced features.

Faults were classified into several categories based on the sense of fault slip and their structural characteristics. The sense of the fault slip was identified using offsets of markers (e.g., bedding and older faults) across the fault plane and predominantly by slicken steps. A fault with cohesiveness across the fault zone was described as a healed fault. Zones of dense fault distribution and intense deformation were described as brecciated zones and fractured zones. Fractured zones are moderately deformed zones where the size of fragments is usually bigger than the width of the core; brecciated zones are intensively deformed zones fragmented into centimeter-size and smaller fragments, containing a few larger fragments. A zone of strong localized deformation delimited by material with lower finite deformation was described as a shear zone.

In the basement rocks, igneous rocks and tectonic mélanges were expected to correspond to the onshore geological map of Osa Peninsula. The lithology and mineralogy of the vein minerals were described by the petrologists, and orientations of the veins, foliations, and other structural features in the igneous rocks were measured by the shipboard structural geologists.

Structures can sometimes be disturbed by drilling-induced deformation such as flow-in structures in APC cores and biscuiting, fracturing, faulting, and rotation of fragments in XCB and RCB cores. In the cases where structures have been disturbed by flow-in on >60% of the cross section of the core, we excluded measurements because of the intense disturbance (bending, rotation, etc.) of these structures. We used paleomagnetic data to correct for possible rotations of the fault orientation caused by coring. When multiple orientation measurements were plotted in stereographic projection, natural faults were expected to display preferred orientations that were possibly related to tectonic stress orientations, whereas drilling-induced fractures were expected to yield random orientation distributions.

Calculation of plane orientation

For planar structures (e.g., bedding or faults), two apparent dips on two different surfaces (e.g., the split core surface, which is east–west vertical, and the horizontal or north–south vertical surface) were measured in the core reference frame as azimuths (measured clockwise from north, looking down) and plunges (Figs. F8, F9, F10). A coordinate system was defined in such a way that the positive *x*-, *y*-, and *z*-directions coincide with north, east, and vertical downward, respectively. If the azimuths and plunges of the two apparent dips are given as (α_1, β_1) and (α_2, β_2), respectively, as in Figure F10, then the unit vectors representing these two lines, v_1 and v_2, are

$$v_1 = \begin{pmatrix} l_1 \\ m_1 \\ n_1 \end{pmatrix} = \begin{pmatrix} \cos\alpha_1 \cos\beta_1 \\ \sin\alpha_1 \cos\beta_1 \\ \sin\beta_1 \end{pmatrix}$$

and

$$v_2 = \begin{pmatrix} l_2 \\ m_2 \\ n_2 \end{pmatrix} = \begin{pmatrix} \cos\alpha_2 \cos\beta_2 \\ \sin\alpha_2 \cos\beta_2 \\ \sin\beta_2 \end{pmatrix}.$$

The unit vector normal to the plane, v_n (Fig. F10), is then defined as

$$v_n = \begin{pmatrix} l_n \\ m_n \\ n_n \end{pmatrix} = \frac{v_1 \times v_2}{|v_1 \times v_2|},$$

where

$$v_1 \times v_2 = \begin{pmatrix} \begin{vmatrix} m_1 & m_2 \\ n_1 & n_2 \end{vmatrix} \\ \begin{vmatrix} n_1 & n_2 \\ l_1 & l_2 \end{vmatrix} \\ \begin{vmatrix} l_1 & l_2 \\ m_1 & m_2 \end{vmatrix} \end{pmatrix} = \begin{pmatrix} m_1 n_2 - m_2 n_1 \\ n_1 l_2 - n_2 l_1 \\ l_1 m_2 - l_2 m_1 \end{pmatrix}.$$

The azimuth, α_n, and plunge, β_n, of v_n are given by

$$\alpha_n = \tan^{-1}\left(\frac{m_n}{l_n}\right), \beta_n = \sin^{-1} n_n.$$

The dip direction, α_d, and dip angle, β, of this plane are α_n and 90° + β_n, respectively, when β_n < 0° (Fig. F12). They are α_n ± 180° and 90° – β_n, respectively, when $\beta_n \geq 0°$. The right-hand rule strike of this plane, α_s, is then given by α_d – 90°.

Calculation of slickenline rake

For a fault with striations, the apparent rake angle of the striation, ϕ_a, was measured on the fault surface from either the 90° or 270° direction of the split-core surface trace (Figs. F9, F11). Fault orientation was measured as described above. Provided that v_n and v_c are unit vectors normal to the fault and split core surfaces, respectively, the unit vector of the intersection line, v_i, is perpendicular to both v_n and v_c (Fig. F11) and is therefore defined as

$$v_i = \begin{pmatrix} l_i \\ m_i \\ n_i \end{pmatrix} = \frac{v_n \times v_c}{|v_n \times v_c|},$$

where

$$v_c = \begin{pmatrix} 1 \\ 0 \\ 0 \end{pmatrix}$$

and

$$v_n \times v_c = \begin{pmatrix} \begin{vmatrix} m_n & 0 \\ n_n & 0 \end{vmatrix} \\ \begin{vmatrix} n_n & 0 \\ l_n & 1 \end{vmatrix} \\ \begin{vmatrix} l_n & 1 \\ m_n & 0 \end{vmatrix} \end{pmatrix} = \begin{pmatrix} 0 \\ n_n \\ -m_n \end{pmatrix}.$$

Knowing the right-hand rule strike of the fault plane, α_s, the unit vector, v_s, toward this direction is then

$$v_s = \begin{pmatrix} \cos\alpha_s \\ \sin\alpha_s \\ 0 \end{pmatrix}.$$

The rake angle of the intersection line, ϕ_i, measured from the strike direction, is given by

$$\phi = \cos^{-1}(v_s \times v_i)$$

because

$$v_s \times v_i = |v_s||v_i|\cos\phi_i = \cos\phi_i, \ \therefore |v_s| = |v_i| = 1.$$

The rake angle of the striation, ϕ, from the strike direction is $\phi_i \pm \phi_a$, depending on the direction from which the apparent rake was measured and the dip direction of the fault (Fig. F13). ϕ_a should be subtracted from ϕ_i when the fault plane dips west and ϕ_a was measured from either the top or 90° direction or when the fault plane dips east and ϕ_a was measured from either the bottom or 90° direction. On the other hand, ϕ_a should be added to ϕ_i when the fault plane dips east and ϕ_a was measured from either the top or 270° direction or when the fault plane dips west and ϕ_a was measured from either the bottom or 270° direction.

Azimuth correction using paleomagnetic data

Provided that a core is vertical, its magnetization is primary, and its bedding is horizontal, its paleomagnetic declination (α_p) indicates magnetic north when its inclination (β_p) $\geq 0°$, whereas α_p indicates magnetic south when $\beta_p < 0°$ (Figs. F9, F14). The dip direction and strike of a plane in the geographic reference frame, α_d* and α_s*, are therefore

$$\alpha_d^* = \alpha_d - \alpha_p$$

and

$$\alpha_s^* = \alpha_s - \alpha_p$$

when $\beta_p \geq 0°$ and are

$$\alpha_d^* = 180° + \alpha_d - \alpha_p$$

and

$$\alpha_s^* = 180° + \alpha_s - \alpha_p$$

when $\beta_p < 0°$.

If the core was complete and continuous, one paleomagnetism sample per section (1.5 m) was deemed sufficient. If the core was discontinuous, then each part of the core that was continuous and structurally important had to contain a paleomagnetism sample. Paleomagnetism samples were taken as cubic or cylindrical samples close to the measured faults (usually within 5 cm) and from a coherent interval that included the fault. We avoided core fragments which were so small that a spin around an axis significantly deviating from the core axis could have taken place (e.g., fragments of brecciated segments of the core).

DESClogik

DESClogik is an application used to store visual (macroscopic and/or microscopic) descriptions of core structures at a given section index. During this expedition, only the locations of structural features, calculated orientations in the core reference frame, and restored orientation based on the paleomagnetic data were input into DESClogik, and orientation data management and planar fabric analysis were recorded on a spreadsheet, as described above.

Geochemistry

The Costa Rica Seismogenesis Project (CRISP) was designed to help us understand the processes that control fault zone behavior during earthquake nucleation and rupture propagation at erosional subduction zones. The first phases of this project focused on sampling sediments, fluids, and crustal rocks to fully characterize the material before subduction. Fluids and associated diagenetic reactions are a key component of this study, as they affect hydrological parameters (e.g., permeability and pore pressure) and may regulate the mechanical state of the plate interface at depth. The concentration of dissolved species and their isotopic composition provide critical data for the identification of fluid sources, fluid-rock interaction, pathways of fluid migration, and plumbing of the system. In addition, geochemical data can help characterize the subsurface biosphere and aid in constraining the mass balance inventories operating in this subduction zone.

Sampling protocol

The majority of geochemistry samples were obtained from two general procedures. First, pore fluid whole-round samples were collected at a frequency of approximately three samples per core in the first three cores and, subsequently, two samples per core to the bottom of the hole, with higher resolution across zones suspected to be fluid conduits. The length of the whole rounds was 10 cm in the shallow cores and increased with depth, depending on pore fluid recovery, to a maximum of 50 cm. Second, dedicated whole-round samples were acquired at each site for He isotope analysis at depths across fluid conduits and/or above oceanic basement. Detailed sampling protocols for each site are given in the site chapters.

For headspace analyses of gas concentrations, two sediment plugs were routinely collected adjacent to each interstitial water sample; one was used for standard shipboard hydrocarbon concentration monitoring and the other for stable-isotope measurements at onshore laboratories. When present, void gases were sampled at the catwalk using a syringe attached to a stainless steel tool used to puncture the core liner, as described by Kvenvolden and McDonald (1986).

Pore fluid collection

For pore fluid analyses, whole-round cores were cut on the catwalk, capped, and taken to the laboratory for processing. In general, samples collected at all sites, between the seafloor and 50 mbsf, were processed inside a nitrogen bag to avoid oxidation of redox-sensitive elements; at Site U1381, whole rounds from the entire sediment section were processed inside a nitrogen bag. All other cores were processed under normal atmospheric conditions.

During high-resolution sampling or shallow-water coring, when the capacity to process pore fluid cores immediately after retrieval was exceeded, capped whole-round core sections were wrapped with electrical tape and stored under a nitrogen atmosphere at 4°C until they were squeezed, which occurred within 24 h of core retrieval.

After extrusion from the core liner, the surface of each whole-round interstitial water core sample was carefully scraped with a spatula to remove potential contamination from seawater and sediment smearing in the borehole. In APC cores, ~0.5 cm of material from the outer diameter and the top and bottom faces was removed, whereas in XCB and RCB cores, where borehole contamination is higher, as much as two-thirds of the sediment was removed from each whole round. The remaining sediment (~150–300 cm^3) was placed into a titanium squeezer, modified after the stainless steel squeezer of Manheim and Sayles (1974). Gauge forces up to a maximum 30,000 lb were applied using a laboratory hydraulic press to extract pore water. Most samples were squeezed at <20 MPa.

The squeezed pore fluids were filtered through a prewashed Whatman No. 1 filter placed in the squeezers, above a titanium screen. The squeezed pore fluids were collected in precleaned plastic syringes attached to the squeezing assembly and subsequently filtered through a 0.45 µm Gelman polysulfone disposable filter. In deeper sections, fluid recovery was as low as 2 mL after squeezing the sediment for as long as ~2 h.

Sample allocation was determined based on the pore fluid volume recovered and analytical priorities based on the objectives of the expedition. Shipboard analytical protocols are summarized in the following section.

Whole-round samples designated for He isotopic analysis were also cut on the catwalk and immediately transferred into a plastic sealable bag initially flushed with ultrahigh-purity N_2. Samples were taken to a special processing and squeezing station set up in the refrigerated core storage repository located on the lowermost deck of the *JOIDES Resolution*. This refrigerated repository is a He-free environment kept at 4°C, whereas the shipboard Chemistry Laboratory uses He as a carrier gas for the gas chromatographs, ion chromatograph, and CHNS elemental analyzer. The samples were cleaned in a glove bag, squeezed, transferred into copper tubing samplers that were previously flushed with ultrahigh-purity N_2, and crimped.

Shipboard pore fluid analyses

Pore fluid samples were analyzed on board following the protocols in Gieskes et al. (1991), Murray et al. (2000), and the IODP user manuals for new shipboard instrumentation, which were updated during this expedition.

Salinity, alkalinity, and pH

Salinity, alkalinity, and pH were measured immediately after squeezing, following the procedures in Gieskes et al. (1991). Salinity was measured using a Fisher temperature-compensated handheld refractometer. The pH was measured with a combined glass electrode, and alkalinity was determined by Gran titration with an autotitrator (Metrohm 794 basic Titrino) using 0.1 N HCl at 20°C. Certified Reference Material 104 obtained from the laboratory of Andrew Dickson, Marine Physical Laboratory, Scripps Institution of Oceanography (USA), was used for calibration of the acid. International Association for the Physical Sciences of the Oceans (IAPSO) standard seawater was used for calibration and was analyzed at the beginning and end of a set of samples for each site and after every 10 samples.

Chloride

High-precision chloride concentrations were acquired using a Metrohm 785 DMP autotitrator and silver nitrate ($AgNO_3$) solutions that were calibrated against repeated titrations of an IAPSO standard. In Hole U1381C, where fluid recovery was ample, a 0.5 mL aliquot of sample was diluted with 30 mL of a HNO_3 solution (92 ± 2 mM) and titrated with 0.1015 N $AgNO_3$. At all other sites, a 0.1 mL aliquot of sample was diluted with 10 mL of 90 ± 2 mM HNO_3 and titrated with 0.1778 N $AgNO_3$. Repeated analyses of an IAPSO standard yielded a precision better than 0.05%. Additionally, chloride concentrations were measured by IC using the third-party (Scripps Institute of Oceanography) Metrom 861.004 Advanced Compact ion chromatograph as described bellow for sulfate and bromide. These data have a precision of 0.15% and are included in the tables for comparison purposes.

Sulfate and bromide

Sulfate and bromide concentrations were determined with a third-party (Scripps Institute of Oceanography) Metrom 861.004 Advanced Compact ion chromatograph. The ion chromatograph included an MSM II suppressor module 46, 853 CO_2 suppressor, a thermal conductivity detector, and a Metrosep A Supp column. The eluent solutions used were 3.2 mM Na_2CO_3 and 1.0 mM $NaHCO_3$. Samples were diluted 1:50 with deionized water, using specifically designated pipettes. The analytical protocol was to run a standard after five samples for six cycles, after which three extra standards were analyzed. The standards used were based on IAPSO dilutions of 50×, 80×, 150×, 250×, 500×, 750×, and 1000×. Sample duplicates were analyzed during each run for reproducibility. Reproducibility was also checked based on the interspersed standard samples run throughout the expedition. Analytical precision was 0.3% for sulfate and 2% for bromide. Concentrations were based on peak areas.

In the uppermost ~50 m at each site, pore fluid aliquots for SO_4 and Br analyses were bubbled with He for as long as 2 min to remove sulfide that could oxidize to sulfate. The bubbled solutions were subsequently analyzed by the protocol described above. At each site, samples were run continuously as they were collected to monitor the location of the sulfate-methane transition zone (SMTZ) and any potential drill fluid contamination. Below the SMTZ, sulfate is depleted in the pore fluids, and any sulfate present in a sample is a result of contamination with surface seawater that was pumped down the hole while drilling. Based on the sulfate concentration of each interstitial water sample, we used the chemical composition of the surface seawater to correct each analysis for contamination using the following equations:

$$f_{SW} = [SO_4]_{meas}/[SO_4]_{SW},$$

$$f_{Pf} = 1 - f_{SW},$$

and

$$[X]_{corr} = [[X]_{meas} - (f_{SW} \times [X]_{SW})]/f_{Pf},$$

where f_{SW} is the fraction of a pore fluid sample that is contaminated with surface seawater and f_{PW} is the fraction of uncontaminated pore water in a sample. The subscripts SW, PF, and meas denote surface seawater, pore fluid, and measured, respectively. $[X]_{corr}$ is the corrected value of a solute (e.g., Cl, Ca, Sr, etc.), $[X]_{meas}$ is the measured concentration of that solute, and $[X]_{SW}$ is the concentration of the solute in surface seawater.

Because of the scientific importance of sulfate concentrations, pore fluid samples were also taken for shore-based analyses, and these were spiked with 100 µL 4 M $Cd(NO_3)_2$ solution to precipitate the sulfide as CdS.

Ammonium and phosphate

Ammonium concentrations were determined by spectrophotometry using an Agilent Technologies Cary Series 100 UV-Vis spectrophotometer with a sipper sample introduction system following the protocol in Gieskes et al. (1991). Samples were diluted prior to color development so that the highest concentration was <1000 µM. Phosphate was measured using the ammonium molybdate method described in Gieskes et al. (1991), using appropriate dilutions.

Major and minor elements

Major and minor elements were analyzed by inductively coupled plasma–atomic emission spectroscopy (ICP-AES) with a Teledyne Prodigy high-dispersion ICP spectrometer. The general method for shipboard ICP-AES analysis of samples is described in ODP *Technical Note* 29 (Murray et al., 2000) and the user manuals for new shipboard instrumentation, with modifications as indicated. Samples and standards were diluted 1:20 using 2% HNO_3 spiked with 10 ppm Y for trace element analyses (Li, B, Mn, Fe, Sr, Ba, and Si) and 1:100 for major constituent analyses (K, Ca, Mg, and SO_4). Each batch of samples run on the ICP spectrometer contains blanks and solutions of known concentrations. Each item aspirated into the ICP spectrometer was counted four times from the same dilute solution within a given sample run. Following each instrument run, the measured raw-intensity values were transferred to a data file and corrected for instrument drift and blank. If necessary, a drift correction was applied to each element by linear interpolation between the drift-monitoring solutions.

Standardization of major cations was achieved by successive dilution of IAPSO standard seawater to 120%, 100%, 75%, 50%, 25%, 10%, 5%, and 2.5% relative to the 1:100 primary dilution ratio. Analytical precision based on repeated analyses of the 100%, 75%, 50%, 25%, and 10% dilution standards over the 2 month expedition was Ca < 0.6%, Mg < 0.8%, Na < 2%, and K < 1.5%. Average accuracies of the analyses based on repeated analyses of 100% IAPSO run as an unknown throughout each batch of analyses were Ca < 1.5%, Mg < 1.5%, Na < 2.5%, and K < 2%.

For minor element concentration analyses, the interstitial water sample aliquot was diluted by a factor of

20 (0.5 mL sample added to 9.5 mL of a 10 ppm Y solution). Because of the high concentration of matrix salts in the interstitial water samples at a 1:20 dilution, matrix matching of the calibration standards is necessary to achieve accurate results by ICP-AES. A matrix solution that approximated IAPSO standard seawater major ion concentrations was prepared according to Murray et al. (2000). A stock standard solution was prepared from ultrapure primary standards (SPC Science PlasmaCAL) in a 2% nitric acid solution. The stock solution was then diluted in the same 2% ultrapure nitric acid solution to concentrations of 100%, 75%, 50%, 25%, 10%, 5%, and 1%. The calibration standards were then diluted using the same method as the samples for consistency. The final matrix-matched 100% standard solution contained the following concentrations of elements: B = 1388.9 µM, Li = 288.2 µM, Si = 1186.7 µM, Mn = 54.6 µM, Fe = 17.9 µM, Sr = 228.1 µM, and Ba = 36.4 µM. The 100%, 75%, 50%, 25%, 10%, and 5% standards were repeatedly analyzed with each batch and over the 2 month expedition as a check of analytical precision. The average precision of the minor element analyses were B < 1%, Ba < 1%, Mn < 1%, Li < 1.5%, Si < 1.5%, and Sr < 1%. Because values of many of these elements in IAPSO standard seawater are either below detection limits (e.g., Fe and Mn) or variable, the average accuracy of the analyses were determined by repeated analysis of the 75%, 25%, and 10% check standards and were B < 1.5%, Ba < 1.5%, Mn < 1.5%, Li < 1.5%, Si < 1.5%, and Sr < 2%. The precision and accuracy of the Fe analyses were deemed to be of insufficient quality, and Fe concentrations are not reported for this expedition.

Fluid organic geochemistry

Routine analysis of hydrocarbon gas in sediment cores is a part of standard IODP shipboard monitoring to ensure that the sediments being drilled do not contain greater than the expected amount of hydrocarbons that is safe to operate with. The most common method of hydrocarbon monitoring used during IODP expeditions is the analysis of gas samples obtained from either sediment samples (headspace analysis) or from gas expansion pockets visible through clear plastic core liners (void gas analysis), following the procedures described by Kvenvolden and McDonald (1986).

When gas pockets were detected, free gas was drawn from the sediment void using a syringe attached to a hollow stainless steel tool used to puncture the core liner. For headspace analyses, a 3 cm^3 bulk sediment sample was collected from the freshly exposed top end of a core section and next to the interstitial water sample immediately after core retrieval using a brass boring tool or plastic syringe. The sediment plug was sealed with an aluminum crimp cap with teflon/silicon septa. The vial was then heated to 70°C for ~30 min to evolve hydrocarbon gases from the sediment plug. When consolidated or lithified samples were encountered, chips of material were placed in the vial and sealed. For gas chromatographic analysis, a 5 cm^3 volume of headspace gas was extracted from the sealed sample vial using a standard gas syringe and analyzed by gas chromatography.

The standard safety gas analysis program was complemented with additional headspace samples taken at the same resolution described above, to measure the stable carbon and hydrogen isotope composition of hydrocarbons at onshore laboratories. The sampling method was the same as that used for the safety analysis, except that the sediment plug was extruded into a 20 cm^3 headspace glass vial filled with 10 cm^3 of a 1 M potassium chloride (KCl) solution containing borosilicate glass beads and immediately sealed with an aluminum crimp cap with teflon/silicon septa. These vials had been flushed with helium and capped within 1 h prior to sampling, in order to remove air from the headspace and ensure the sample was preserved anaerobically. After the sample was sealed in the vial, it was vigorously shaken to help dissociate the sediment. Potassium chloride is toxic and was thus used to stop all microbial activity in the sediment. The glass beads (3 mm in diameter) were used to help break up the sediment plug during shaking and liberate gas trapped in sediment pore space or adsorbed on particles.

Headspace samples were directly injected into the gas chromatograph fitted with a flame ionization detector (GC3-FID) or the natural gas analyzer (NGA). The Agilent/HP 6890 Series II gas chromatograph (GC3) is equipped with 8 ft, 2.00 mm inner diameter (ID) × ⅛ inch outer diameter stainless steel column packed with 80/100 mesh HayeSep R (Restek) and an FID set at 250°C. The GC3 oven temperature was programmed to hold for 8.25 min at 80°C, ramp at 40°C/min to 150°C, hold for 5 min, and return to 100°C postrun, for a total of 15 min. Helium was used as the carrier gas. The GC3 system determines concentrations of methane (C_1), ethane (C_2), ethene ($C_{2=}$), propane (C_3), and propene ($C_{3=}$). For hydrocarbon analysis, the NGA is outfitted with an Agilent/HP 6890 Series II GC equipped with an Agilent DB-1 dimethylpolysiloxane capillary column (60 m × 0.320 mm diameter × 1.50 µm film thickness) fitted with an FID and using He as carrier gas (constant flow of 21 mL/min). The NGA oven temperature was programmed to hold for 2 min at 50°C, ramp at 8°C/min to 70°C, and then ramp at 25°C/min to 200°C, with a final holding time of 5.1 min. The FID

temperature was 250°C. For nonhydrocarbon gases, thermal conductivity detector separation used three columns: a 6 ft × 2.0 mm ID stainless steel column (Poropak T; 50/80 mesh), a 3 ft × 2.0 mm ID stainless steel molecular sieve column (13X; 60/80 mesh), and a 2.4 m × 3.2 mm ID stainless steel column packed with 80/100 mesh HayeSep R.

Data were collected using the Hewlett Packard 3365 Chemstation data processing program. Chromatographic response is calibrated to nine different gas standards with variable quantities of low molecular weight hydrocarbons (N_2, O_2, CO_2, Ar, and He) and checked on a daily basis. Gas concentrations for the required safety analyses are expressed as component parts per million by volume (ppmv) relative to the analyzed gas. The internal volumes of 15 representative headspace vials were carefully measured and determined to average 21.5 ± 0.18 mL. This volume was taken as a constant in calculations of gas concentrations.

Void gas samples were analyzed on shore using gas chromatography with flame ionization (GC3-FID) and thermal conductivity (GC-TCD) detectors. For hydrocarbon analysis, an Agilent 7890A was equipped with a DB-1 dimethylpolysiloxane capillary column (50 m × 0.320 mm diameter × 5 µm film thickness) fitted with a FID and using helium as carrier gas (constant flow of 1.8 mL/min). The GC oven temperature was programmed to hold for 3 min at 30°C, ramp at 20°C/min to 100°C, and then ramp at 25°C/min to 195°C with a final holding time of 5 min. For detection of hydrocarbons, the FID temperature was 250°C. For nonhydrocarbon gases, the GC was outfitted with a 6 ft × 2.0 mm ID stainless steel column, packed with 80 × 100 mesh carbosphere, and a TCD.

The concentrations of C_1–C_6 hydrocarbons gases were calibrated using five different gas standards and the gas concentrations are expressed as parts per million by volume relative to the analyzed gas. Typical precision, assessed using 10 replicate analyses of a standard, was 1.5% for hydrocarbon.

Sediment geochemistry

For shipboard sediment geochemistry, 5 cm^3 of sediment was freeze-dried for ~24 h, crushed to a fine powder using a pestle and agate mortar, and sampled to analyze inorganic carbon (IC), total carbon (TC), and total nitrogen (TN).

Elemental analysis

The TC and TN of the sediment samples were determined with a ThermoElectron Corporation FlashEA 1112 CHNS elemental analyzer equipped with a ThermoElectron packed column CHNS/NCS and a thermal conductivity detector. Approximately 10–15 mg of freeze-dried, ground sediment was weighed into a tin cup, and the sample was combusted at 900°C in a stream of oxygen. The reaction gases were passed through a reduction chamber to reduce nitrogen oxides to nitrogen and were then separated by the gas chromatograph before detection by thermal conductivity detector. All measurements were calibrated to a standard soil reference material (soil standard 33840025) for carbon and nitrogen detection (Thermo), which was run every six samples for verification. The detection limit was 0.001% for TN (instrument limit) and 0.002% for TC (procedural blank, measured as an empty tin cup). Repeated (n = 21) analyses of the standards yielded precisions of TN < 3% and TC < 5%.

Inorganic and organic carbon content

Total inorganic carbon (TIC) concentrations were determined using a UIC 5011 CO2 coulometer. Between 10 and 12 mg of freeze-dried, ground sediment was weighed and reacted with 2 N HCl. The liberated CO_2 was titrated, and the end point was determined by a photodetector. Calcium carbonate ($CaCO_3$) content, expressed as weight percent, was calculated from the TIC content, assuming that all evolved CO_2 was derived from the dissolution of $CaCO_3$ by the following equation:

$$CaCO_3\ (wt\%) = TIC \times 8.33\ (wt\%).$$

No correction was made for the presence of other carbonate minerals. Accuracy during individual batches of analyses was determined by running a carbonate standard (100 wt% $CaCO_3$) every 10 samples. Typical precision assessed using 36 replicate analyses of a carbonate sample was 1%. The detection limit for $CaCO_3$, defined here as three times the standard deviation of the blank (2 N HCl), was 0.1% for 100 mg of pelagic clay. Total organic carbon (TOC) content was calculated as the difference between TC (measured on the elemental analyzer) and IC (measured by coulometry):

$$TOC = TC - IC.$$

Physical properties

Physical properties measurements provide fundamental information required to characterize lithostratigraphic units, basement properties, and hydrogeology and allow for the correlation of cored materials with logging data. A comprehensive discussion of methodologies and calculations used in the *JOIDES Resolution*

Physical Properties Laboratory is presented in Blum (1997). Two additional measurement types and one additional measurement tool not described in Blum (1997) were used during this expedition. These consisted of electrical conductivity, which provides information relevant to chemical diffusion, and anelastic strain recovery, which provides information on stress orientation. A needle penetrometer, which covers a higher range of compressive strength than the standard pocket penetrometer, was used for indurated sediments.

Recovered whole-round cores were first allowed to thermally equilibrate to an ambient room temperature of ~20°C (~3 h). After thermally equilibrating, core sections longer than 30 cm were run through the WRMSL for measurement of gamma ray attenuation (GRA) density, magnetic susceptibility, and compressional wave velocity (*P*-wave Logger [PWL]). Sections longer than 50 cm were measured with the spectral NGRL.

For cores with soft sediments, thermal conductivity measurements were carried out on whole-round core sections using the needle probe technique. For lithified sediments, thermal conductivity was measured on split cores using the half-space technique.

After the cores were split into archive and working halves, digital image scanning was carried out on the cut surfaces of archive core halves using the SHIL. Following the SHIL, the archive half of the core was passed through the SHMSL for measurement of point magnetic susceptibility and color spectrophotometry. The SHMSL uses a laser to record relief along the core, which yields information about the location of gaps and cracks between core pieces.

Discrete samples for moisture and density (MAD) measurements were taken from the working half at a frequency of approximately one per section. MAD measurements yield wet bulk density, dry bulk density, grain density, water content, void ratio, and porosity.

P-wave velocity was measured on the working half of cores. Electrical conductivity was measured at a frequency of approximately one per section and was used to estimate formation factor. Shear strength was measured using the automated vane shear (AVS) apparatus, and compressive strength was measured using pocket and needle penetrometers.

Whole-Round Multisensor Logger measurements

GRA bulk density, *P*-wave velocity, and magnetic susceptibility were measured nondestructively with the WRMSL. To optimize WRMSL performance, sampling intervals and measurement integration times were the same for all sensors. The sampling interval was set at either 1 or 2.5 cm (depending on available time) with an integration time of 5 s for each measurement. GRA performance was monitored by passing a single core liner filled with deionized water through the WRMSL after every core.

In general, measurements are most effective with a completely filled core liner with minimal drilling disturbance. For APC sediment cores, the 66 mm core liner width is generally filled. Cores recovered using the XCB and RCB have a diameter smaller than the core liner. Because the reported bulk density values assume a 66 mm diameter, GRA bulk density measurements from XCB and RCB cores tend to underestimate true values. Sections consisting of discontinuous fragments were not measured with the WRMSL sensors.

Gamma ray attenuation bulk density

The GRA densiometer on the WRMSL operates by passing gamma rays from a ^{137}Cs source through a whole-round core into a 75 mm × 75 mm sodium iodide detector situated directly above the core. The gamma ray peak has a principal energy of 0.662 MeV and is attenuated as it passes through the core (Evans, 1965; Harms and Choquette, 1965). The attenuation of gamma rays, mainly by Compton scattering, is related to the material bulk density and thickness of the sample. The gamma ray count is proportional to density. Bulk density, ρ, determined with this method can be expressed as

$$\rho = 1/(\mu d) \times \ln (I_0/I),$$

where

- μ = Compton attenuation coefficient,
- d = sample diameter,
- I_0 = gamma ray source intensity, and
- I = measured intensity of gamma rays passing through the sample.

The attenuation coefficient and gamma ray source intensity are treated as constants, such that ρ can be calculated from *I*. The gamma ray detector is calibrated with a set of aligned aluminum cylinders of various diameters surrounded by distilled water in a sealed core liner that is the same as that used during coring operations. The relationship between *I* and the product of μ and *d* can be expressed as

$$\ln I = A(\mu d)^2 + B(\mu d) + C,$$

where *A*, *B*, and *C* are coefficients determined during calibration. Gamma ray counts through each cylinder were determined for a period of 60 s, and the natural log of resulting intensities was plotted as a function of μ*d*. Here density of each aluminum

cylinder was 2.7 g/cm^3 and d was 1, 2, 3, 4, 5, or 6 cm. The WRMSL provided the values of I and μ, and ρ was calculated with the above equation. Recalibration was performed as needed if the deionized water standard after every core deviated significantly (more than a few percent) from 1 g/cm^3. The spatial resolution of the GRA densiometer is <1 cm.

Magnetic susceptibility

Magnetic susceptibility, k, is a dimensionless measure of the degree to which a material can be magnetized by an external magnetic field:

$$k = M/H,$$

where M is the magnetization induced in the material by an external field strength H. Magnetic susceptibility responds to variations in the magnetic composition of the sediment that commonly can be related to mineralogical composition (e.g., terrigenous versus biogenic materials) and diagenetic overprinting. Materials such as clay generally have a magnetic susceptibility several orders of magnitude lower than magnetite and some other iron oxides that are common constituents of igneous material. Water and plastics (core liner) have a slightly negative magnetic susceptibility.

The WRMSL incorporates a Bartington Instruments MS2 meter coupled to a MS2C sensor coil with an 88 mm diameter and operates at a frequency of 565 Hz. The sensor output was set to record in instrument units. Data shown here and within the database are not corrected for volume effects due to differing APC, XCB, and RCB core diameters or varying sample bulk densities. The instrument is calibrated with a homogeneous mixture of magnetite and epoxy in a 40 cm long piece of core liner to an accuracy of ±5%. The spatial resolution of the method is ±4 cm; therefore, core material that is not continuous over an 8 cm interval will underestimate the magnetic susceptibility.

Compressional wave velocity

The compressional wave velocity sensor measures the ultrasonic *P*-wave velocity of the whole-round sample residing in the core liner. The PWL transmits a 500 kHz *P*-wave pulse across the core section at a specified repetition rate. This signal is coupled to the sample by the plastic pole contacts of the transducers clamped to the sides of the core by the linear actuator. Frequently, water is used to improve coupling between the transducers and the liner. The plastic pole contacts and the pressure applied by the actuator are generally sufficient for reliable *P*-wave velocity measurement. The transmitting and receiving ultrasonic transducers are aligned so that wave propagation is perpendicular to the long axis of the core section. Torque applied by the actuator can be set by the user to ensure good acoustic contact between the liner and the core material. Because of poor contact between the core liner and XCB and RCB cores, WRMSL *P*-wave velocity was generally not measured on those cores.

The basic relationship for sonic velocity, V, is

$$V = d/t,$$

where d is the path length of the wave through the core and t is the traveltime. Besides the traveltime through the sample, the total traveltime between the transducers includes three additional components:

t_{delay} = time delay related to transducer faces and electronic circuitry),
t_{pulse} = delay related to the peak detection procedure), and
t_{liner} = transit time through the core liner).

The system is calibrated using a core liner filled with deionized water. For routine measurement on whole-round cores inside core liners, the corrected core velocity, V_{core}, can be expressed by

$$V_{core} = (d'_{core} - 2d_{liner})/(t_0 - t_{pulse} - t_{delay} - 2t_{liner}),$$

where

d'_{core} = measured diameter of core and liner,
d_{liner} = liner wall thickness, and
t_0 = measured total traveltime.

Traveltime is determined by signal processing software that automatically detects the first arrival of the *P*-wave signal to a precision of 50 ms. It is a challenge for an automated routine to pick the first arrival of a potentially weak signal if background noise is high. The search method skips the first positive amplitude and finds the second positive amplitude using a detection threshold limit, typically set to 30% of the maximum amplitude of the signal. The program then finds the preceding zero crossing and subtracts one wave period to determine the first arrival. To avoid extremely weak signals, a minimum signal strength can be set (typically 0.02 V) and weaker signals are ignored. To avoid signal interference at the beginning of the record from the receiver, a delay (typically 0.01 ms) can be set to force the amplitude search to begin in the quiet interval preceding the first arrival. In addition, a trigger (typically 4 V) is selected to initiate the arrival search process, and the number of waveforms to be stacked (typically five) can also be set. A linear voltage differential transformer measures the separation of the transducer to derive a signal path length (i.e., the core

diameter). After corrections for system propagation delay, liner thickness, and liner material velocity, the ultrasonic *P*-wave velocity is calculated.

Natural Gamma Radiation Logger measurements

The NGRL measures gamma radiation emitted from whole-round core sections arising primarily from the decay of ^{238}U, ^{232}Th, and ^{40}K isotopes. The main NGR detector unit consists of 8 sodium iodide (NaI) scintillator detectors, 7 plastic scintillator detectors, 22 photomultipliers, and passive lead shielding. The NaI detectors are covered by 8 cm of lead shielding. In addition, lead separators (~7 cm of low-background lead) are positioned between the NaI detectors. Half of the lead shielding closest to the NaI detectors is composed of low-background lead, whereas the outer half is composed of regular (virgin) lead. In addition to passive lead shielding, the NGRL employs a plastic scintillator to suppress the high-energy gamma and muon components of cosmic radiation by producing a canceling signal when these charged particles pass through the plastic scintillators. The NGRL was calibrated using a source consisting of ^{137}Cs and ^{60}Co and identifying the peaks at 662 keV (^{137}Cs) and 1330 keV (^{60}Co). Calibration materials are provided by Eckert & Ziegler Isotope Products, Valencia, California (USA).

For presentation purposes, the counts were summed over the range of 100–3000 keV. Background measurements of an empty core liner counted for 20,000 s (5 h) were made upon arrival at each site. Over the 100–3000 keV integration range, background counts averaged 4–5 cps.

A measurement run consisted of eight simultaneous measurements offset by 20 cm each. The quality of the energy spectrum measured in a core depends on the concentration of radionuclides in the sample but also on the counting time, with higher times yielding better spectra. The available count time in each position depended on core flow. For sediment cores, counting times were generally 10 min. For basement cores, counting times were extended as allowed by available time.

Section Half Multisensor Logger measurements

The SHMSL measures magnetic susceptibility and spectral reflectance on core section halves. The archive half of the split core is placed on the system's core track. An electronic platform moves along a track above the core section, recording the sample height with a laser sensor. The laser establishes the location of the bottom of the section, and the platform reverses the direction of movement, moving from bottom to top making measurements of point magnetic susceptibility and spectral reflectance data at 2.5 cm intervals.

Color reflectance spectrometry

Reflectance is measured from 171 to 1100 nm wavelength at 2 nm intervals using a halogen light source, covering a wavelength from ultraviolet through visible to near-infrared. The scan of the entire wavelength range takes ~5 s per data acquisition offset. The data are generated using the L*a*b* color system, in which L* is luminescence, a* is the blue + green value, and b* is the red + green value. The color reflectance spectrometer calibrates on two spectra, pure white (reference) and pure black (dark). Color calibration was conducted approximately every 12 h.

Point magnetic susceptibility

Point magnetic susceptibility is measured using a contact probe with a flat, 15 mm diameter sensor operating at a frequency of 0.580 kHz. The sensor takes and averages three measurements at 0.1 attenuation for each offset to an accuracy of 5%. The spatial resolution of the magnetic susceptibility point instrument is 2 cm, making it advantageous over whole-round magnetic susceptibility measurements for basement cores consisting of broken pieces <8 cm long (the spatial resolution of whole-round magnetic susceptibility). Results are reported in dimensionless instrument units. The point magnetic susceptibility meter was calibrated by the manufacturer before installation on the ship. The probe is zeroed in air before each measurement point, and a background magnetic field is measured (influence from metal track, etc.) and removed from the measured value before data are recorded.

Thermal conductivity

Thermal conductivity is a measure of the ease at which heat flows through a material and is dependent on composition, porosity, and structure. Thermal conductivity was measured on unconsolidated sediment and rock samples using the full-space needle probe (Von Herzen and Maxwell, 1959) and the half-space line source (Vacquier, 1985), respectively. Both the full- and half-space methods approximate the heating element of an infinite line source (Blum, 1997). These measurements produce a scalar value in a plane perpendicular to the orientation of the probe. All measurements were made after the cores had equilibrated to ambient laboratory temperature. After the background thermal drift was determined to be stable, the heater circuit was closed and the increase in the probe temperature was recorded.

In porous rocks, temperature influences thermal conductivity in two competing ways. The thermal conductivity of rock matrix is inversely related to temperature (Zoth and Haenel, 1988), whereas the thermal conductivity of water increases with temperature (Keenan et al., 1978). Reported thermal conductivity values are at laboratory temperatures and have not been corrected to in situ temperature. Previous studies suggest a correction of +5% for each +20°C change in temperature between the laboratory and in situ conditions for a high-porosity, water-saturated sediment (Ratcliffe, 1960) and –3% for several hard rocks (Clark, 1966).

For soft sediment, a full-space single-needle probe TeKa TK04 unit (Blum, 1997) was utilized to measure thermal conductivity of whole cores. To insert this probe, a hole was made in the core liner at a position based on visual inspection of the core to avoid disturbed regions. A rubber insulator was sometimes wrapped around the core and the lower portion of the probe before placing the section in a box to reduce ambient temperature variations and speed up temperature drift calibration times. Temperature-time series were acquired over ~80 s. Values of thermal conductivity are based on the observed rise in temperature for a given quantity of heat. In most cases, repeated measurements were made at the same location, and in these cases the probe was left in place and the sample was left to re-equilibrate for 5 to 10 min prior to the next measurement.

Thermal conductivity on lithified samples was measured on the working half of the split core with the thermal conductivity meter in half-space mode (Vacquier, 1985). Samples must be smooth and flat to ensure adequate contact with the heating needle. Visible saw marks were removed when necessary by grinding the split surface with 120–320 gauge silicon carbide powder.

Moisture and density

Several basic quantities of interest (water content, bulk density, dry density, porosity, and void ratio) are found most accurately through mass and volume determinations on discrete samples. The shipboard MAD facility on the *JOIDES Resolution* includes a dual-balance system and a pycnometer with six cells. Sediment samples were measured in vials, and the mass and volume of the vials were subtracted to determine sediment mass and dry volume.

Immediately after sediment samples were collected, the vials were capped until weighing to prevent moisture loss. As soon as possible after collection, the wet sediment mass (M_{wet}) was measured. Dry sediment mass (M_{dry}) and volume (V_{dry}) were measured after drying the samples in a convection oven for >24 h at a temperature of 105° ± 5°C and then cooling in a desiccator for >1 h. The dual-balance system was used to measure both wet and dry masses. Two Mettler-Toledo XS204 balances were used to compensate for ship motion, one acting as a reference and the other for measurement of the unknown. A standard weight of similar value to the sample was placed upon the reference balance to increase accuracy. The default setting of the balances is 300 measurements (taking ~1.5 min).

Dry volume was measured using a helium-displacement pycnometer with a nominal precision of ±0.04 cm^3. The pycnometer system measures dry sample volume using six pressurized, helium-filled chambers. At the start of the expedition, and whenever the helium gas tank was changed, shipboard technicians performed a calibration using stainless steel spheres of known volume. Each pycnometer chamber was tested at least once a day by running spheres of known volume. Spheres are assumed to be known to be within 1% of their total volume. Individual volume measurements were preceded by three purges of the sample chambers with research grade (99.995% or better) helium heated to 28°C followed by three data acquisition cycles. Each reported value consists of an average of the three measurements.

For calculation of sediment bulk density, dry density, grain density, porosity, and void ratio, the traditional ODP method was used (Method C; Blum, 1997). Water content, porosity, and void ratio are defined by the mass or volume of extracted water before and after removal of interstitial pore water through the drying process. Standard seawater density (1.024 g/cm^3) is used for the density of pore water.

Water content (W_c) was determined following the methods of the American Society for Testing and Materials (ASTM) designation D2216 (ASTM International, 1990). Corrections are required for salt when measuring the water content of marine samples. In addition to the recommended water content calculation in ASTM D2216 (i.e., the ratio of pore-fluid mass to dry sediment mass [% dry wt]), we also calculated the ratio of pore-fluid mass to total sample mass (% wet wt). The equations for water content are

$$W_c\ (\%\ \text{dry wt}) = (M_t - M_d)/(M_d - rM_t)$$

and

$$W_c\ (\%\ \text{wet wt}) = (M_t - M_d) \times (1 + r)/M_t,$$

where

M_t = total mass of the saturated sample,
M_d = mass of the dried sample, and
r = salinity.

Bulk density, ρ, is the density of the saturated samples, with $\rho = M_t/V_t$. The mass, M_t, was measured using the balance, and V_t was determined from the pycnometer measurements of grain volume and the calculated volume of the pore fluid ($V_t = V_{pore} + V_d$).

Porosity, ϕ, was calculated using

$$\phi = (W_c \times \rho)/[(1 + W_c) \times \rho_w],$$

where

- ρ = calculated bulk density,
- ρ_w = density of the pore fluid, and
- W_c = water content expressed as a decimal ratio of percent dry weight.

Grain density, ρ_{grain}, was determined from measurements of dry mass and dry volume made in the balance and in the pycnometer, respectively. Mass and volume were corrected for salt using

$$\rho_{grain} = (M_d - s)/[V_d - (s/\rho_{salt})],$$

where s is the salt content (in grams) and ρ_{salt} is the density of salt (2.257 g/cm^3).

Compressional wave velocity

Discrete compressional wave velocity measurements were obtained on sediment cores at a frequency of 1 per section where conditions allowed. *X*-axis measurements were acquired with a caliper-type contact probe with one plastic transducer contact on the face of the working half of the core and the other contact against the core liner. *Y*- and *z*-axis measurements were acquired using two pairs of bayonet probes inserted perpendicular and parallel to the face of the working half, respectively.

For indurated sediments, *P*-wave velocities were measured on the split core using the *x*-axis caliper-type contact probe transducers on the *P*-wave velocity gantry. The system uses Panametrics-NDT Microscan delay line transducers, which transmit at 500k Hz. To maximize contact with the transducers, deionized water was applied to sample surfaces.

The signal received through the sample was recorded by the computer attached to the system, and the peak of the initial arrival was chosen either with autopicking software or by manual picking based on operator evaluation. The complete waveform is stored with the data in case reanalysis is deemed necessary. The distance between transducers was measured with a built-in linear voltage displacement transformer (LDVT).

Calibration was performed each day before measurements were made with a series of acrylic cylinders of differing thicknesses and known *P*-wave velocity of 2750 ± 20 m/s for the caliper-type contact probe and water for the bayonet probes. The determined system time delay from calibration was subtracted from the picked arrival time to yield a traveltime of the *P*-wave through the sample. The thickness of the sample (calculated by LDVT in meters) was divided by the traveltime (in seconds) to calculate a *P*-wave velocity in meters per second.

Downhole temperature measurements

Downhole temperature measurements were made using the advanced piston coring temperature tool (APCT-3). The APCT-3 consists of three components: electronics, coring hardware, and computer software. The temperature sensors were calibrated for a working range of 0° to 45°C. Prior to entering a hole, each instrument is held at the mudline for ~10 min to equilibrate with bottom water temperature. After bottom water temperature equilibration, the tools are lowered in the hole to penetrate the formation. The penetration of each tool into the formation generates a rise in temperature caused by frictional heating. Following the initial temperature rise, temperatures decrease along a decay curve to near equilibrium. During this decay phase, it is important that the temperature tool is not disturbed. A second rise in temperature occurs because of frictional heating as the tool is pulled out of the formation. Temperatures were measured as a time series with a sampling rate of 1 s and logged onto a microprocessor within the downhole tool. The data were retrieved when the tool was recovered. The formation equilibrium temperature was determined based on fitting the temperature decay curve using the MATLAB TP-Fit program (M. Heeseman et al., pers. comm., 2008).

If heat transfer is conductive and constant with depth through the sediment, the thermal gradient will be inversely proportional to thermal conductivity according to Fourier's law. This relationship can be linearized by plotting temperature as a function of summed thermal resistance (Bullard, 1939):

$$T(z) = T_o + Q\sum_{i=1}^{N}\left(\frac{\Delta z_i}{k(z)_i}\right)$$

$$T(z) = T_o\sum_{i=1}^{N}\left(\frac{\Delta z_i}{k(z)_i}\right),\ i = 1;n$$

where

- T = temperature,
- z = depth,
- T_0 = bottom water temperature,
- Q = heat flow, and
- $\sum_{i=1}^{N}\left(\frac{\Delta z_i}{k(z)_i}\right)$ = thermal resistance.

Where thermal conductivity data were available throughout the borehole, the above equation was used to estimate the borehole temperature profile.

Shear and compressive strength

Undrained sediment strength was measured using the AVS, a pocket penetrometer, and a needle penetrometer. Measurements were not performed at in situ stress conditions and thereby underestimate the true undrained peak shear strength in situ. Measurements were made with the vane rotation axis and penetrometer penetration direction perpendicular to the split surface.

Undrained shear strength (τ_{fu}) was measured in fine-grained plastic sediment using the AVS system following the procedures of Boyce (1977). The vane rotation rate was set to 90°/min. Peak undrained shear strength was measured typically once per >100 cm section. The instrument measures the torque and strain at the vane shaft using a torque transducer and potentiometer. To minimize disturbance effects resulting from the measurement itself, vane shear tests were generally conducted first, followed by penetrometer tests. Vane shear strength, $S_{u(v)}$ (kPa), is calculated as

$$S_{u(v)} = T/K_v,$$

where T is the torque required to cause the material to fail (N·m) and K_v is the constant depending on vane dimensions (cubic meters) (Blum, 1997).

All AVS measurements reported were obtained using a vane with a height and diameter of 12.7 mm. Failure torque was determined by measuring the degrees of rotation of one of four torsional springs and a manufacturer-specified linear calibration equation relating the rotation angle to torque for the particular spring being used. Selection of the appropriate spring was based on the anticipated shear strength of the material. Vane shear results were generally considered reliable for shear strength values less than ~150–200 kPa, above which excessive cracking and separation of the core material occurred.

Two penetrometers were used to measure compressive strength. A pocket penetrometer was used for soft sediment, and a needle penetrometer was used for lithified sediment. Penetration measurements were all conducted on the split core face. The Geotester STCL-5 pocket penetrometer is a spring-operated device used to measure compressive strength by pushing a 0.25 inch (6.4 mm) diameter probe 0.25 inches (6.4 mm) deep (to the red marker) below the split-core surface. The mechanical scale of compressive strength is in units of kilograms per square centimeter, which are converted into units of kilopascals for reporting as follows:

$$\Delta\sigma_f(\text{kPa}) = 98.1 \times \Delta\sigma_f\ (\text{kg/cm}^2).$$

A 1 inch diameter adaptor foot is available for measuring in very soft sediment. This provides a 16 times increase in area. In addition, for sediment strength in the middle range between the two adaptors, another adaptor foot 0.478 inches (12.14 mm) in diameter was made during the expedition. When the 1 inch diameter foot is used, the scale readings are multiplied by 0.0625, and when the 0.478 inch diameter foot is used, they are multiplied by 0.228484. In the database, the adaptor feet are designated "A" (1 inch diameter adaptor foot), "M" (0.478 inch diameter medium adaptor foot), or "Non" (no adaptor foot). The maximum compressive strength that can be measured with the pocket penetrometer is 220 kPa.

In the case of indurated sediment, a third-party needle penetrometer (SH-70, MARUTO Testing Machine Company, Japan) that covers a much higher range than the pocket penetrometer (>220 kPa) was used. For the needle penetrometer, the equation to estimate a uniaxial compressive strength, $\Delta\sigma_f$, is

$$\Delta\sigma_f(\text{kPa}) = 409.3 \times \text{NP}^{0.978}$$

or

$$\log(\Delta\sigma_f) = 0.978 \times \log(\text{NP}) + 2.621,$$

where NP is the penetration force (N) divided by penetration depth into sediment (mm). The minimum and maximum NP that can be measured are 1 and 100 N/mm, respectively, which is equivalent to 410 and 37,000 kPa of compressive strength, respectively. Measurements using one of the two penetrometers were typically performed once per section, with a higher frequency from 0 to 3 mbsf.

Electrical conductivity and formation factor

Formation factor was determined from electrical conductivity measurements taken adjacent to every MAD measurement on split sediment cores using a third-party tool (University of Rhode Island, USA). Formation factor is used to estimate pore space tortuosity and may be used to quantify chemical diffusivities. For these measurements, two in-line electrodes, 1.5 cm long, spaced 1 cm apart in a block of nonconducting flouoropolymer and attached to a Metrohm 712 conductometer, were inserted into the split-core sediment in the direction of y and z.

At each sampling location, measurements of sediment conductivity, χ_{sed} (the inverse of resistivity,

R_{core}), and sediment temperature were made. Measurements of IAPSO seawater conductivity, χ_{IAPSO}, and temperature were made at the beginning and end of each site. Measurement of a seawater standard conductivity, χ_{sw}, and its temperature were made before and after each core for use in tracking instrument drift. The seawater standard was obtained by pumping seawater from ~4 m below the sea surface at Site U1381 for measurements at Sites U1381 and U1380 and from Site U1412 for Sites U1412–U1414.

Both seawater and sediment measurements of electrical conductivity were adjusted to a standard temperature of 20°C, where the correction factor is given by a fifth-order polynomial (Janz and Singer, 1975):

$$\chi = a + bT + cT^2 + dT^3 + eT^4 + fT^5,$$

where

a = 29.05128,
b = 0.88082,
c = -1.98312×10^{-4},
d = 3.3363×10^{-4},
e = -1.0776×10^{-5}, and
f = 1.12518×10^{-7}.

The temperature corrected measurement, σ_T, is given by

$$\sigma_T = \sigma \times (\chi_{20}/\chi_{obs}),$$

where σ is the measurement and χ_{20} and χ_{obs} are the correction factors using 20°C and the observed temperature, respectively. Both seawater and sediment measurements of electrical conductivity are adjusted for the effects of temperature. A linear drift correction based on the seawater standard measurements is computed and applied to the sediment temperature-adjusted measurements. The formation factor, *F*, is computed as

$$F = [(\alpha \times S_{pw} + \beta)/(\alpha \times S_{IAPSO} + \beta)] \times (\chi_{IAPSO}/\chi_{sed}),$$

where

S_{pw} = measured salinity of the pore water,
S_{IAPSO} = salinity of the IAPSO standard (34.995),
α = 1.169, and
β = 5.196.

The values of α and β were determined by a least-squares fit to measured values of salinity and conductivity of 100%, 80%, 66.7%, and 50% seawater, which spans the range of salinities that were expected at the sites being cored as part of Expedition 344. This simple method for determining formation factor does not account for surface conductivity effects of the sediment matrix.

Anelastic strain recovery analysis

The anelastic strain recovery (ASR) technique is a core-based stress measurement that can evaluate both the orientation and magnitude of the 3-D principal stress tensor. The ASR technique is principally used to measure the anelastic strain change due to releasing the stress soon after core recovery. ASR measurements during Expedition 344 followed the methodology of Matsuki (1991), with guidelines described in Lin et al. (2007), and were made using a third-party instrument (JAMSTEC, Japan).

Soon after a 15 cm long fresh whole-round core was taken on the catwalk, WRMSL measurements were carried out. Because ASR measurements are very time sensitive, WRMSL measurements were conducted prior to thermal equilibration. The core samples were extruded from core liners, the outer surface was washed in seawater to remove drilling mud, and the surfaces were air-dried at room temperature and marked with reference lines at 45° intervals to ensure that strains were measured in at least nine directions, six of which were independent (18 wire strain gauges: 6 cross gauges and 6 single gages). It took 1–2 h to insert all strain gauges, and the total elapsed time after core on deck was 1–2 h before we started recording the strain (core diameter) changes.

To prevent volumetric changes associated with pore fluid evaporation and temperature change, the core samples were triple bagged (i.e., with two plastic bags and an aluminum bag) and submerged in a thermostatic chamber where temperature changes were kept controlled within less than ±0.1°C from the room temperature (23°C) during measurement. All strain data were collected every 10 min for a maximum of 14 days. ASR results were not available shipboard during Expedition 344, so are not included in the site reports. Data are available from IODP by request.

Paleomagnetism

Shipboard paleomagnetism was investigated mainly to determine directions of remanence components. Routine measurements were conducted on archive section halves with stepwise alternating field (AF) demagnetization. Discrete cube and minicore samples were taken from selected working-half sections and measured with stepwise AF and thermal demagnetization. These data were used for core orientation and magnetostratigraphic dating.

Magnetic measurements

Remanent magnetization was measured using a 2G superconducting rock magnetometer (SRM; 2G Enterprises model 760R) equipped with direct-current

superconducting quantum interference devices (SQUIDs) and an in-line, automated AF demagnetizer capable of reaching a peak field of 80 mT. Ocean drilling cores generally carry secondary overprint remanence components. Common overprints for ocean drilling cores include natural viscous remanence and a steep downward-pointing component attributed to the drill string. To separate overprints from the characteristic remanence (ChRM), stepwise demagnetization was performed, as described below.

Archive-half sections

Measurements of archive halves were conducted using the SRM for Section software (version 1.0; 8/15/2011) with a nominal sample area parameter of 15.59 cm^2. The interval between measurement points and measurement speed were selected as 2.5 cm and 10 cm/s, respectively.

We performed successive AF demagnetization using the in-line AF demagnetizer of the SRM (2G Enterprises model 2G600) on all split-core archive sections. The in-line AF demagnetizer applies a field to the *x*-, *y*-, and *z*-axes of the SRM in this fixed order. Previous reports suggest that higher AF demagnetization fields have produced significant anhysteretic remanent magnetization (ARM) along the *z*-axis of the SRM. With this limitation, we used demagnetization steps up to 30 or 40 mT to demagnetize the sections. For most of the sediment sections, we performed 4–7 steps from natural remanent magnetization (NRM) to 30 or 40 mT demagnetization. AF demagnetization results were plotted individually as vector plots (Zijderveld, 1967), as well as downhole variations with depth. We inspected the plots visually to judge whether the remanence after demagnetization at the highest AF step reflects the ChRM and geomagnetic polarity sequence.

Magnetic noise due to anomalous *y*-axis flux jumps

During Expedition 344, especially in Hole U1412A, we observed large *y*-axis flux jumps due to the "antenna" effect described by the Expedition 342 scientists (see "Paleomagnetism" in the "Site U1405" chapter [Expedition 342 Scientists, in press]). We rewrapped the power cable attached to the in-line degausser with aluminum foil and ensured that this foil was electrically connected to the existing shielding material of the SRM. The flux jumps decreased abruptly thereafter, and SRM demagnetization data from Hole U1412B and subsequent sites were remarkably free of the magnetic noise caused by the *y*-axis flux jumps. Moderate to small flux jumps still occurred at Site U1413, possibly associated with rig floor activity. At Site U1414, we observed increased flux jumps for reasons that are unclear at present.

Discrete samples

Oriented discrete samples representative of the lithology were collected from working-half sections. In soft sediment, discrete samples were taken in plastic "Japanese" Natsuhara-Giken sampling cubes (7 cm^3 sample volume; Fig. **F15**). Cubes were pushed into the working half of the core by hand with the "up" arrow on the cube pointing upsection in the core. For indurated intervals, cubes were cut with a table saw and trimmed to fit into the plastic containers. In lithified sediments and hard rocks, minicores (~11 cm^3) were taken. Measurements of discrete samples were conducted using the SRM for Discrete software (version 1.0, 8/15/2011).

For discrete samples, we performed successive AF demagnetization with the DTech AF demagnetizer (model D-2000) for the spinner magnetometer measurements to 120 mT (majority of samples) and 200 mT (for several high-coercivity samples). We also performed successive thermal demagnetization using a thermal specimen demagnetizer (ASC Scientific model TD-48SC) for several selected discrete samples up to 675°C. Temperature increments of 25°–100°C were used, depending on the unblocking temperature of each sample. We analyzed the stepwise demagnetization data of the discrete samples by principal component analysis (PCA) to define the ChRM (Kirschvink, 1980). Section half and discrete data collected on the pass-through SRM were uploaded to the LIMS.

Anisotropy of magnetic susceptibility (AMS) measurements were made on an AGICO KLY 4S Kappabridge instrument using the AMSSpin LabVIEW program designed by Gee et al. (2008) and adapted for use with the shipboard KLY 4S. The KLY 4S Kappabridge measures AMS by rotating the sample along three axes, stacking the data, and calculating the best-fit second-order tensor. It also measures volume-normalized, calibrated bulk susceptibility (χ).

Coordinates

All magnetic data are reported relative to the IODP orientation conventions: +*x* is into the face of the working half, +*y* points toward the left side of the face of the working half, and +*z* points downsection. The relationship of the SRM coordinates (*x*-, *y*-, and *z*-axes) to the data coordinates (*x*-, *y*-, and *z*-directions) is as follows: for archive halves, *x*-direction = *x*-axis, *y*-direction = –*y*-axis, and *z*-direction = *z*-axis; for working halves, *x*-direction = –*x*-axis, *y*-direction = *y*-axis, and *z*-direction = *z*-axis (Fig. **F15**). The coordinate

system for the spinner magnetometer (AGICO model JR-6A) and Natsuhara-Giken sampling cubes are shown in Figure F16.

Core orientation

Core orientation of APC cores was achieved with an orientation tool (FlexIT) mounted on the core barrel. The tool consists of three mutually perpendicular fluxgate magnetic sensors and two perpendicular gravity sensors. The information from both sets of sensors allows the azimuth and dip of the hole to be measured, as well as the azimuth of the APC core orientation. Generally, the orientation tool has an accuracy of 20°–30°. The orientation information contributed to paleomagnetic polarity determinations and magnetostratigraphic interpretations.

The ChRMs also provide a reference frame to orient cores (see "Structural geology"). Provided that the reference magnetic pole is known, the orientation of the paleomagnetic vector is then used to restore the azimuth of the core: the horizontal component of the mean ChRM makes an angle with the reference line, which specifies the rotation of the core relative to the geographic coordinates (e.g., Fuller, 1969). The relatively young expected age (Neogene) of the sediments and nearly longitudinal (westward) slow motion of the Caribbean plate during this period (e.g., Pindell et al., 1988) allow us to approximate the reference magnetic pole by the present-day geographic poles for the entire sedimentary section. The other assumptions for orientation are (1) the section has enough measurements to average out geomagnetic secular variation, (2) the original bedding is horizontal, (3) the core is vertical, and (4) the sedimentary unit has not experienced any vertical axis rotation. Assumptions 2 and 3 were confirmed with shipboard structural geologists, seismic profiles of the drill sites, and drilling operational records. Assumptions 1 and 4 remain to be checked.

For intervals of particular interest for structural geology, we report the ChRMs defined from discrete samples. More detailed demagnetization steps for the discrete samples allowed more accurate ChRMs than those from the archive halves.

Magnetostratigraphy

Magnetostratigraphy for each site was constructed by correlating observed polarity sequences with the geomagnetic polarity timescale (GPTS) in combination with biostratigraphic datums. We adopted the GPTS of Gradstein et al. (2012) (Table T3). In this GPTS, boundary ages for Chrons C1n–C13n and C24n.1n–C34n are orbitally tuned, whereas those for Chrons C13r–C23r are spline fitted.

For azimuthally unoriented samples from sedimentary rocks that formed in low latitudes, determining the polarity of sedimentary units can be difficult. The polarity ambiguity arises when the samples are azimuthally unoriented and the inclination is shallow near the Equator (the angular distance between reversed and normal polarity inclinations is small). Because paleomagnetic inclinations from any samples will have some degree of dispersion about their mean inclination, it is likely that when the mean inclination is shallow, the sign of the inclination will not be indicative of the polarity (e.g., McFadden and Reid, 1982; Cox and Gordon, 1984). The sign of the inclination of these samples should be used carefully as a definitive estimate of magnetic polarity.

Our interpretation is compared with predicted paleolatitudes of the drill sites according to the absolute plate motion of the Cocos plate following MORVEL plate reconstruction (DeMets et al., 2010, 2011). Based on paleomagnetic records reconstructions, our drill sites have moved northward since the formation of these sediments at a velocity of ~90 km/m.y. Following the reconstructed position of the drill holes for two representative periods at 2 and 12 Ma (Fig. F17), the paleolatitudes would be ~2° and ~12° to the south of their present day positions, respectively. However, if our mean inclinations are steeper than expected (according to the model), this could be due to some unresolved combination of unaccounted for plate motion, long-term nondipole fields, or effects of hotspot motion on the plate circuit models (e.g., Barckhausen et al., 2001).

Whenever possible, we offer an interpretation of the magnetic polarity, with the naming convention following that of correlative anomaly numbers prefaced by the letter C (Tauxe et al., 1984). Normal polarity subchrons are referred to by adding suffixes (n1, n2) that increase with age. For the younger part of the timescale (Pliocene–Pleistocene) we use the traditional names to refer to the various chrons and subchrons (e.g., Brunhes, Jaramillo, Olduvai, etc.). In general, polarity reversals occurring at core section ends have been treated with extreme caution.

Downhole logging

Downhole logs measure physical, chemical, and structural properties of the rock formation penetrated by a borehole. The data are collected continuously with depth and measured in situ; they can be interpreted in terms of the stratigraphy, lithology, mineralogy, and geochemical composition of the rock formation. Downhole logs also provide information on the condition, shape, and size of the borehole and on possible deformations induced by

drilling or by the stress field. Where core recovery is incomplete or disturbed, log data may provide the only way to characterize the borehole section. Where core recovery is good, log and core data complement each other and can be interpreted jointly.

The scales of downhole log measurements are intermediate between those obtained from laboratory measurements on core samples and geophysical surveys. Logs are useful in calibrating the interpretation of geophysical survey data (e.g., through the use of synthetic seismograms) and provide a necessary link for the integrated understanding of physical properties on all scales.

Wireline logging

During wireline logging, measurements are made with a variety of Schlumberger and Lamont-Doherty Earth Observatory (LDEO) logging tools combined into several tool strings, which are run into the hole on a wireline cable after coring operations are complete. Two wireline tool strings were used during Expedition 344: a modified triple combination or "triple-combo" (gamma ray, bulk density, resistivity, and ultrasonic imaging of the borehole wall) and the Formation MicroScanner (FMS)-sonic (resistivity imaging of the borehole wall and sonic velocities) (Fig. F18; Table T4). Each tool string also contains a telemetry cartridge to communicate through the wireline to the Schlumberger data acquisition system on the drillship.

In preparation for logging, the boreholes were flushed of debris by circulating through the drill pipe to the bottom of the hole a "pill" of viscous drilling fluid (sepiolite mud mixed with seawater; density ~8.8 ppg, or ~1.055 g/cm^3; if weighted with barite, density ~10.5 ppg, or ~1.258 g/cm^3). The BHA was pulled up to 80–100 mbsf. The tool strings were then lowered downhole by a seven-conductor wireline cable in sequential runs. During a run, each lowering or hauling-up of the tool string while collecting data constitutes a pass. During each pass, the tool strings were pulled up at constant speed, typically 250–550 m/h, to simultaneously measure several properties. During the logging runs, measured data were recorded and monitored in real time on the MCM MAXIS logging computer. A wireline heave compensator (WHC) was employed to minimize the effect of ship's heave on the tool position in the borehole (see below).

Logged properties and tool measurement principles

Logged properties and the methods that the tools use to measure them are briefly described below. The main measurements taken by the tools are listed in Table T5. More detailed information on individual tools and their geological applications is found in Ellis and Singer (2007), Goldberg (1997), Rider (1996), Schlumberger (1989, 1994), and Serra (1984, 1986). A complete online list of acronyms for the Schlumberger tools and measurement curves is available at www.apps.slb.com/cmd/.

Natural radioactivity

Two wireline gamma ray tools were used to measure natural radioactivity in the formation. The Hostile Environment Natural Gamma Ray Sonde (HNGS) is a spectral tool that uses two bismuth germanate scintillation detectors and five-window spectroscopy to determine concentrations of K, Th, and U. The radioactive isotopes of these three elements dominate the natural radiation spectrum. The HNGS filters out gamma ray energies below 500 keV, eliminating sensitivity to bentonite or KCl in the drilling mud and improving measurement accuracy.

The Enhanced Digital Telemetry Cartridge (EDTC), which is used primarily to communicate data to the surface, includes a sodium iodide scintillation detector to measure the total natural gamma ray emission. It is not a spectral tool, but it provides a high-resolution total gamma ray measurement that allows for precise correlation and depth matching between different logging runs.

Bulk density

Formation bulk density was determined with the Hostile Environment Litho-Density Sonde (HLDS). The sonde contains a radioactive cesium (^{137}Cs) gamma ray source (622 keV) and far and near gamma ray detectors mounted on a shielded skid. The skid is pressed against the borehole wall by a hydraulically activated eccentralizing caliper arm, which also measures the borehole diameter. Gamma rays emitted by the source are scattered by electrons in the formation (Compton scattering). The number of scattered gamma rays that reach the detectors is proportional to the density of electrons in the formation, which is in turn related to bulk density. Porosity may also be derived from this bulk density if the matrix (grain) density is known. Good contact between the tool and borehole wall is essential for good HLDS logs; poor contact results in underestimation of density values.

The HLDS also measures photoelectric absorption as the photoelectric effect (PEF). Photoelectric absorption of gamma rays occurs when their energy is reduced below 150 keV after being repeatedly scattered by electrons in the formation. Because PEF depends on

the atomic number of the elements in the formation, it also varies according to the chemical composition of the minerals present. The PEF of calcite = 5.08 b/e$^-$; illite = 3.03 b/e$^-$; quartz = 1.81 b/e$^-$; and kaolinite = 1.49 b/e$^-$. For example, in a clastic sequence, PEF will typically be lower in sand-rich intervals and higher in intervals containing clay, mostly because of Fe in clay minerals (Fe has a high PEF of 31.2 b/e$^-$) (Ellis and Singer, 2007).

Electrical resistivity

Typical igneous rock minerals, silica, calcite, and hydrocarbons are electrical insulators, whereas ionic solutions like pore water are conductors. Variation in electrical resistivity, therefore, is dominated by water content, and the measured resistivity can be used to evaluate porosity (via Archie's equation) for a given pore water resistivity. Two wireline tools were used to measure formation resisitivity, the High-Resolution Laterolog Array (HRLA) and the Phasor Dual Induction Tool (DIT).

The HRLA sonde sends a focused current beam into the formation and measures the current intensity necessary to maintain a constant drop in voltage across a fixed interval, providing a direct resistivity measurement. The HRLA electrode array has one central source electrode and six electrodes above and below it, which serve alternately as focusing and returning current electrodes. By rapidly changing the role of these electrodes, five resistivity profiles at different depths of investigation are simultaneously measured. The HRLA uses these resistivity profiles to estimate the true formation resistivity and also measures the resistivity of the drilling fluid in the borehole.

The DIT tool provides three measures of electrical resistivity, each with a different depth of investigation into the formation. The two induction devices (deep and medium depths of penetration) transmit high-frequency alternating currents through transmitter coils, creating magnetic fields that induce secondary currents in the formation. These currents produce a new inductive field, proportional to the conductivity of the formation, which is measured by the receiving coils. The measured conductivities are then converted to resistivity (in ohm-meters). The spherically focused resistivity is measured by an electrode device that sends a current into the formation. The amount of current needed to maintain a constant drop in voltage gives a direct measure of resistivity. This device uses several electrodes to focus the current flow into the formation so that equipotential surfaces are spherical, and has a higher vertical resolution than the induction measurements.

Elastic wave velocities

The Dipole Shear Sonic Imager (DSI) measures the transit times between sonic transmitters and an array of eight receivers. It combines replicate measurements, thus providing a measurement of compressional velocity through sediment that is relatively free from the effects of formation damage and of borehole enlargements (Schlumberger, 1989). Along with the monopole transmitters found on most sonic tools, the DSI also has two cross-dipole transmitters, which allow an additional measurement of shear wave velocity. Dipole measurements are necessary to measure shear velocities in slow formations, whose shear velocity is less than the compressional velocity of the borehole fluid. Such slow formations are often encountered in deep ocean drilling.

Electrical resistivity images

The FMS provides high-resolution electrical resistivity images of the borehole wall (Chen et al., 1987). The tool has four orthogonal arms and pads, each containing 16 button electrodes that are pressed against the borehole wall during the recording. The electrodes are arranged in two offset rows of eight electrodes each. A focused current is emitted from the button electrodes into the formation, with a return electrode near the top of the tool. Resistivity of the formation at the button electrodes is derived from the intensity of current passing through the button electrodes. Processing transforms these measurements into oriented high-resolution images that reveal the geologic structures of the borehole wall. Fine-scale features such as bedding, fracturing, slump folding, and bioturbation can be resolved; the images are oriented to magnetic north so that fabric analysis can be carried out and the dip and direction (azimuth) of planar features in the formation can be measured (Serra, 1989; Luthi, 1990; Lovell et al., 1998).

The maximum extension of the FMS caliper arms is 15 inches. In holes with a diameter larger than 15 inches, the pad contact will be inconsistent, and the FMS images may appear out of focus and too conductive. Irregular borehole walls will also adversely affect the images if the pad contact with the wall is poor. The aperture and orientation of the FMS caliper arms can also be used to identify borehole breakouts and measure stress orientation in the borehole (see below).

Ultrasonic images

The Ultrasonic Borehole Imager (UBI) is the latest generation of acoustic borehole televiewer (Zemanek et al., 1970). The UBI features a rotating transducer that emits ultrasonic pulses at a frequency of 250 or

500 kHz. The pulses are reflected by the borehole wall and then received by the same transducer. The continuous rotation of the transducer and the upward motion of the tool produce a complete image of the borehole wall.

The UBI measures both the amplitude and traveltime of the reflected signal. The measured amplitude is mostly affected by the roughness of the borehole wall, with an additional minor contribution due to the contrast in acoustic impedance between the formation and the borehole fluid. Fractures intersecting the borehole wall are typically surrounded by rough areas and can be recognized in the amplitude image. The traveltime is sampled every 2°–2.6° during the transducer rotation and gives detailed information on the borehole radius. Amplitude and traveltime are recorded together with a reference to magnetic north, permitting the orientation of images. If features (e.g., fractures) recognized in the core can be matched to those observed in the UBI images, orientation of the core is possible. The UBI measurements can also be used to measure stress orientation in the borehole through identification of borehole breakouts (see below).

Accelerometry and magnetic field measurement

Three-component acceleration and magnetic field measurements were made with the General Purpose Inclinometer Tool (GPIT). The primary purpose of this tool, which incorporates a three-component accelerometer and a three-component magnetometer, is to determine the acceleration and orientation during logging of imaging tools such as the FMS and the UBI. The measured images can then be corrected for irregular tool motion and the dip and direction (azimuth) of imaged features can be determined.

Log data quality

The principal influence on log data quality is the condition of the borehole wall. If the borehole diameter varies over short intervals because of washouts, ledges made of harder layers, or narrow ("bridged") sections, the logs from those tools that require good contact with the borehole wall (e.g., bulk density and FMS) may be degraded. Deep investigation measurements such as resistivity and sonic velocity, which do not require contact with the borehole wall, are generally less sensitive to irregularity of the borehole. The quality of the borehole is improved by minimizing the circulation of fluid while drilling, flushing the borehole to remove debris, and logging as soon as possible after drilling and hole conditioning are completed.

The quality of the logging depth determination depends on several factors. The depth of wireline log measurements is determined from the length of the logging cable played out at the winch on the ship. The seafloor is identified on the natural gamma log by the abrupt reduction in gamma ray count at the water/sediment boundary (mudline). As depth in the cores is determined from the length of the drill pipe (drillers depth), there may be discrepancies between the core depth and the wireline depth scale. Inaccuracies in the core depth scale can be due to core expansion, incomplete core recovery, incomplete heave compensation, and drill pipe stretch. The wireline log depth can be inaccurate because of incomplete heave compensation, incomplete correction for cable stretch, and cable slip. Tidal changes in sea level will also have an effect. To minimize the wireline tool motion caused by ship heave, a hydraulic wireline heave compensator adjusts for rig motion during wireline logging operations.

Wireline Heave Compensator

The WHC system is designed to compensate for the vertical motion of the ship and maintain a steady motion of the logging tools. It uses vertical acceleration measurements made by a Motion Reference Unit (MRU), located under the rig floor near the center of gravity of the ship, to calculate the vertical position of the ship. The WHC adjusts the length of the wireline by varying the distance between two pulleys that the cable passes through. Real time measurements of uphole (surface) and downhole acceleration are made simultaneously by the MRU and by the GPIT tool, respectively. An LDEO-developed software package allows these data to be analyzed and compared in real time, displaying the actual motion of the tool string and enabling the efficacy of the compensator to be evaluated.

Logging data flow and log depth scales

Data for each wireline logging run were monitored in real time and recorded using the Schlumberger MAXIS 500 system. The logging data are initially referenced to the rig floor (WRF). After logging was completed, the data were shifted to a seafloor reference (WSF) based on the step in natural gamma radiation at the sediment-water interface. These data were made available to the science party within a few days of their acquisition.

The downhole log data were also transferred onshore to LDEO for standardized data processing. The main part of the processing is depth matching to remove depth offsets between different logging runs, which results in a new depth scale (WMSF). Also, corrections are made to certain tools and logs (e.g., FMS

images are corrected for tool acceleration), documentation for the logs (with an assessment of log quality) is prepared, and the data are converted to ASCII format. Schlumberger GeoQuest's GeoFrame software package is used for most of the processing. The data are then transferred back to the ship and made available through the shipboard IODP logging database (in ASCII and digital log information standard [DLIS] formats and GIF for borehole images).

Core-log-seismic integration

A depth-traveltime relationship must be determined at each site to correlate core and log data acquired in depth with seismic reflection measurements that are a function of traveltime. This relationship can be estimated by constructing synthetic seismograms, which are computed from reflection coefficients obtained from contrasts in *P*-wave velocity and density. These velocities and densities may be measured in situ with downhole logs or on cores in the physical properties laboratory. Synthetic seismograms can be calculated using the IESX seismic interpretation package (part of the Schlumberger GeoFrame software suite), which allows for interactively adjusting the depth-traveltime relationship until a good match is achieved between features in the synthetic seismogram and the measured seismic data. A calibrated depth-traveltime relationship provides an accurate correlation of core and log data with features in the seismic reflection data (e.g., to assign ages to seismic horizons that can be correlated away from the drill site).

Borehole breakout analysis

Drilling a vertical borehole through a rock mass that is under different principal compressive horizontal stresses induces a compressive stress along the borehole wall that is strongest at the azimuth of the minimum horizontal stress. If the stress reaches the rock strength, the borehole wall can fail and develop characteristic breakouts that are located 180° apart and mark the minimum horizontal stress direction. Therefore, borehole breakouts are key indicators of the state of stress in the subsurface (Zoback et al., 2003). Downhole logging measurements can indicate the presence and measure the orientation of borehole breakouts from the orientation of four-arm caliper tools and from borehole imaging. Due to cable torque, four-arm caliper tools such as the FMS rotate while they are being pulled uphole. If breakouts are present, a pair of caliper arms will tend to remain within the breakout, stopping tool rotation. The breakout direction can be determined from the orientation of the pair of caliper arms that measures the larger borehole diameter (Bell and Gough, 1979; Plumb and Hickman, 1985; Lin et al., 2010). Data acquired by an ultrasonic borehole televiewer such as the UBI can also image breakouts. Breakout surfaces are rough and appear as persistent vertical stripes of low reflectivity 180° apart in reflection amplitude images. Traveltime data can provide detailed cross sections of the borehole radius that show the width and depth of breakouts (Plumb and Hickman, 1985; Zoback et al., 2003).

References

ASTM International, 1990. Standard method for laboratory determination of water (moisture) content of soil and rock (Standard D2216–90). In *Annual Book of ASTM Standards for Soil and Rock* (Vol. 04.08): Philadelphia (Am. Soc. Testing Mater.). [revision of D2216-63, D2216-80]

Bandy, O.L., and Arnal, R.E., 1957. Distribution of Recent foraminifera off the west coast of Central America. *AAPG Bull.,* 41(9):2037–2053. **http://archives.datapages.com/data/bulletns/1957-60/data/pg/0041/0009/2000/2037.htm**

Barckhausen, U., Ranero, C.R., von Huene, R., Cande, S.C., and Roeser, H.A., 2001. Revised tectonic boundaries in the Cocos plate off Costa Rica: implications for the segmentation of the convergent margin and for plate tectonic models. *J. Geophys. Res.: Solid Earth,* 106(B9):19207–19220. **doi:10.1029/2001JB000238**

Bell, J.S., and Gough, D.I., 1979. Northeast-southwest compressive stress in Alberta: evidence from oil wells. *Earth Planet. Sci. Lett.,* 45(2):475–482. **doi:10.1016/0012-821X(79)90146-8**

Blum, P., 1997. Physical properties handbook: a guide to the shipboard measurement of physical properties of deep-sea cores. *ODP Tech. Note,* 26. **doi:10.2973/odp.tn.26.1997**

Boggs, S., Jr., 2005. *Principles of Sedimentology and Stratigraphy* (4th ed.): Saddle River, New Jersey (Prentice-Hall).

Boyce, R.E., 1977. Deep Sea Drilling Project procedures for shear strength measurement of clayey sediment using modified Wykeham Farrance laboratory vane apparatus. *In* Barker, P.F., Dalziel, I.W.D., et al., *Init. Repts. DSDP,* 36: Washington, DC (U.S. Govt. Printing Office), 1059–1068. **doi:10.2973/dsdp.proc.36.1977**

Bullard, E.C., 1939. Heat flow in South Africa. *Proc. R. Soc. London, Ser. A,* 173(955):474–502. **doi:10.1098/rspa.1939.0159**

Bukry, D., 1973. Low-latitude coccolith biostratigraphic zonation. *In* Edgar, N.T., Saunders, J.B., et al., *Init. Repts. DSDP,* 15: Washington, DC (U.S. Govt. Printing Office), 685–703. **doi:10.2973/dsdp.proc.15.116.1973**

Bukry, D., 1975. Coccolith and silicoflagellate stratigraphy, northwestern Pacific Ocean, Deep Sea Drilling Project Leg 32. *In* Larson, R.L., Moberly, R., et al., *Init. Repts. DSDP,* 32: Washington, DC (U.S. Govt. Printing Office), 677–701. **doi:10.2973/dsdp.proc.32.124.1975**

Cande, S.C., and Kent, D.V., 1995. Revised calibration of the geomagnetic polarity timescale for the Late Creta-

ceous and Cenozoic. *J. Geophys. Res.: Solid Earth,* 100(B4):6093–6095. doi:10.1029/94JB03098

Chen, M.Y., Ekstrom, M.P., Dahan, C.A., Lloyd, P.M., and Rossi, D.J., 1987. Formation imaging with microelectrical scanning arrays. *Log Analyst,* 28(3):294–306.http://www.onepetro.org/mslib/servlet/onepetropreview?id=SPWLA-1987-v28n3a4

Clark, S.P. (Ed.), 1966. *Handbook of Physical Constants*. Mem.—Geol. Soc. Am., 97.

Cox, A., and Gordon, R.G., 1984. Paleolatitudes determined from paleomagnetic data from vertical cores. *Rev. Geophys. Space Phys.,* 22(1):47–71. doi:10.1029/RG022i001p00047

Crouch, R.W., and Poag, C.W., 1987. Benthic foraminifera of the Panamanian Province; distribution and origins. *J. Foraminiferal Res.,* 17(2):153–176. doi:10.2113/gsjfr.17.2.153

DeMets, C., Gordon, R.G., and Argus, D.F., 2010. Geologically current plate motions. *Geophys. J. Int.,* 181(1):1–80. doi:10.1111/j.1365-246X.2009.04491.x

DeMets, C., Gordon, R.G., and Argus, D.F., 2011. Erratum: DeMets, C., Gordon, R.G., and Argus, D.F., 2010. Geologically current plate motions (*Geophys. J. Int.,* 181:1–80). *Geophys. J. Int.,* 187(1):538. doi:10.1111/j.1365-246X.2011.05186.x

Droser, M.L., and Bottjer, D.J., 1986. A semiquantitative field classification of ichnofabric. *J. Sediment. Res.,* 56(4):558–559. doi:10.1306/212F89C2-2B24-11D7-8648000102C1865D

Droser, M.L., and Bottjer, D.J., 1991. Trace fossils and ichnofabric in Leg 119 cores. *In* Barron, J., Larsen, B., et al., *Proc. ODP, Sci. Results,* 119: College Station, TX (Ocean Drilling Program), 635–641. doi:10.2973/odp.proc.sr.119.206.1991

Ellis, D.V., and Singer, J.M., 2007. *Well Logging for Earth Scientists* (2nd ed.): Dordrecht, The Netherlands (Springer).

Evans, H.B., 1965. GRAPE—a device for continuous determination of material density and porosity. *Trans. SPWLA Annu. Logging Symp.:* 6(2):B1–B25. http://www.spwla.org/cgi-bin/shop.pl?choice=display;item_id=82

Expedition 334 Scientists, 2012. Methods. *In* Vannucchi, P., Ujiie, K., Stroncik, N., Malinverno, A., and the Expedition 334 Scientists, *Proc. IODP,* 334: Tokyo (Integrated Ocean Drilling Program Management International, Inc.). doi:10.2204/iodp.proc.334.102.2012

Expedition 342 Scientists, in press. Site U1405. *In* Norris, R.D., Wilson, P.A., Blum, P., and the Expedition 342 Scientists, *Proc. IODP,* 342: Tokyo (Integrated Ocean Drilling Program Management International, Inc.). doi:10.2204/iodp.proc.342.106.2014

Fisher, R.V., and Schmincke, H.-U., 1984. *Pyroclastic Rocks:* New York (Springer-Verlag).

Fuller, M., 1969. Magnetic orientation of borehole cores. *Geophysics,* 34(5):772–774. doi:10.1190/1.1440047

Galehouse, J.S., 1969. Counting grain mounts: number percentage vs. number frequency. *J. Sediment. Res.,* 39(2):812–815. doi:10.1306/74D71D3E-2B21-11D7-8648000102C1865D

Galehouse, J.S., 1971. Point counting. *In* Carver, R.E. (Ed.), *Procedures in Sedimentary Petrology:* New York (Wiley-Interscience), 385–407.

Gee, J.S., Tauxe, L., and Constable, C., 2008. AMSSpin: a LabVIEW program for measuring the anisotropy of magnetic susceptibility with the Kappabridge KLY-4S. *Geochem., Geophys., Geosyst.,* 9(8):Q08Y02. doi:10.1029/2008GC001976

Gieskes, J.M., Gamo, T., and Brumsack, H., 1991. Chemical methods for interstitial water analysis aboard *JOIDES Resolution. ODP Tech. Note,* 15. doi:10.2973/odp.tn.15.1991

Goldberg, D., 1997. The role of downhole measurements in marine geology and geophysics. *Rev. Geophys.,* 35(3):315–342. doi:10.1029/97RG00221

Gradstein, F.M., Ogg, J.G., Schmitz, M.D., and Ogg, G.M. (Eds.), 2012. *The Geological Time Scale 2012:* Amsterdam (Elsevier).

Harms, J.C., and Choquette, P.W., 1965. Geologic evaluation of a gamma-ray porosity device. *Trans. SPWLA Annu. Logging Symp.:* 6(2):C1–C37.

Heard, T.G., and Pickering, K.T., 2008. Trace fossils as diagnostic indicators of deep-marine environments, middle Eocene Ainsa-Jaca Basin, Spanish Pyrenees. *Sedimentology,* 55(4):809–844. doi:10.1111/j.1365-3091.2007.00922.x

Heinz, P., Ruschmeier, W., and Hemleben, C., 2008. Live benthic foraminiferal assemblages at the Pacific continental margin of Costa Rica and Nicaragua. *J. Foraminiferal Res.,* 38(3):215–227. doi:10.2113/gsjfr.38.3.215

Ingle, J.C., Jr., Keller, G., and Kolpack, R.L., 1980. Benthic foraminiferal biofacies, sediments and water masses of the southern Peru-Chile Trench area, southeastern Pacific Ocean. *Micropaleontology,* 26(2):113–150. doi:10.2307/1485435

Janz, G.J., and Singer, S.K., 1975. Copenhagen Standard Sea Water: conductivity and salinity. *J. Solution Chem.,* 4(12):995–1003. doi:10.1007/BF01074741

Keenan, J.H., Keyes, F.G., Hill, P.G., and Moore, J.G., 1978. *Steam Tables: Thermodynamic Properties of Water Including Vapor, Liquid, and Solid Phases:* New York (John Wiley & Sons).

Kirschvink, J.L., 1980. The least-squares line and plane and the analysis of palaeomagnetic data. *Geophys. J. R. Astron. Soc.,* 62(3):699–718. doi:10.1111/j.1365-246X.1980.tb02601.x

Kvenvolden, K.A., and McDonald, T.J., 1986. Organic geochemistry on the *JOIDES Resolution*—an assay. *ODP Tech. Note,* 6: College Station, TX (Ocean Drilling Program). doi:10.2973/odp.tn.6.1986

Lin, W., Doan, M.-L., Moore, J.C., McNeill, L., Byrne, T.B., Ito, T., Saffer, D., Conin, M., Kinoshita, M., Sanada, Y., Moe, K.T., Araki, E., Tobin, H., Boutt, D., Kano, Y., Hayman, N.W., Flemings, P., Huftile, G.J., Cukur, D., Buret, C., Schleicher, A.M., Efimenko, N., Kawabata, K., Buchs, D.M., Jiang, S., Kameo, K., Horiguchi, K., Wiersberg, T., Kopf, A., Kitada, K., Eguchi, N., Toczko, S., Takahashi, K., and Kido, Y., 2010. Present-day principal horizontal stress orientations in the Kumano forearc basin of the southwest Japan subduction zone determined from

IODP NanTroSEIZE drilling Site C0009. *Geophys. Res. Lett.,* 37(13):L13303. doi:10.1029/2010GL043158

Lin, W., Yeh, E.-C., Ito, H., Hirono, T., Soh, W., Wang, C.-Y., Ma, K.-F., Hung, J.-H., and Song, S.-R., 2007. Preliminary results of stress measurements using drill cores of TCDP Hole-A: an application of anelastic strain recovery method to three-dimensional in-situ stress determination. *Terr. Atmos. Oceanic Sci.,* 18(2):379. doi:10.3319/TAO.2007.18.2.379(TCDP)

Loeblich, A.R., Jr., and Tappan, H., 1988. *Foraminiferal Genera and Their Classification:* New York (Van Nostrand Reinhold).

Lovell, M.A., Harvey, P.K., Brewer, T.S., Williams, C., Jackson, P.D., and Williamson, G., 1998. Application of FMS images in the Ocean Drilling Program: an overview. *In* Cramp, A., MacLeod, C.J., Lee, S.V., and Jones, E.J.W. (Eds.), *Geological Evolution of Ocean Basins: Results from the Ocean Drilling Program.* Geol. Soc. Spec. Publ., 131(1):287–303. doi:10.1144/GSL.SP.1998.131.01.18

Luthi, S.M., 1990. Sedimentary structures of clastic rocks identified from electrical borehole images. *In* Hurst, A., Lovell, M.A., and Morton, A.C. (Eds.), *Geological Applications of Wireline Logs.* Geol. Soc. Spec. Publ., 48(1):3–10. doi:10.1144/GSL.SP.1990.048.01.02

Manheim, F.T., and Sayles, F.L., 1974. Composition and origin of interstitial waters of marine sediments, based on deep sea drill cores. *In* Goldberg, E.D. (Ed.), *The Sea* (Vol. 5): *Marine Chemistry: The Sedimentary Cycle:* New York (Wiley), 527–568.

Martini, E., 1971. Standard Tertiary and Quaternary calcareous nannoplankton zonation. *In* Farinacci, A. (Ed.), *Proc. Second Planktonic Conf. Roma 1970:* Rome (Ed. Tecnosci.), 2:739–785.

Matsuki, K., 1991. Three-dimensional in situ stress measurement with anelastic strain recovery of a rock core. *Proc.—Int. Congr. Rock Mech.,* 7:557–560. http://www.onepetro.org/mslib/servlet/onepetropreview?id=ISRM-7CONGRESS-1991-110

McFadden, P.L., and Reid, A.B., 1982. Analysis of paleomagnetic inclination data. *Geophys. J. R. Astron. Soc.,* 69(2):307–319. doi:10.1111/j.1365-246X.1982.tb04950.x

Munsell Color Company, Inc., 2000. *Munsell Soil Color Chart*: New York (Gretag-Macbeth).

Murray, R.W., Miller, D.J., and Kryc, K.A., 2000. Analysis of major and trace elements in rocks, sediments, and interstitial waters by inductively coupled plasma–atomic emission spectrometry (ICP-AES). *ODP Tech. Note,* 29. doi:10.2973/odp.tn.29.2000

Nigrini, C., and Moore, T.C., 1979. *A Guide to Modern Radiolaria.* Spec. Publ.—Cushman Found. Foraminiferal Res., 16.

Okada, H., and Bukry, D., 1980. Supplementary modification and introduction of code numbers to the low-latitude coccolith biostratigraphic zonation (Bukry, 1973; 1975). *Mar. Micropaleontol.,* 5:321–325. doi:10.1016/0377-8398(80)90016-X

Pindell, J.L., Cande, S.C., Pitman, W.C., III, Rowley, D.B., Dewey, J.F., Labrecque, J., and Haxby, W., 1988. A plate-kinematic framework for models of Caribbean evolution. *Tectonophysics,* 155(1–4):121–138. doi:10.1016/0040-1951(88)90262-4

Plumb, R.A., and Hickman, S.H., 1985. Stress-induced borehole elongation: a comparison between the four-arm dipmeter and the borehole televiewer in the Auburn geothermal well. *J. Geophys. Res.: Solid Earth,* 90(B7):5513–5521. doi:10.1029/JB090iB07p05513

Ratcliffe, E.H., 1960. The thermal conductivities of ocean sediments. *J. Geophys. Res.,* 65(5):1535–1541. doi:10.1029/JZ065i005p01535

Richter, C., Acton, G., Endris, C., and Radsted, M., 2007. Handbook for shipboard paleomagnetists. *ODP Tech. Note,* 34. doi:10.2973/odp.tn.34.2007

Rider, M.H., 1996. *The Geological Interpretation of Well Logs* (2nd ed.): Caithness (Whittles Publ.).

Riedel, W.R., and Sanfilippo, A., 1970. Radiolaria, Leg 4, Deep Sea Drilling Project. *In* Bader, R.G., Gerard, R.D., et al., *Init. Repts. DSDP,* 4: Washington, DC (U.S. Govt. Printing Office), 503–575. doi:10.2973/dsdp.proc.4.124.1970

Rothwell, R.G., 1989. *Minerals and Mineraloids in Marine Sediments: An Optical Identification Guide:* London (Elsevier).

Sanfilippo, A., and Nigrini, C., 1998. Code numbers for Cenozoic low latitude radiolarian biostratigraphic zones and GPTS conversion tables. *Mar. Micropaleontol.,* 33(1–2):109–117, 121–156. doi:10.1016/S0377-8398(97)00030-3

Sanfilippo, A., Westberg-Smith, M.J., and Riedel, W.R., 1985. Cenozoic Radiolaria. *In* Bolli, H.M., Saunders, J.B., and Perch-Nielsen, K. (Eds.), *Plankton Stratigraphy* (Vol. 2): *Radiolaria, Diatoms, Silicoflagellates, Dinoflagellates, and Ichthyoliths:* Cambridge (Cambridge Univ. Press), 631–712.

Schlumberger, 1989. *Log Interpretation Principles/Applications:* Houston (Schlumberger Educ. Serv.), SMP–7017.

Schlumberger, 1994. *IPL Integrated Porosity Lithology:* Houston (Schlumberger Wireline Testing), SMP-9270.

Serra, O., 1984. *Fundamentals of Well-Log Interpretation* (Vol. 1): *The Acquisition of Logging Data:* Amsterdam (Elsevier).

Serra, O., 1986. *Fundamentals of Well-Log Interpretation* (Vol. 2): *The Interpretation of Logging Data.* Amsterdam (Elsevier).

Serra, O., 1989. *Formation MicroScanner Image Interpretation:* Houston (Schlumberger Educ. Serv.), SMP-7028.

Smith, P.B., 1963. Quantitative and qualitative analysis of the family *Bolivinidae. U.S. Geol. Surv. Prof. Pap.,* 429-A.

Smith, P.B., 1964. Ecology of benthonic species. *U.S. Geol. Surv. Prof. Pap.* 429–B.

Takahashi, K., 1991. *Radiolaria: Flux, Ecology, and Taxonomy in the Pacific and Atlantic.* Ocean Biocoenosis Ser., 3. doi:10.1575/1912/408

Tauxe, L., Tucker, P., Peterson, N.P., and LaBrecque, J.L., 1984. Magnetostratigraphy of Leg 73 sediments. *In* Hsü, K.J., LaBrecque, J.L., et al., *Init. Repts. DSDP,* 73: Washington, DC (U.S. Govt. Printing Office), 609–621. doi:10.2973/dsdp.proc.73.123.1984

Vacquier, V., 1985. The measurement of thermal conductivity of solids with a transient linear heat source on the

plane surface of a poorly conducting body. *Earth Planet. Sci. Lett.,* 74(2–3):275–279. **doi:10.1016/0012-821X(85)90027-5**

van der Plas, L., and Tobi, A.C., 1965. A chart for judging the reliability of point counting results. *Am. J. Sci.,* 263(1):87–90. **doi:10.2475/ajs.263.1.87**

Von Herzen, R., and Maxwell, A.E., 1959. The measurement of thermal conductivity of deep-sea sediments by a needle-probe method. *J. Geophys. Res.,* 64(10):1557–1563. **doi:10.1029/JZ064i010p01557**

Wentworth, C.K., 1922. A scale of grade and class terms for clastic sediments. *J. Geol.,* 30(5):377–392. **doi:10.1086/622910**

Zemanek, J., Glenn, E.E., Norton, L.J., and Caldwell, R.L., 1970. Formation evaluation by inspection with the borehole televiewer. *Geophysics,* 35(2):254–269. **doi:10.1190/1.1440089**

Zidjerveld, J.D.A., 1967. A. C. demagnetization of rocks: analysis of results. *In* Collinson, D.W., Creer, K.N., and Runcorn, S.K. (Eds.), *Methods in Paleomagnetism:* Amsterdam (Elsevier), 254–286.

Zoback, M.D., Barton, C.A., Brudy, M., Castillo, D.A., Finkbeiner, T., Grollimund, B.R., Moos, D.B., Peska, P., Ward, C.D., and Wiprut, D.J., 2003. Determination of stress orientation and magnitude in deep wells. *Int. J. Rock Mech. Min. Sci.,* 40(7–8):1049–1076. **doi:10.1016/j.ijrmms.2003.07.001**

Zoth, G., and Haenel, R., 1988. Appendix: 1. *In* Haenel, R., Rybach, L., and Stegena, L. (Eds.), *Handbook of Terrestrial Heat-Flow Density Determination: with Guidelines and Recommendations of the International Heat Flow Commission:* Dordrecht (Kluwer Acad. Publ.), 449–4668.

Publication: 11 December 2013
MS 344-102

Figure F1. IODP convention for naming sites, holes, cores, sections, and samples.

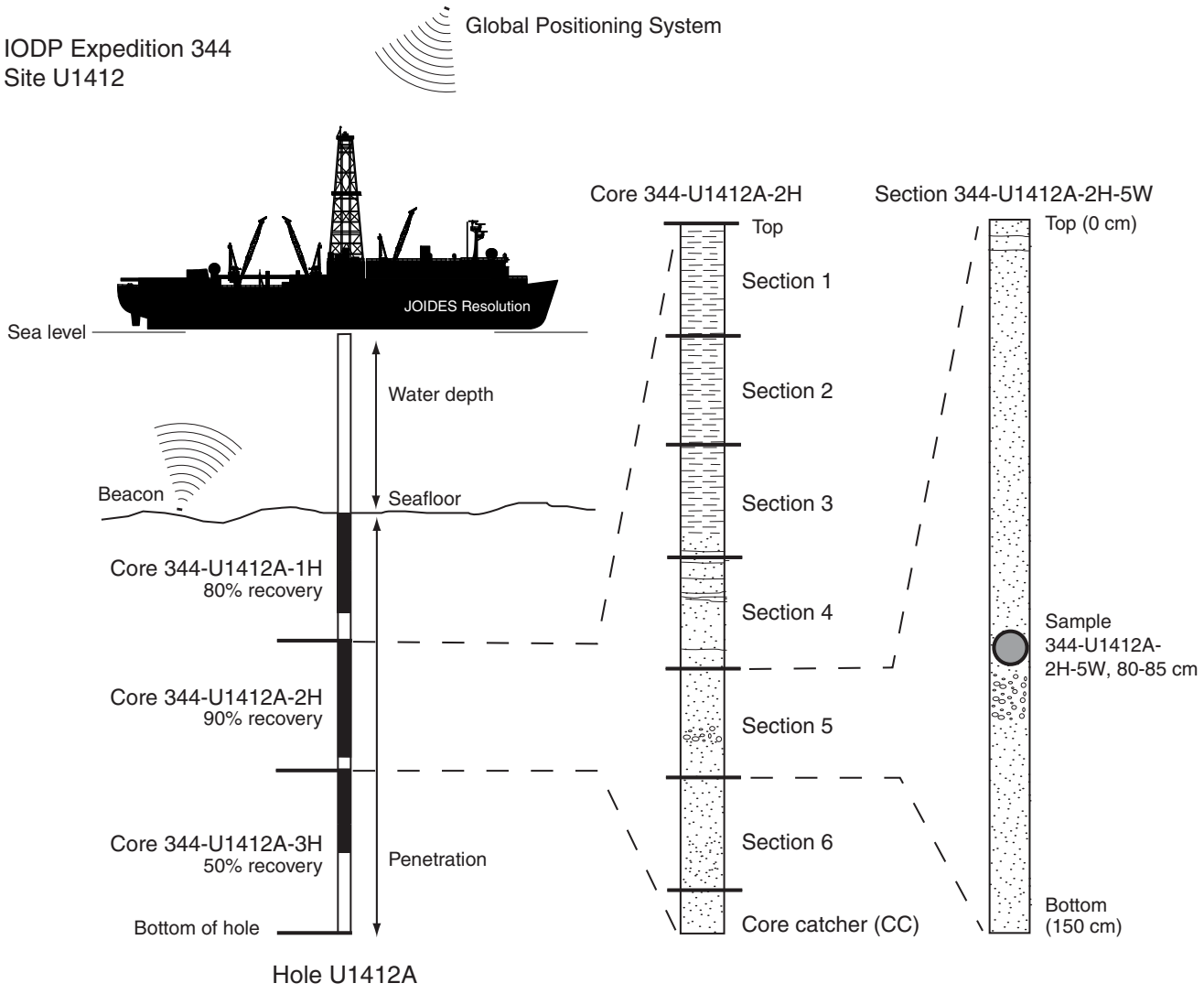

Figure F2. Core flow and types of samples and measurements taken during Expedition 344. WRMSL = Whole-Round Multisensor Logger, GRA = gamma ray attenuation, MS = magnetic susceptibility, PWL = *P*-wave logger, NGR = natural gamma radiation, TCON = thermal conductivity, SHIL = Section Half Imaging Logger, SHMSL = Section Half Multisensor Logger, MSP = point magnetic susceptibility, RSC = color spectroscopy, SRM = superconducting rock magnetometer, PWB = bayonet *P*-wave velocity, AVS = automated vane shear, TOR = Torvane, PEN = penetrometer, MAD = moisture and density, PWC = caliper *P*-wave velocity, GC = gas chromatography, SRA = source rock analyzer, IW = interstitial water, IC = ion chromatography, ICP-AES = inductively coupled plasma–atomic emission spectroscopy, TOC = total organic carbon, XRD = X-ray diffraction, CHNS = carbon, hydrogen, nitrogen, sulfur elemental analysis.

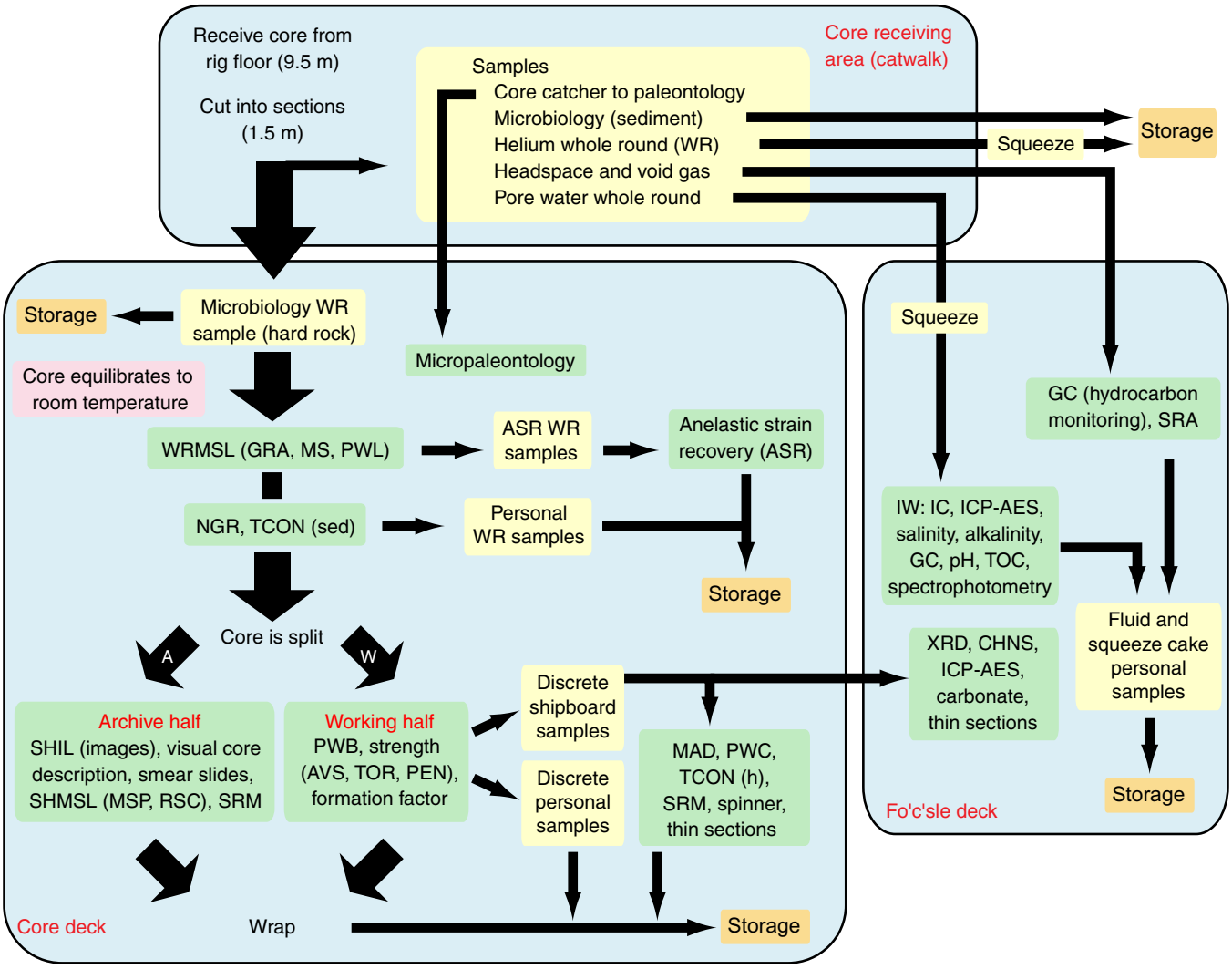

Figure F3. Symbols used in sediment visual core descriptions, Expedition 344. (Continued on next page.)

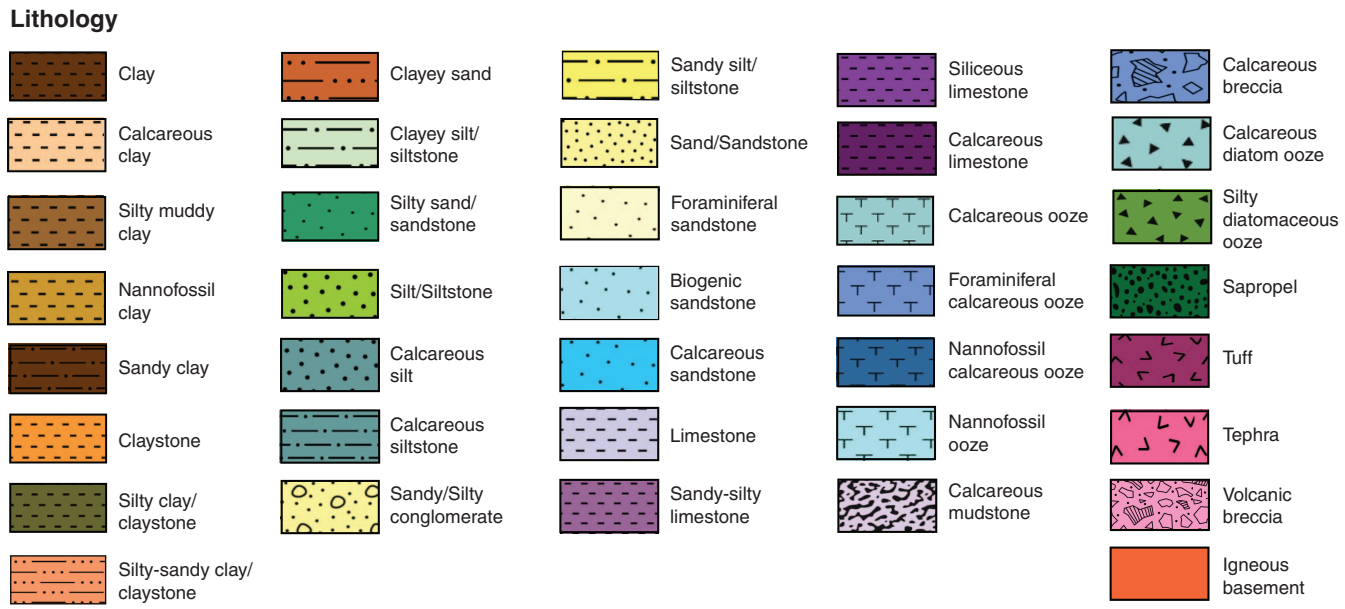

Figure F3 (continued).

Figure F4. Diffractograms of mixtures of standard minerals showing positions of diagnostic XRD peaks used to calculate relative mineral abundances. Cl = total clay minerals, Q = quartz, P = plagioclase, Cc = calcite.

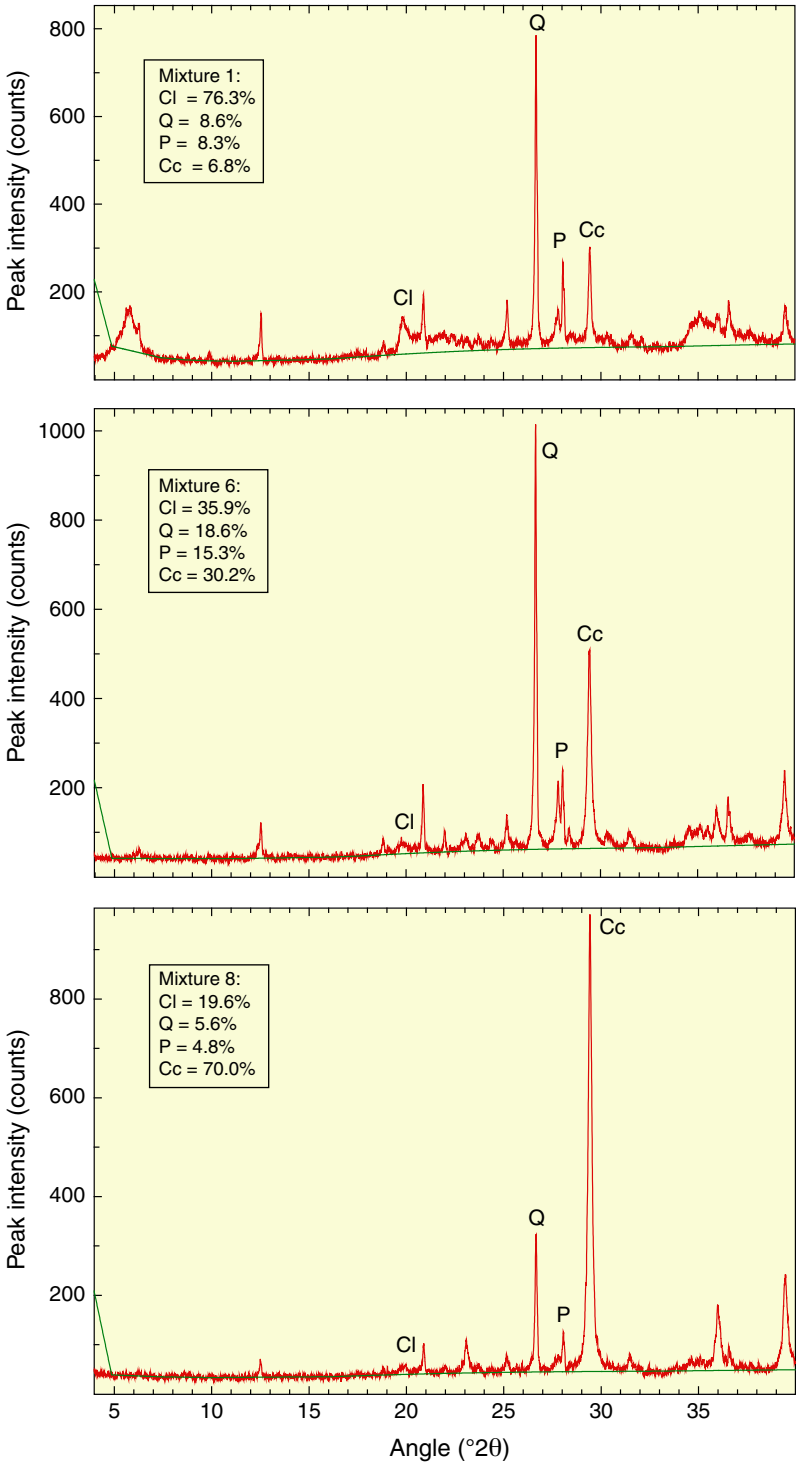

Figure F5. Symbols used in hard rock visual core descriptions, Expedition 344.

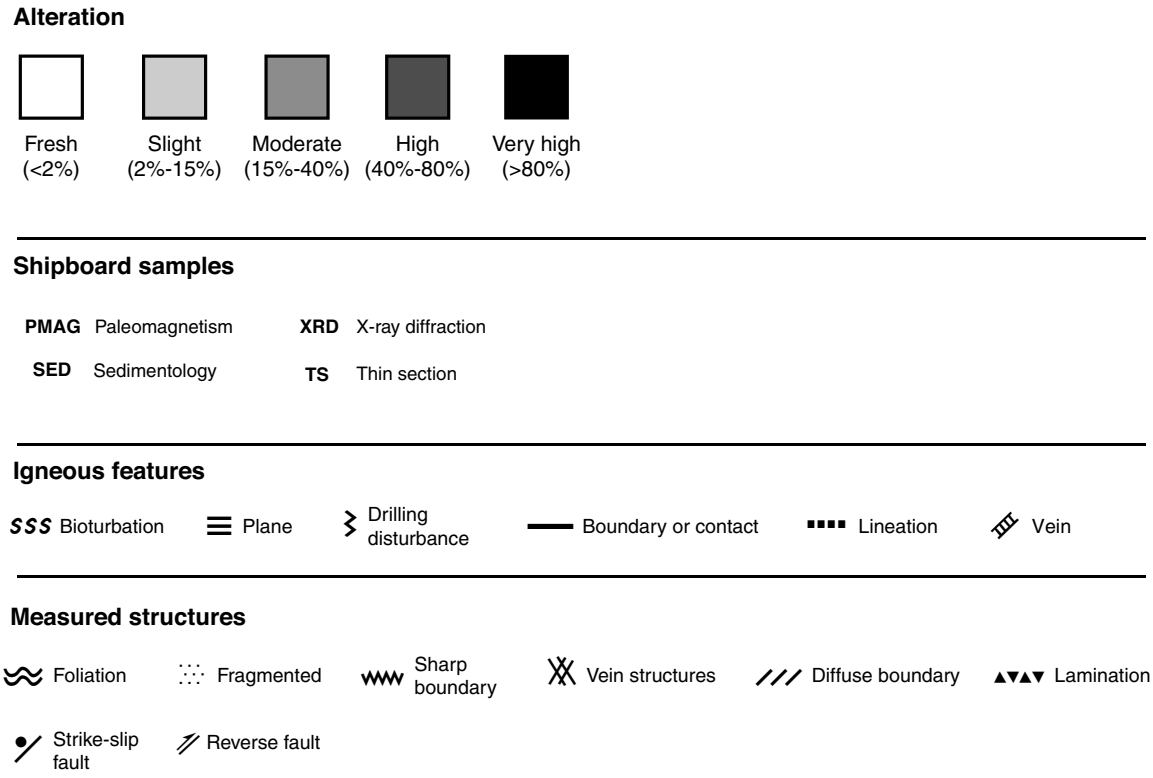

Figure F6. Example of log sheet used to record structural and orientation data and observations from the working half of a split core, Expedition 344.

Exp. 344 Structural Geology Observation Sheet

Site:

Core	Sec.	Structure ID	Top of struct	Bottom of struct	Core face app. plunge		2nd app. plunge		Striation on surface		Coherent int for pmag		P-mag pole		Note
					az	plunge	az	plunge	rake	from	top	bottom	Dec	Inc	

Figure F7. Photograph of protractor used to measure apparent dips, trends, plunges, and rakes on planar and linear features in a split core, Expedition 344.

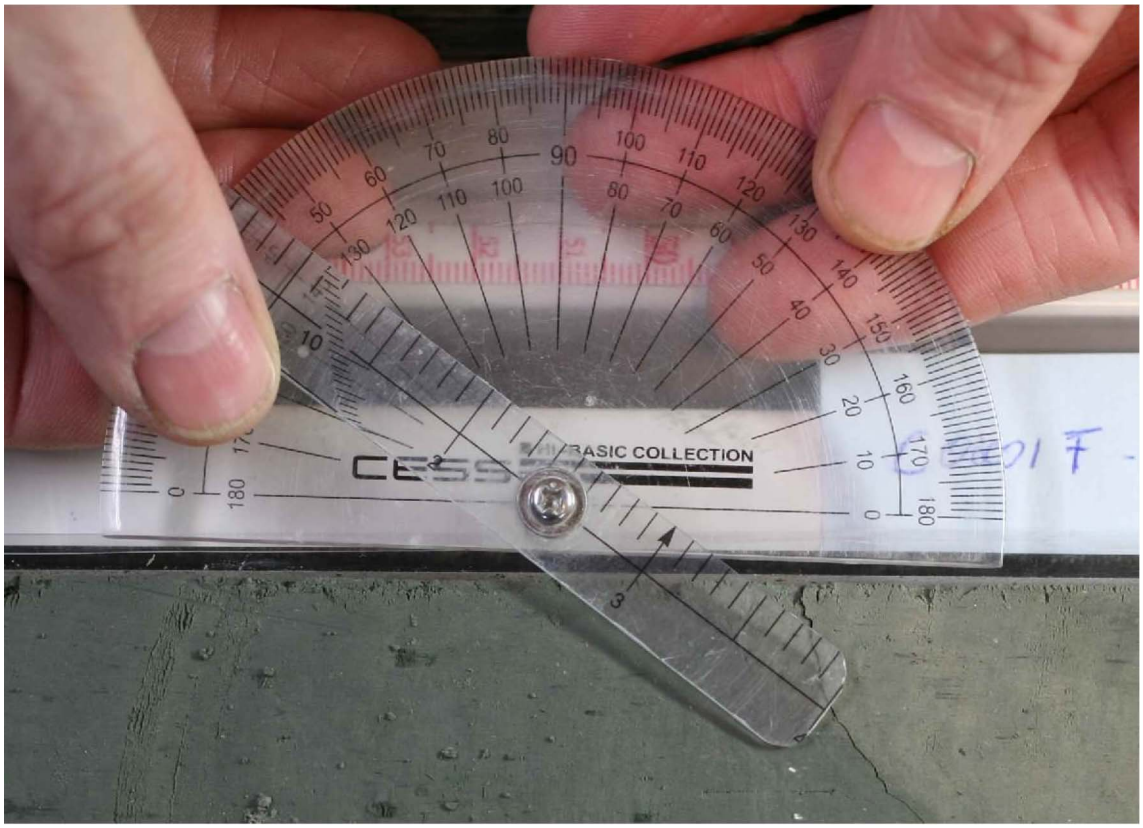

Figure F8. Diagram of core reference frame and *x*-, *y*-, and *z*-coordinates used in orientation data calculations, Expedition 344.

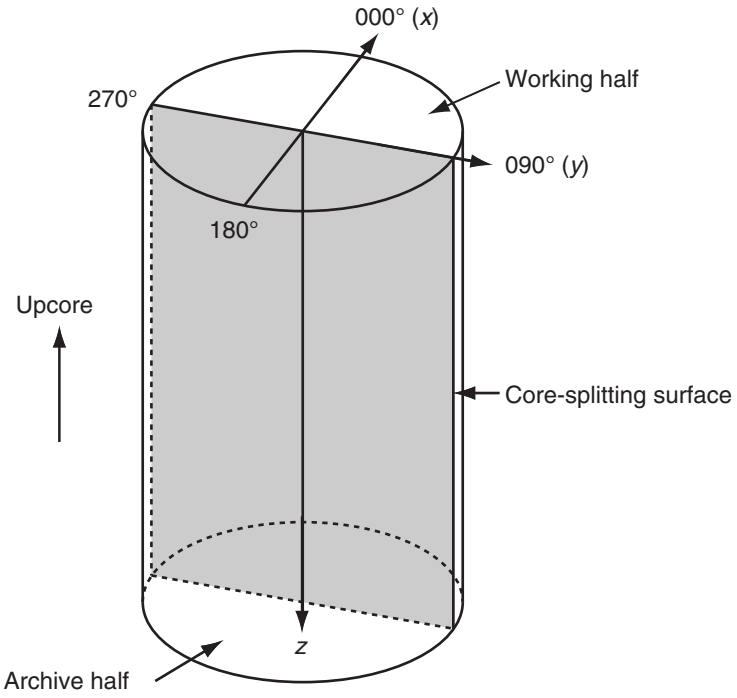

Figure F9. Lower hemisphere equal area projection showing the procedure for converting 2-D measured data to 3-D data. **A.** Plane attitude determined from two apparent dips on two surfaces. Striation on the plane is also plotted. **B.** Restoration to the geographic coordinates using paleomagnetic data.

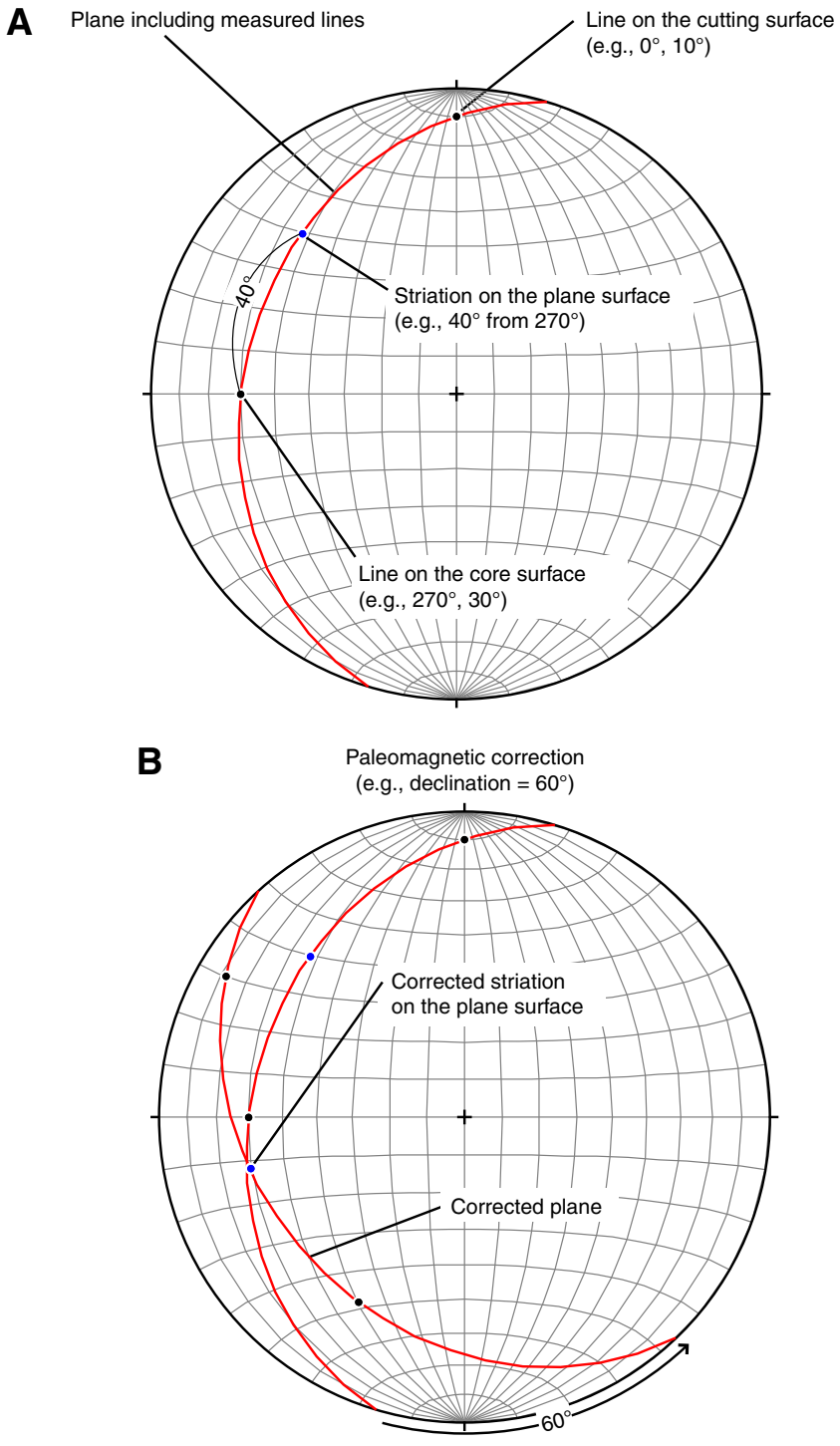

Figure F10. Diagram showing calculation of plane orientation (shaded) from two apparent dips. Intersections of split core surface, section perpendicular to split core surface, and section parallel to core direction with plane of interest are shown. (α_1, β_1) and (α_2, β_2) are the azimuths and dips of traces of the plane on two sections, respectively; v_1 and v_2 are unit vectors parallel to traces of the plane on two sections; and v_n is the unit vector normal to plane.

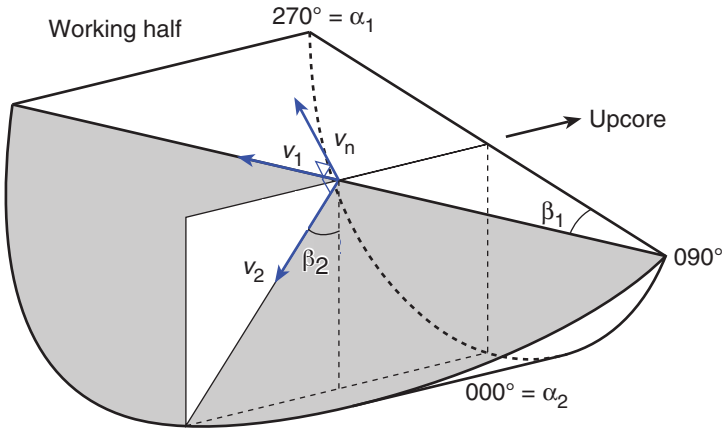

Figure F11. Diagrams of dip direction (α_d), right-hand rule strike (α_s), and dip (β) of a plane deduced from its normal azimuth (α_n) and dip (β_n). v_n denotes the unit vector normal to plane. **A.** $\beta_n < 0°$. **B.** $\beta_n \geq 0°$.

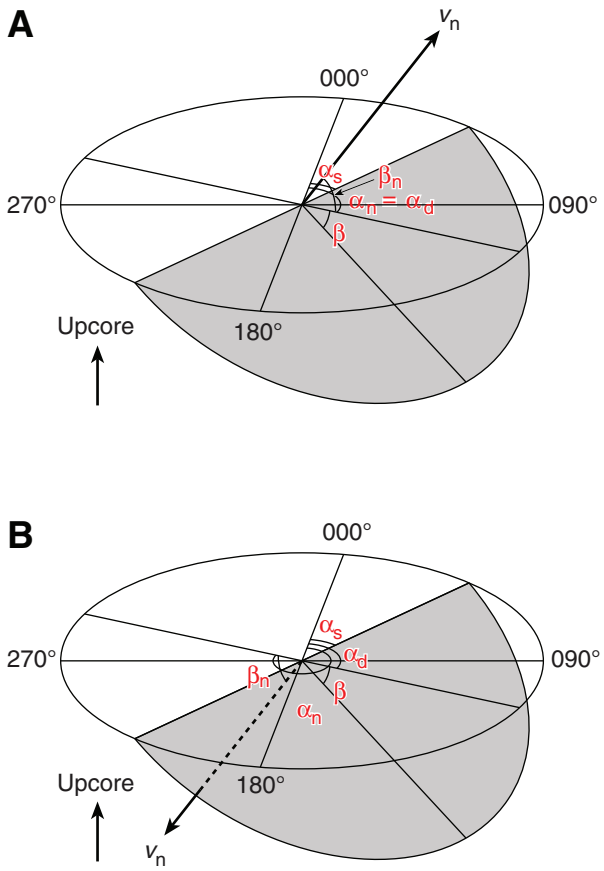

Figure F12. Diagram of apparent rake measurement of striations on a fault surface from 270° direction of split core surface trace. ϕ_a = apparent rake, v_n = unit vector normal to fault plane, v_c = unit vector normal to split core surface, v_i = unit vector parallel to the intersection line between fault plane and split core surface.

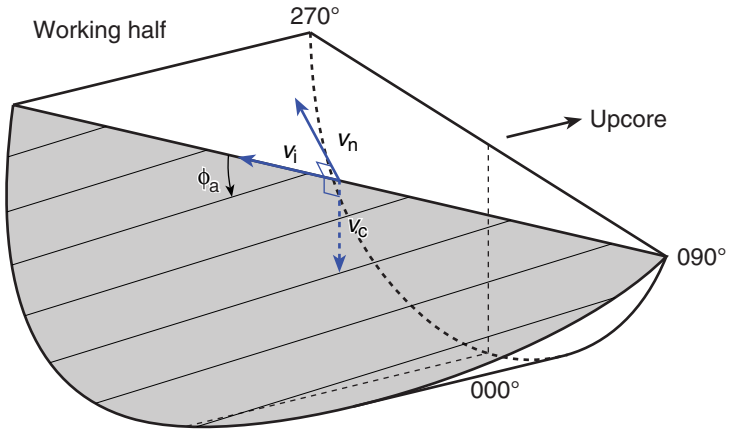

Figure F13. Diagrams of rake of striations (ϕ) deduced from the rake of intersection line between fault plane and split core surface (ϕ_i) and apparent rake measured (ϕ_a). α_s = right-hand rule strike of fault plane, v_n = unit vector normal to fault plane, v_c = unit vector normal to split core surface, v_i = unit vector parallel to intersection line between fault plane and split core surface. **A.** ϕ_a from top or 90° direction when fault plane dips west. **B.** ϕ_a from bottom or 90° direction when fault plane dips east. **C.** ϕ_a from top or 270° direction when fault plane dips east. **D.** ϕ_a from bottom or 270° direction when fault plane dips west.

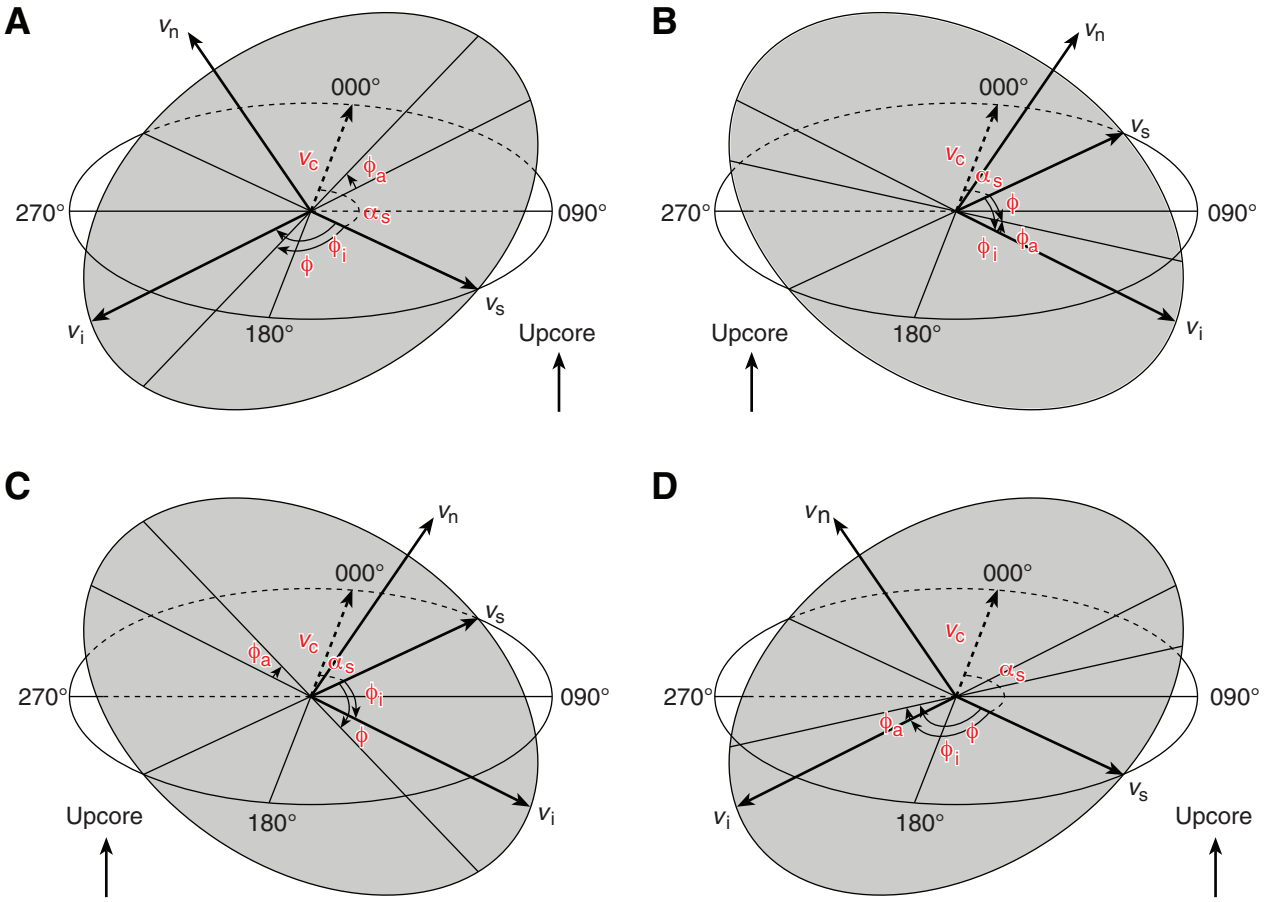

Figure F14. Diagrams of azimuth correction based on paleomagnetic data. α_p = paleomagnetic declination, α_d and α_s = dip direction and right-hand rule strike of a plane. **A.** $\beta_p \geq 0°$. **B.** $\beta_p < 0°$.

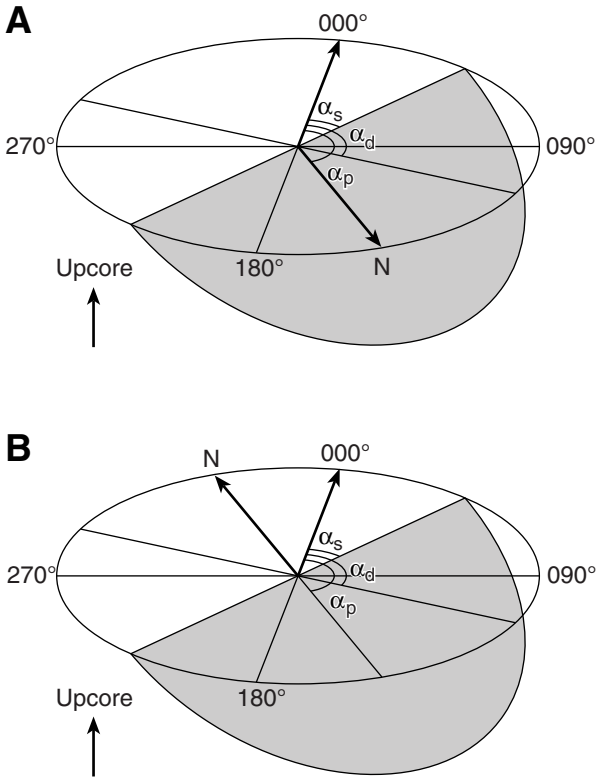

Figure F15. A. Coordinates of paleomagnetic samples (after Richter et al., 2007). **B.** Natsuhara-Giken sampling cubes (7 cm^3 volume) with sample coordinate system used during Expedition 344. Hatched arrow is parallel to the up arrow on the sample cube and points in the –*z*-direction. **C.** Coordinate system used for the superconducting rock magnetometer onboard the *JOIDES Resolution*.

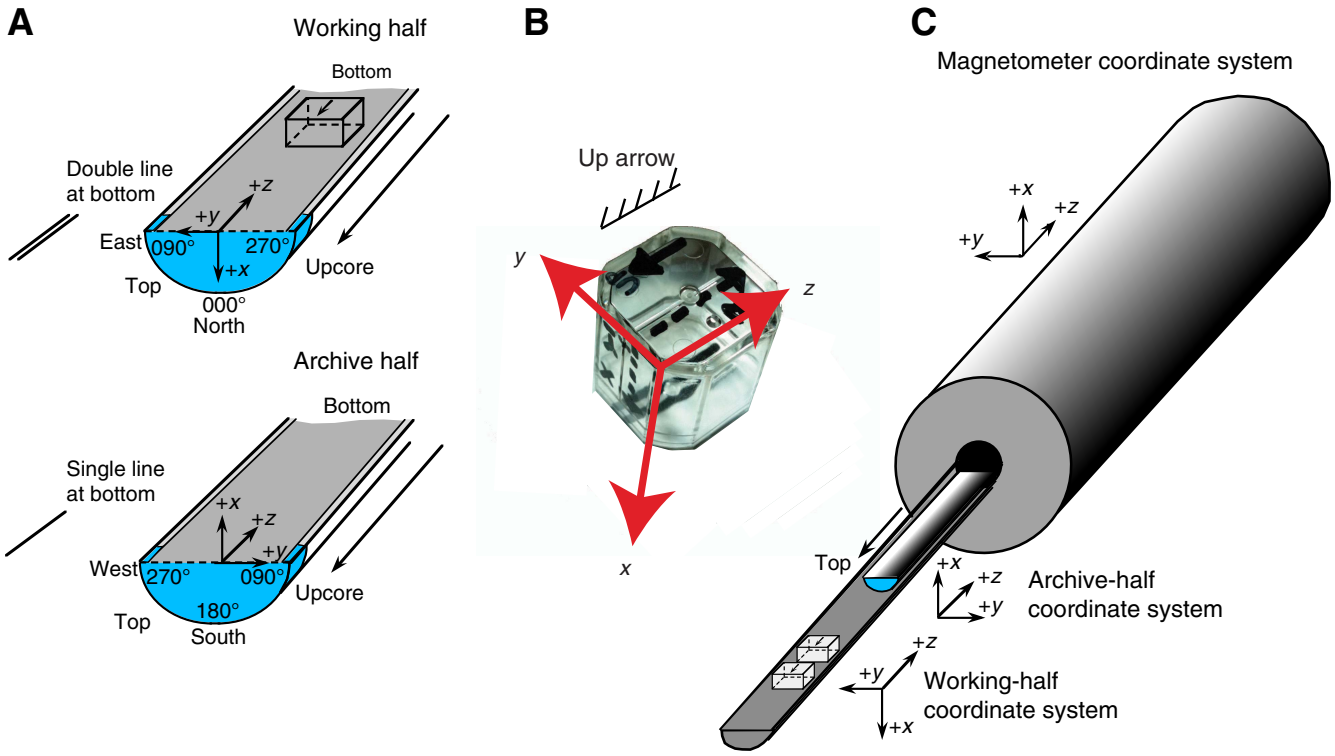

Figure F16. Positioning of discrete samples in the automatic holder of the JR-6A spinner magnetometer.

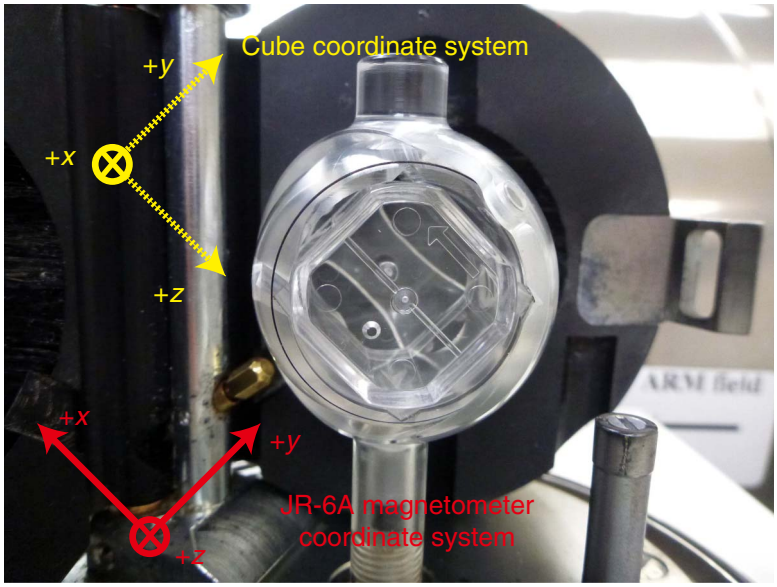

Figure F17. Paleoreconstruction sketches of the Cocos plate at 2 and 12 Ma, with DSDP (red dots) and ODP (green dots) drill sites shown. Magnetic anomalies of the region are shown by fine and short black lines. Reconstruction made using the web-based software at **www.odsn.de/odsn/services/paleomap/paleomap.html.**

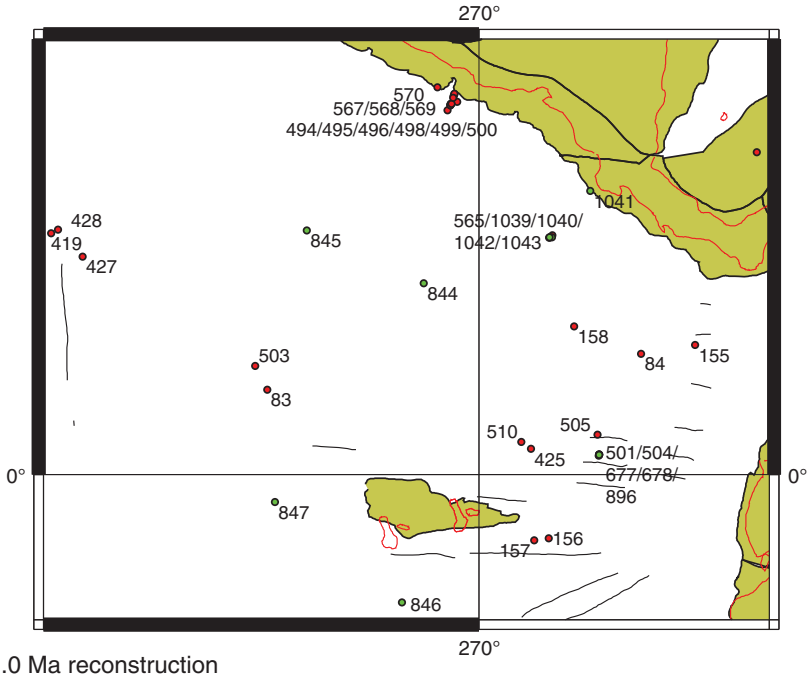

2.0 Ma reconstruction

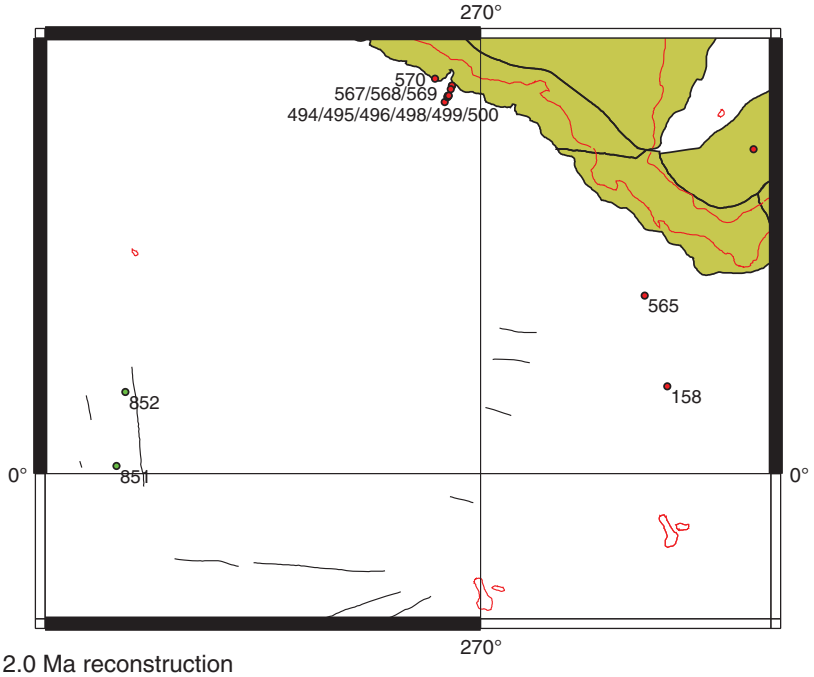

12.0 Ma reconstruction

Figure F18. Wireline tool strings. **A.** Triple combo-UBI. **B.** FMS-sonic. This illustrates the most complete configuration, as used in Hole U1414A. See the site chapters for tools deployed at each site. UBI = Ultrasonic Borehole Imager, LEH-MT = logging equipment head-mud temperature, EDTC = Enhanced Digital Telemetry Cartridge, HNGS = Hostile Environment Natural Gamma Ray Sonde, HLDS = Hostile Environment Litho-Density Sonde, HRLA = High-Resolution Laterolog Array, GPIT = General Purpose Inclinometry Tool, FMS = Formation MicroScanner, DSI = Dipole Shear Sonic Imager.

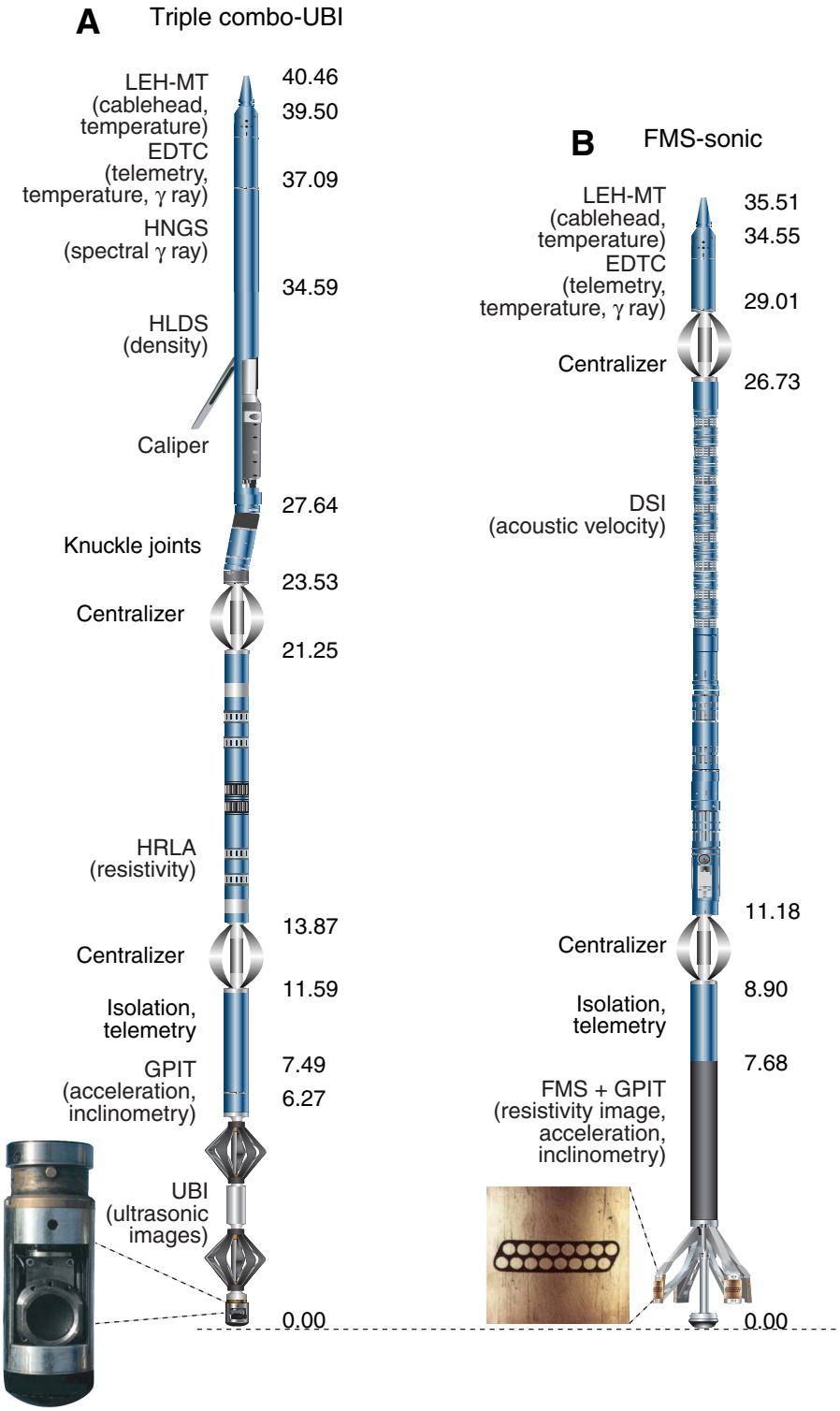

Table T1. Classification of volcanic lithologies, Expedition 344.

	Mixture		
	Tephras	Tuffites	Epiclastic deposits
>64 mm	Pyroclastic breccia	Tuffaceous breccia/ Conglomerate	Breccia/Conglomerate
2–64 mm	Lapillistone/Lapilli tuff	Tuffaceous gravel	Gravel
64 µm–2 mm	Coarse ash tuff	Tuffaceous sandstone	Sandstone
2–64 µm	Fine ash tuff	Tuffaceous siltstone	Siltstone
<2 µm	Volcanic dust	Tuffaceous volcanic dust	Claystone
Amount of pyroclasts	≥75%	<75% to >25%	≤25%

Modified after Fisher and Schmincke (1984).

Table T2. Characteristic X-ray diffraction peaks for semiquantitative area analysis, Expedition 344.

Mineral	Reflection	d-value (Å)	Peak position (°2θ)
Composite clay	Multiple	4.478	19.4–20.4
Quartz	101	3.342	26.3–27.0
Plagioclase	002	3.192	27.4–28.2
Calcite	104	3.035	29.1–29.7

Table T3. Geomagnetic polarity timescale used for magnetostratigraphy during Expedition 344 (to Eocene). (Continued on next two pages.)

Geological age	Base age (Ma)		Polarity chron	Top (Ma)	Base (Ma)	Duration (m.y.)	Remarks
Quaternary							
Holocene	11.5 ka						
Pleistocene		C1	C1n (Brunhes)	0	0.781	0.781	Base of middle Pleistocene (Ionian) = base of Brunhes Chron
late (Tarantian)	0.126		C1r.1r (Matuyama)	0.781	0.988	0.207	
middle (Ionian)	0.781		C1r.1n (Jaramillo)	0.988	1.072	0.084	
			C1r.2r	1.072	1.173	0.101	
			C1r.2n (Cobb Mountain)	1.173	1.185	0.012	Cobb Mountain cryptochron is within early part of Matuyama (C1r) Chron
			C1r.3r	1.185	1.778	0.593	
early (Calabrian)	1.806	C2	C2n (Olduvai)	1.778	1.945	0.167	Base of Calabrian is in lower part of Olduvai Chron
			C2r.1r	1.945	2.128	0.183	
			C2r.1n (Reunion)	2.128	2.148	0.020	
			C2r.2r (Matuyama)	2.128	2.581	0.453	Base of Pleistocene is near base of Matuyama Chron
(Gelasian)	2.588						
Pliocene		C2A	C2An.1n (Gauss)	0.000	3.032	3.032	Gauss Normal Chron (C2An) contains two reversed intervals—Kaena (2An.1r) and Mammoth (2An.2r)
			C2An.1r (Keana)	3.032	3.116	0.084	
			C2An.2n	3.116	3.207	0.091	
			C2An.2r (Mammoth)	3.207	3.330	0.123	
late (Piacenzian)	3.600		C2An.3n (Gauss)	3.330	3.596	0.266	Base of Piacenzian is base of Chron C2An.3n
			C2Ar (Gilbert)	3.596	4.187	0.591	Gilbert Reversed Chron spans Chrons C2Ar through C3r
		C3	C3n.1n (Cochiti)	4.187	4.300	0.113	
			C3n.1r	4.300	4.493	0.193	
			C3n.2n (Nunivak)	4.493	4.631	0.138	
			C3n.2r	4.631	4.799	0.168	
			C3n.3n (Sidufjall)	4.799	4.896	0.097	
			C3n.3r	4.896	4.997	0.101	
early (Zanclean)	5.332		C3n.4n (Thvera)	4.997	5.235	0.238	Base of Miocene is in uppermost Chron C3r
Miocene			C3r (Gilbert)	5.235	6.033	0.798	
		C3A	C3An.1n	6.033	6.252	0.219	
			C3An.1r	6.252	6.436	0.184	
			C3An.2n	6.436	6.733	0.297	
			C3Ar	6.733	7.140	0.407	
		C3B	C3Bn	7.140	7.212	0.072	
late (Messinian)	7.246		C3Br.1r	7.212	7.251	0.039	Base of Messinian is in lowermost Chron C3Br.1r
			C3Br.1n	7.251	7.285	0.034	
			C3Br.2r	7.285	7.454	0.169	
			C3Br.2n	7.454	7.489	0.035	
			C3Br.3r	7.489	7.528	0.039	
		C4	C4n.1n	7.528	7.642	0.114	
			C4n.1r	7.642	7.695	0.053	
			C4n.2n	7.695	8.108	0.413	
			C4r.1r	8.108	8.254	0.146	
			C4r.1n	8.254	8.300	0.046	
			C4r.2r	8.300	8.771	0.471	Cryptochron C4r.2r-1 within C4r.2r (ca. 8.661–8.699 Ma)
		C4A	C4An	8.771	9.105	0.334	
			C4Ar.1r	9.105	9.311	0.206	
			C4Ar.1n	9.311	9.426	0.115	
			C4Ar.2r	9.426	9.647	0.221	
			C4Ar.2n	9.647	9.721	0.074	
			C4Ar.3r	9.721	9.786	0.065	
		C5	C5n.1n	9.786	9.937	0.151	
			C5n.1r	9.937	9.984	0.047	
			C5n.2n	9.984	11.056	1.072	Cryptochrons C5n.2n-1, 2, 3
			C5r.1r	11.056	11.146	0.090	
			C5r.1n	11.146	11.188	0.042	
			C5r.2r	11.188	11.592	0.404	Subchron C5r.2r-1 is within C5r.2r (ca. 11.263–11.308 Ma)
(Tortonian)	11.63		C5r.2n	11.592	11.657	0.065	Base of Tortonian = near base of Chron C5r.2n
			C5r.3r	11.657	12.049	0.392	

Table T3 (continued).

Geological age	Base age (Ma)		Polarity chron	Top (Ma)	Base (Ma)	Duration (m.y.)	Remarks
		C5A	C5An.1n	12.049	12.174	0.125	
			C5An.1r	12.174	12.272	0.098	
			C5An.2n	12.272	12.474	0.202	
			C5Ar.1r	12.474	12.735	0.261	
			C5Ar.1n	12.735	12.770	0.035	
			C5Ar.2r	12.770	12.829	0.059	
			C5Ar.2n	12.829	12.887	0.058	
			C5Ar.3r	12.887	13.032	0.145	
		C5AA	C5AAn	13.032	13.183	0.151	
			C5AAr	13.183	13.363	0.180	
		C5AB	C5ABn	13.363	13.608	0.245	
			C5ABr	13.608	13.739	0.131	
middle (Serravalian)	13.82	C5AC	C5ACn	13.739	14.070	0.331	Base of Serravalian = upper Chron C5ACn
			C5ACr	14.070	14.163	0.093	
		C5AD	C5ADn	14.163	14.609	0.446	
			C5ADr	14.609	14.775	0.166	
		C5B	C5Bn.1n	14.775	14.870	0.095	
			C5Bn.1r	14.870	15.032	0.162	
			C5Bn.2n	15.032	15.160	0.128	
(Langhian)	15.97		C5Br	15.160	15.974	0.814	Base of Langhian = base of Chron C5Br
		C5C	C5Cn.1n	15.974	16.268	0.294	
			C5Cn.1r	16.268	16.303	0.035	
			C5Cn.2n	16.303	16.472	0.169	
			C5Cn.2r	16.472	16.543	0.071	
			C5Cn.3n	16.543	16.721	0.178	
			C5Cr	16.721	17.235	0.514	
		C5D	C5Dn	17.235	17.533	0.298	
			C5Dr.1r	17.533	17.717	0.184	
			C5Dr.1n	17.717	17.740	0.023	Cryptochron in C5Dr
			C5Dr.2r	17.740	18.056	0.316	
		C5E	C5En	18.056	18.524	0.468	
			C5Er	18.524	18.748	0.224	
		C6	C6n	18.748	19.722	0.974	
			C6r	19.722	20.040	0.318	Cryptochron C6r-1
		C6A	C6An.1n	20.040	20.213	0.173	
early (Burdigalian)	20.44		C6An.1r	20.213	20.439	0.226	Base of Burdigalian (working version) = approx. base of Chron C6An.1r (used here) or of Chron C6An.1n
			C6An.2n	20.439	20.709	0.270	
			C6Ar	20.709	21.083	0.374	
		C6AA	C6AAn	21.083	21.159	0.076	
			C6AAr.1r	21.159	21.403	0.244	
			C6AAr.1n	21.403	21.483	0.080	
			C6AAr.2r	21.483	21.659	0.176	
			C6AAr.2n	21.659	21.688	0.029	
			C6AAr.3r	21.688	21.767	0.079	
		C6B	C6Bn.1n	21.767	21.936	0.169	
			C6Bn.1r	21.936	21.992	0.056	
			C6Bn.2n	21.992	22.268	0.276	
			C6Br	22.268	22.564	0.296	
		C6C	C6Cn.1n	22.564	22.754	0.190	
			C6Cn.1r	22.754	22.902	0.148	
(Aquitanian)	23.03		C6Cn.2n	22.902	23.030	0.128	Base of Miocene = base of Chron C6Cn.2n
Paleogene			C6Cn.2r	23.030	23.233	0.203	
Oligocene			C6Cn.3n	23.233	23.295	0.062	
			C6Cr	23.295	23.962	0.667	
		C7	C7n.1n	23.962	24.000	0.038	
			C7n.1r	24.000	24.109	0.109	
			C7n.2n	24.109	24.474	0.365	
			C7r	24.474	24.761	0.287	Cryptochron C7r-1
		C7A	C7An	24.761	24.984	0.223	
			C7Ar	24.984	25.099	0.115	

Table T3 (continued).

Geological age	Base age (Ma)		Polarity chron	Top (Ma)	Base (Ma)	Duration (m.y.)	Remarks
		C8	C8n.1n	25.099	25.264	0.165	
			C8n.1r	25.264	25.304	0.040	
			C8n.2n	25.304	25.987	0.683	Cryptochron C8n.2n-1
			C8r	25.987	26.420	0.433	
		C9	C9n	26.420	27.439	1.019	Cryptochrons C9n-1, 2
			C9r	27.439	27.859	0.420	Cryptochron C9r-1
late (Chattian)	28.09	C10	C10n.1n	27.859	28.087	0.228	Base of Chattian (working version) base of Chron C10n.1n. (Note: base is potentially at ~70% up in undifferentiated Chron C10n in candidate GSSP in Italy [Coccioni et al., 2008], which would project as equivalent to C10n.1n.4.)
			C10n.1r	28.087	28.141	0.054	
			C10n.2n	28.141	28.278	0.137	
			C10r	28.278	29.183	0.905	Cryptochrons C10r-1, 2
		C11	C11n.1n	29.183	29.477	0.294	
			C11n.1r	29.477	29.527	0.050	
			C11n.2n	29.527	29.970	0.443	
			C11r	29.970	30.591	0.621	Cryptochron C11r-1
		C12	C12n	30.591	31.034	0.443	
			C12r	31.034	33.157	2.123	Cryptochrons C12r-1, 2, 3, 4, 5, 6, 7, 8
		C13	C13n	33.157	33.705	0.548	Cryptochron C13n-1
early (Rupelian)	33.89		C13r	33.705	34.999	1.294	Base of Rupellian is at Chron C13r.86 Cryptochrons C13r-1, 2, 3, 4
Eocene		C15	C15n	34.999	35.294	0.295	C14 does not exist
			C15r	35.294	35.706	0.411	
		C16	C16n.1n	35.706	35.892	0.186	
			C16n.1r	35.892	36.051	0.159	
			C16n.2n	36.051	36.700	0.649	
			C16r	36.700	36.969	0.269	
late (Priabonian)	37.75	C17	C17n.1n	36.969	37.753	0.784	Base of Priabonian (working version) assigned as base of Chron C17n.1n
			C17n.1r	37.753	37.872	0.119	
			C17n.2n	37.872	38.093	0.221	
			C17n.2r	38.093	38.159	0.065	
			C17n.3n	38.159	38.333	0.174	
			C17r	38.333	38.615	0.283	
		C18	C18n.1n	38.615	39.627	1.012	Cryptochron C18n.1n-1
			C18n.1r	39.627	39.698	0.070	
			C18n.2n	39.698	40.145	0.447	
middle (Bartonian)	41.15		C18r	40.145	41.154	1.010	Base of Bartonian (working version) assigned as base of Chron C18r
		C19	C19n	41.154	41.390	0.235	
			C19r	41.390	42.301	0.912	
		C20	C20n	42.301	43.432	1.130	
			C20r	43.432	45.724	2.292	
		C21	C21n	45.724	47.349	1.625	
(Lutetian)	47.84		C21r	47.349	48.566	1.217	Base of Lutetian is Chron C21r.6
		C22	C22n	48.566	49.344	0.778	
			C22r	49.344	50.628	1.283	
		C23	C23n.1n	50.628	50.835	0.207	
			C23n.1r	50.835	50.961	0.126	
			C23n.2n	50.961	51.833	0.872	
			C23r	51.833	52.620	0.787	
		C24	C24n.1n	52.620	53.074	0.454	
			C24n.1r	53.074	53.199	0.125	
			C24n.2n	53.199	53.274	0.075	
			C24n.2r	53.274	53.416	0.142	
			C24n.3n	53.416	53.983	0.567	
early (Ypresian)	55.96		C24r	53.983	57.101	3.118	Base of Eocene is 1.14 m.y. after beginning of Chron C24r, or ca. Chron C24r.37 Cryptochrons C24r-1, 2, 3, 4, 5, 6, 7, 8, 9, 10, 11

Datums are from Gradstein et al. (2012). Boundary ages of Chrons C1n–C13n and C24n.1n–C34n are orbitally tuned, whereas those for Chrons C13r–C23r are spline fitted (Gradstein et al., 2012). Cryptochrons are from Cande and Kent (1995) and noted in the Remarks column.

Table T4. Downhole measurements made by wireline tool strings, Expedition 344.

Tool string	Tool	Measurement	Sampling interval (cm)	Approximate vertical resolution (cm)
Triple combo-Ultrasonic Borehole Imager (UBI)	EDTC	Total gamma ray	5 and 15	30
	HNGS	Spectral gamma ray	15	20–30
	HLDS	Bulk density	2.5 and 15	38
	HRLA	Resistivity	15	30
	DIT	Resistivity	15	200/150/76
	GPIT	Tool orientation	0.25 and 15	NA
	UBI	Ultrasonic images	0.5–2.5	0.5–2.5
Formation MicroScanner (FMS)-sonic combination	EDTC	Total gamma ray	5 and 15	30
	DSI	Acoustic velocity	15	107
	GPIT	Tool orientation	0.25 and 15	NA
	FMS	Resistivity images	0.25	0.5

NA = not applicable. See Table T5 for definitions of tool acronyms.

Table T5. Acronyms and units used for downhole wireline tools and measurements, Expedition 344.

Tool	Output	Explanation	Unit
DIT		Dual Induction Tool	
	IDPH	Deep induction resistivity	Ωm
	IMPH	Medium induction resistivity	Ωm
	SFLU	Spherically focused resistivity	Ωm
DSI		Dipole Shear Sonic Imager	
	DTCO	Compressional wave slowness	µs/ft
	DTSM	Shear wave slowness	µs/ft
	DT1	Shear wave slowness, lower dipole	µs/ft
	DT2	Shear wave slowness, upper dipole	µs/ft
EDTC		Enhanced Digital Telemetry Cartridge	
	GR	Total gamma ray	gAPI
	ECGR	Environmentally corrected gamma ray	gAPI
	EHGR	High-resolution environmentally corrected gamma ray	gAPI
	MTEM	Borehole fluid temperature	°C
FMS		Formation MicroScanner	
	C1, C2	Orthogonal hole diameters	Inch
	P1AZ	Pad 1 azimuth	Degrees
		Spatially oriented resistivity images of borehole wall	
GPIT		General Purpose Inclinometry Tool	
	DEVI	Hole deviation	Degrees
	HAZI	Hole azimuth	Degrees
	F*x*, F*y*, F*z*	Earth's magnetic field (three orthogonal components)	Degrees
	A*x*, A*y*, A*z*	Acceleration (three orthogonal components)	m/s^2
HLDS		Hostile Environment Litho-density Sonde	
	RHOM	Bulk density	g/cm^3
	PEFL	Photoelectric effect	$barn/e^-$
	LCAL	Caliper (measure of borehole diameter)	Inch
	DRH	Bulk density correction	g/cm^3
HNGS		Hostile Environment Gamma Ray Sonde	
	HSGR	Standard (total) gamma ray	gAPI
	HCGR	Computed gamma ray (HSGR minus uranium contribution)	gAPI
	HFK	Potassium	wt%
	HTHO	Thorium	ppm
	HURA	Uranium	ppm
HRLA		High-Resolution Laterolog Array Tool	
	RLAX	Apparent resistivity from computed focusing mode X (X = 1 to 5)	Ωm
	RT_HLRT	True formation resistivity	Ωm
	RM_HLRT	Borehole fluid resistivity	Ωm

LEH, HNGS, HLDS, GPIT, and UBI are trademarks of Schlumberger. For the complete list of acronyms used in IODP and for additional information about tool physics, consult IODP-USIO Science Services, LDEO, at iodp.ldeo.columbia.edu/TOOLS_LABS/tools.html.